Temperature and Metallicity Profiles of Galaxy Clusters — Background Study for X-ray CCD Camera onboard the Suzaku Satellite —

Noriaki Tawa

Department of Earth and Space Science, Graduate School of Science,
Osaka University, Japan

March 6, 2008

Abstract

We present an analysis of Suzaku spatially resolved spectroscopy data for nearby galaxy clusters. Galaxy clusters are the largest gravitationally bounded objects in the universe and contain galaxies, X-ray emitted hot gas (intracluster medium: ICM), and a large amount of dark matter. Studies of galaxy clusters are important for understanding cosmological structure formation and evolution.

The X-ray Imaging Spectrometer (XIS) system onboard Suzaku is best suited for measurements of the outermost regions of clusters due to its large effective area and low and stable non-X-ray background (NXB). In order to make the best use of the low and stable NXB, we construct an NXB database with an exposure of approximately 785 ks for each XIS. We also establish a method to model the NXB spectrum using the cut-off-rigidity or the count rate of the PIN upper discriminator (PIN-UD) in hard X-ray detector onboard Suzaku. The reproducibility of the NXB model using PIN-UD is better than that of the model using the cut-off-rigidity. The reproducibility of the NXB model using PIN-UD is 4.55–5.63% for each XIS NXB in the 1–7 keV band and 2.79–4.36% for each XIS NXB in the 5–12 keV band.

The estimation of the cosmic X-ray background (CXB) is also important for the analysis of faint diffuse sources such as galaxy clusters. Therefore, we analyze six blank sky observations with Suzaku and evaluate the CXB spectrum and its spatial fluctuation. The CXB spectrum can be well reproduced by an absorbed single power-law model whose average photon index is 1.451 ± 0.034 (1σ confidence level, CL). On the other hand, the average 2–10 keV flux of the CXB is $(4.37 \pm 0.14) \times 10^{-15}$ erg cm^{-2} s^{-1} arcmin^{-2} (1σ CL), and its spatial fluctuation in the XIS field of view by one third, ~ 78.66 arcmin^2, is $12.0 \pm 2.4\%$ (1σ CL).

Using the NXB model for background subtraction and considering the CXB fluctuation for the error estimation, we determine the temperature and surface brightness profiles of eight regular clusters, which include A1060, A1413, A1795, A2052, A2218, A2801, A2804, and A2811. While there are large scatters at the center, these both profiles exhibit similarity from a radius of $0.15r_{180}$ to r_{180}, where r_{180} denotes the virial radius. The temperatures significantly decline with the radius in the outer region ($r \gtrsim 0.15r_{180}$), and their general trend is fitted with a model with a polytropic index of 1.190 ± 0.034 (90% CL). Our temperature profiles are in good agreement with previous measurements from ASCA (Markevitch et al.), BeppoSAX (De Grandi & Molendi), Chandra (Vikhlinin et al.), and XMM-Newton (Pratt et al.) at $0.2r_{180}$ to $0.6r_{180}$, but show the boundary to be extended up to r_{180}. Moreover, our temperature profiles show good agreement with recent numerical simulations of the cold dark matter model from $0.15r_{180}$ to r_{180}.

We measure the metallicities of our sample of the eight regular clusters, A1674, and the link region between A399 and A401. While there is a large scatter in the metallicity profiles at the center, the metallicities in the outer region ($0.4r_{180} \lesssim r \lesssim 0.7$–$0.8r_{180}$) approximately constant at $0.2Z_{\odot}$. We extend the measurement of metallicity by a factor of approximately two. The constant and high metallicities in the outer region suggest that metals were transported into the ICM by galactic outflows before the clusters formed ($z \sim 2$) and that the proto-cluster region was heavily polluted with the metals.

Finally, we search for the O VII line emitted from the warm-hot intergalactic medium (WHIM) surrounding A1413 and in the Sculptor supercluster to which A2801, A2804, and A2811 belong. These galaxy clusters have relatively high redshifts, which is important to distinguish the redshifted O VII line of the WHIM from the unredshifted one of the soft X-ray background. We detect no significant line and set a tight constraint on the intensity with upper limits for the surface brightness of O VII line of 1.6×10^{-7} photons cm^{-2} s^{-1} arcmin^{-2} for A1413 and 5.2×10^{-8} photons cm^{-2} s^{-1} arcmin^{-2} for the Sculptor supercluster.

Contents

List of Tables

List of Figures

Chapter 1

Introduction

Galaxy clusters are the largest gravitationally bounded objects in the universe. They contain the 10–1000 galaxies and the large amount of hot gas, X-ray emitting intracluster medium (ICM), spread over a region of whose size is epically 2 Mpc in radius. However, since the total mass of the galaxies and the ICM is not enough to gravitationally bind themselves, it is predicted that a further huge amounts of matter which is not seen, the so-called "Cold Dark Matter (CDM)," exists. Although the origin of CDM is still an open question, the CDM model has become a standard paradigm for explaining observations on the large scale structure of the universe, i.e., galaxy cluster and supercluster. In the CDM model, the structure of the universe grows hierarchically by gravitational attraction, with small objects merging in a continuous hierarchy to form more and more massive objects. This structure formation suggests that the mass components, which are the ICM mass and the total gravitational mass of a cluster (including the CDM), are representative of the universe as a whole. Although these components can be estimated from X-ray data of the ICM, to accurately estimate these mass components, the X-ray data up to the outermost region of a cluster are required. On the other hand, the metallicity of the ICM and its distribution are the key observable characteristics to constrain the integral past star formation history in clusters and to study the mechanisms that transfer metals from cluster galaxies into the ICM. Thus, X-ray observations up to the outermost regions of clusters are very important for the cosmological probes.

The density, temperature, and metallicity of the ICM at large cluster radius are technically difficult to measure because the X-ray surface brightness of cluster decreases rapidly as distance from the center increases. In addition, previous and current instruments, e.g., Chandra and XMM-Newton, are not suitable to observe the faint and diffuse sources such as the outermost regions of clusters due to their small effective areas or high and unstable background levels. Therefore, their measurements of the ICM have been limited to the

inner regions.

Suzaku, the fifth in the series of Japanese X-ray astronomy satellites devoted to observations of celestial X-ray sources, was launched by Japan Aerospace Exploration Agency (JAXA) on July 10, 2005. One of the main instruments on Suzaku is the X-ray Imaging Spectrometer (XIS), comprised of four X-ray charge-coupled devices (CCDs). Three sensors of the XIS, XIS0, XIS2, and XIS3, have front-illuminated (FI) CCDs (hereafter referred to as XIS-FIs), while the other, XIS1, has a back-illuminated (BI) CCD (Koyama et al. 2007a). The background levels normalized by the effective area and the field of view (FOV), in terms of the S/N ratio to diffuse emissions, of the XIS-FIs are comparable to those of the ASCA SIS and are $\sim$3 and $\sim$10 times lower than those of the XMM-Newton EPIC and the Chandra ACIS at 5 keV, respectively, as shown in Fig. 3.3. The Suzaku XIS should be best suitable for the measurements of faint and extended sources such as the outermost regions of clusters.

The background of the XIS consists of three components: (1) non-X-ray background (NXB); (2) a solar component, which is emission from the earth's atmosphere illuminated by the Sun and solar wind charge exchange; and (3) a sky X-ray background from such sources a local hot bubble (LHB), Milky Way halo (MWH), and cosmic X-ray background (CXB). It is most important to establish a method to accurately evaluate the NXB spectra and its time variations in order to maximize the advantage of the low background level of the XIS. Thus, we construct an XIS NXB database to be used in the evaluation of the NXB and introduce a method to generate the NXB model given the intensity of charged particles in chapter 4. We also examine and confirm the reproducibility of our NXB model.

Among the three components of the XIS background, the solar component varies with time, and hence, is the most difficult to estimate. We try to minimize it by using the orbital and altitude data, which are elevation angles from the day or night Earth edge, and the solar wind data. The sky X-ray background is basically stable but slightly fluctuates from field to field. In the analysis of the faint and spatially diffuse sources, the spectrum of the sky X-ray background has to be evaluated by the observations of other fields by Suzaku. It is important that the spectrum and the spatial fluctuation of the sky X-ray background are accurately measured. We investigate the sky X-ray background using six blank sky observations of Suzaku in chapter 5.

The temperature and density are important measurable characteristics to study the physical properties of the diffuse cosmic baryons in the ICM. Under the action of gravity, these baryons follows the dark matter during the process of hierarchical structure formation, in which they are heated by adiabatic compression during the halo mass growth and

by shocks induced by supersonic accretion or merger events. Under the assumptions that provided gravity dominates the process of gas heating, and gas is in hydrostatic equilibrium within the dark matter, scaling relations for cluster properties, e.g., temperature and density, are predicted because gravity is a scale-free force. These scaling relations has been also predicted by hydrodynamical simulations of galaxy clusters in the CDM model (e.g. Navarro et al. 1995; Evrard et al. 1996; Loken et al. 2002; Borgani et al. 2004). In addition, if the density and temperature profiles of the ICM have the scaling relations, the global temperature of ICM, excluding the core region, should be a good proxy for the total gravitating mass. Therefore, although the temperature profiles were measured by the previous observations, e.g., ASCA (Markevitch et al. 1998), BeppoSAX (De Grandi & Molendi 2002), Chandra (Vikhlinin et al. 2005), and XMM-Newton (Pratt et al. 2007), their profiles were unfortunately limited up to $\sim 0.6 r_{180}$, where r_{180} denotes the virial radius, because of the low effective areas or high and unstable background levels. Therefore, we measure the temperature and surface brightness, which is proportional to the squared gas density, profiles of eight regular clusters up to the virial radii by using the Suzaku observations in chapter 6. Then, we investigate the scaling relations for cluster properties, the heating mechanisms of the ICM, and the relation between the total cluster mass and the ICM temperature.

The metals in the ICM were originally produced by stars in galaxies. However, it is still unclear about possible mechanisms that transfer metals from the cluster galaxies into the ICM. These mechanisms can be classified broadly into two types, ram-pressure stripping by the ICM and energetic outflows from cluster galaxies. In the former mechanism, the metal-enriched gas in the galaxy (interstellar medium) is stripped by the ram pressure exerted by the ICM (Gunn & Gott 1972; Fujita & Nagashima 1999; Quilis et al. 2000). Since the gas density is higher at the cluster center than at the outside, ram-pressure stripping should be most effective at the center. In the latter mechanism, galactic outflows that result from supernova explosions following active star formation in a galaxy inject metals into the ICM (De Young 1978). Since the static pressure exerted by the ICM suppresses the evolution of the galactic outflows, the latter mechanism should be rather effective in the peripheral region of a cluster or the intergalactic space before the cluster forms (a proto-cluster region) (Kapferer et al. 2006). In order to know how and when the metals were transported into the ICM from the galaxies, it is important to determine the metallicity of the ICM in the outermost region of clusters. However, previous observations of metallicity have been limited to the inner region of clusters ($r \lesssim 0.4$–$0.5 r_{180}$) (De Grandi et al. 2004; Pratt et al. 2007). We measure the metallicities of a sample of the eight regular clusters, A1674, and the link region between A399 and A401 in chapter 7.

The numerical simulations of the CDM model (Cen & Ostriker 1999; Davé et al. 2001) have predicted the existence of a large amounts of baryonic matter in the local universe dispersed in the intergalactic medium. This material is expected to reside in the form of tenuous shock-heated warm-hot ($T = 10^{5-7}$ K) filaments of gas in moderate overdensities (about 10–100 times of the mean hydrogen density) tracing the dark matter cosmic web (Dolag et al. 2006), the so-called warm-hot intergalactic medium (WHIM). The firm detection of the WHIM is important because this existence is the most promising candidate for the "missing baryons problem". We search for the O VII line emitted from the WHIM around A1413 and the clusters belonging to the Sculptor supercluster, A2801, A2804, and A2811, in chapter 8.

Chapter 2

Overview of Galaxy Clusters

2.1 Galaxy Clusters

The largest aggregations of matter that can be detected as visible entites are galaxies. The large-scale structure of the universe, as we know it, has been determined by measuring the distribution and motion of galaxies in space. The distribution of galaxies is not random. Although on the largest scale, the arrangement of matter in the universe is uniform, on an intermediate level, galaxies are found in gravitationally bound aggregate referred to as "groups" and "clusters".

Galaxy clusters contain about ten to thousands of galaxies within a radius of several Mpc, so they are usually observed as regions which show an enhancement of the surface galaxy number density over the empty field. Galaxy clusters are the largest gravitationally bound systems in the universe, therefore they set clear constraints on the formation of the structure and composition of the universe. Optically, galaxy clusters are classified according to the number of member galaxies. Clusters containing many galaxies, up to a few thousands, are called rich, while those with fewer members, ten or so, are called poor. The most extensive and often cited catalogs of rich clusters are those of Abell (1958) and Zwicky et al. (1961-1968). They used the Palomar Observatory Sky Survey (POSS) plates for the northern sky and searched for the galaxy enhancements by eye, using somewhat different criteria to identify the cluster. later, Abell's catalogue was extended to the southern sky by his co-workers (Abell et al. 1989). These large catalogs enabled us to make a statistical study of galaxy clusters and large scale structures in the universe.

Many clusters contain a particularly large, bright elliptical galaxy at the center. Since the heliocentric velocity of such a giant elliptical galaxy usually agrees with that of the cluster mean redshift, it should sit at the bottom of the cluster potential well. Such a galaxy is identified as a cD or D galaxy. The cD galaxies are also embedded in an extended

stellar halo of low surface brightness. About 20% of all rich clusters have the cD galaxies (Sarazin 1988).

The gravitational potential which binds galaxies within a cluster also binds a vast cloud of hot gas which fills the space between and around the galaxies. This hot gas is often called the ICM. The ICM has a temperature of $\sim 10^8$ K and is a strong source of X-ray emission. The mass of X-ray emitting gas is about seven times greater than the "optical" mass derived from the total visible luminosity of the galaxies. This indicates that the X-ray data have the large amount of observable matter in galaxy clusters.

In addition, the cluster gravitational potential which is required to explain both X-ray and optical measurements indicates the existence of a large amount of hidden mass. Some data require about six times more mass than that observed in the form of cluster galaxies plus the ICM. This clearly indicates the necessity of non-luminous matter, namely dark matter. However, the nature of dark matter has long been one of the fundamental unsolved problem in astrophysics.

2.2 X-ray observation of galaxy clusters

2.2.1 X-ray emission from a galaxy cluster

It was one of the most surprising discoveries in the history of X-ray astronomy that clusters of galaxies are powerful X-ray emitters. In the 1960's, X-ray emissions from clusters of galaxies were detected from the Virgo cluster, the Coma cluster (Byram 1966), and the Perseus cluster (Fritz et al. 1971) using a sounding rocket. The launch of the first X-ray astronomy satellite Uhuru established that most clusters are generally bright X-ray sources with an X-ray luminosity of 10^{44}–10^{45} erg sec^{-1}. The X-ray emissions from clusters are extended, so that there are two alternative explanations; thermal bremsstrahlung from hot plasma, or inverse Compton of cosmic micro-wave background by high-energy electrons. In 1976, He-like Fe-K line emissions were detected from the Perseus cluster (Mitchell et al. 1976), which revealed that X-ray emissions are emitted from hot gas (ICM) with a temperature of 10^{7-8} K.

2.2.2 X-ray spectrum from the ICM

Since the ICM is low density ($\sim 10^{-3}$ cm^{-3}) and high temperature ($\sim 10^8$ K) plasma, the main radiation mechanism of the continuum emission is thermal bremsstrahlung (free-free radiation) and various atomic emission lines. The emissivity, which is the energy emitted

from the unit volume during the unit time per unit frequency, is given by

$$\epsilon_\nu^{ff} = 6.8 \times 10^{-38} \sum_i Z_i^2 n_e n_i T_g^{-1/2} e^{-h\nu/kT_g} \overline{g_{ff}} \ \ (\mathrm{erg\ s^{-1}\ cm^{-3}\ Hz^{-1}}) \ , \tag{2.1}$$

where Z_i and n_i are the charge and number density of the iron i, n_e is the electron number density in cgs units, and $\overline{g_{ff}}$ is the Gaunt factor which is weakly dependent on the temperature and frequency (Rybicki & Lightman 1979). The bolometric emissivity is then

$$\begin{aligned} \epsilon^{ff} &= \int_0^\infty \epsilon_\nu^{ff} d\nu \\ &\sim 1.4 \times 10^{-27} n_e n_i T_g^{1/2} \sum_i Z_i^2 \overline{g_B} \ \ (\mathrm{erg\ s^{-1}\ cm^{-3}}) \ , \end{aligned} \tag{2.2}$$

where the averaged Gaunt factor $\overline{g_B}$ is 1.1–1.5. The X-ray luminosity in a given bandpass, $\nu_1 \leq \nu \leq \nu_2$, is obtained by integrating Equation (2.1) over the frequency and the cluster volume;

$$L_X = \int dV \int_{\nu_1}^{\nu_2} \epsilon_\nu^{ff} \ d\nu \ . \tag{2.3}$$

Emission of atomic lines becomes significant when the ICM temperature falls below a few keV. Since the temperature of the ICM is of the same order as the K-shell ionization potentials of heavy elements such as O, Ne, Mg, Si, S, and Fe, these elements become mainly He/H-like ions and are completely ionized. These ions are collisionally excited, and then emit their resonance K-lines. In lower temperature clusters, in which Fe ions are not only He-like or H-like but also of a low ionization status, the spectrum exhibits resonance L-lines at ∼1 keV. The emission line spectra from the ionization equilibrium plasma have been calculated by various authors, e.g. Raymond & Smith (1977), Kaastra & Mewe (1993), and so on. In this thesis, we use the APEC code as thin thermal plasma model (Smith et al. 2001) in the XSPEC data analysis package.

2.3 Mass and temperature distributions in a galaxy cluster

We summarize mass distribution in a galaxy cluster and temperature distribution of the ICM by mainly referring to Sarazin (1988).

2.3.1 Hydrostatic equilibrium

Sound crossing time, t_{cross}, in the ICM is given by

$$t_{cross} \sim 6.6 \times 10^8 yr \left(\frac{T_g}{10^8\,\mathrm{K}} \right) \left(\frac{D}{\mathrm{Mpc}} \right) \ , \tag{2.4}$$

where D is the cluster diameter. Since this sound crossing time is considerably shorter than the age of the Universe, we can assume the ICM is hydrostatic equilibrium. The force balance between the gas pressure, P_g, and gravitational force, both acting on the ICM, is expressed as

$$\nabla P_g = -\rho_g \nabla \phi \ , \tag{2.5}$$

where ϕ is the gravitational potential and ρ_g is the gas density which can be written as $\rho_g = \mu n_g m_p$. Here, n_g is the number density including electron and ions, μ (~ 0.6) is the mean molecular weight, and m_p is the proton mass. If we assume spherically symmetry, the above equation is reduced

$$\frac{dP_g}{dr} = -\mu n_g m_p \frac{d\phi}{dr} \ , \tag{2.6}$$

where r is the three dimensional radius. Because of the low density ($n_g < 10^{-2}\,\mathrm{cm}^{-3}$), the ICM can be treated as an ideal gas that follows the equation of state as

$$P_g = n_g k T_g \ . \tag{2.7}$$

By combining Newton's equation,

$$\frac{\phi(r)}{dr} = \frac{GM(<r)}{r^2} \ , \tag{2.8}$$

where G is the gravitational constant, and eq. (2.6), the total gravitating mass within a radius r, $M(<r)$, is expressed as follows,

$$M(<r) = -\frac{1}{\mu n_g(r) m_p} \frac{r^2}{G} \frac{dP_g(r)}{dr} \tag{2.9}$$

$$= -\frac{kT_g(r) r}{\mu m_p G} \left(\frac{d \ln T_g(r)}{d \ln r} + \frac{d \ln n_g(r)}{d \ln r} \right) . \tag{2.10}$$

We thus can obtain the mass profile $M(<r)$ from the measurements of the density distribution $n_g(r)$ and the temperature distribution $T_g(r)$. Furthermore, knowledge of $n_g(r)$ readily allows us to estimate the ICM mass profile $M_g(<r)$, which is written as

$$M_g(<r) = \int_0^r 4\pi r'^2 \mu m_p n_g(r') \ dr' \ . \tag{2.11}$$

Therefore, we can estimate the baryonic fraction as a function of r by incorporating optical data on the galaxy distribution.

2.3.2 King profile

We consider a cluster of galaxies to be a self-gravitational system consisting of collisionless particles of a single species, although a cluster is in fact a multi-component system consisting of at least galaxies, ICM, and dark matter. We assume the particles to have a mass m, a density profile $n(r)$, and an isotropic-uniform velocity dispersion of σ_r.

The hydrostatic equation for the particles can be written as,

$$\frac{d\phi(r)}{dr} = -\sigma_r^2 \frac{d\ln n(r)}{dr} \ , \tag{2.12}$$

which may be integrated and solved for $n(r)$ as,

$$n(r) = n_0 \exp\left[-\frac{\phi(r)}{\sigma_r^2}\right] \ , \tag{2.13}$$

where n_0 is the central density. We may combine this with the Poisson equation,

$$\nabla^2\phi(r) = 4\pi G m n(r) \ , \tag{2.14}$$

to determine $n(r)$ and $\phi(r)$.

Although Eqs. (2.13) and (2.14) do not give a trivial solution, King (1962) derived an approximate solution for $n(r)$ and $\phi(r)$ as,

$$n(r) = n_0(1+x^2)^{-3/2} \ , \tag{2.15}$$

and

$$\phi(r) = -4\pi G n_0 m r_c^2 \frac{\ln(x+(1+x^2)^{1/2})}{x} \ , \tag{2.16}$$

where r_c is a characteristic radius called the core radius, and x is r/r_c. These two expression satisfy the Poisson equation (2.14) exactly, while they only approximately satisfy the hydrostatic equilibrium equation (2.12). The mass enclosed within a radius r in the King profile is expressed as follows,

$$M_{\rm King}(<r) = \int_0^r 4\pi r'^2 m n(r')\ dr' \tag{2.17}$$

$$= 4\pi m n_0 r_c^3 \left(\ln\left[x+\sqrt{1+x^2}\right] - \frac{x}{\sqrt{1+x^2}}\right) \ . \tag{2.18}$$

2.3.3 Isothermal β model

Next, we consider the ICM density profile in the King potential. For simplicity we may approximate the ICM to be isothermal (T_g = constant). Then, eq. (2.10) can be simplified as follows,

$$M(<r) = -\frac{kT_g r}{\mu m_p G}\left(\frac{d\ln n_g}{d\ln r}\right) \ . \tag{2.19}$$

Using Newton equation, $M(r)$ is also expressed as,

$$M(r) = \frac{r^2}{G}\frac{d\phi(r)}{dr} \ . \tag{2.20}$$

We may combine Eqs. (2.19) and (2.20) as,

$$\frac{d\ln n_g(r)}{dr} = \beta\frac{d\ln n(r)}{dr} \ , \tag{2.21}$$

with

$$\beta \equiv \frac{\mu m_p \sigma_r^2}{kT_g} \ . \tag{2.22}$$

β can be approximately calculated as follows,

$$\beta = 0.726\left(\frac{\sigma_r}{10^3\ \mathrm{km\,s^{-1}}}\right)^2\left(\frac{T_g}{10^8\ \mathrm{K}}\right)^{-1} \ . \tag{2.23}$$

Integrating eq. (2.21), we get

$$n_g(r) = n_{g0}\exp(-\beta[\phi(r) - \phi(0)]) \ , \tag{2.24}$$

where n_{g0} is the central density of the ICM. Applying eq. (2.16) to the above equation, $n_g(r)$ can be expressed as follows,

$$n_g(r) = n_{g0}(1 + x^2)^{-3\beta/2} \ . \tag{2.25}$$

This equation is called the β model.

The X-ray emitting gas floats in, but does not contribute appreciably to, this potential. The X-ray emission is proportional to the square of the gas observed surface brightness, S, can be described by the form

$$S = S_0(1 + x^2)^{-3\beta+1/2} \ , \tag{2.26}$$

where S_0 is the central surface brightness. This indicates that, as radius increases, the surface brightness and the density of gas decrease rapidly. At the core radius, where $x = 1$, the X-ray surface brightness generally drops to 10–30% of its value at the center.

When the ICM density is given by the β model, from eq. (2.10) we readily get

$$M(<r) = \frac{3kT_g\beta r}{\mu m_p G}\frac{x^2}{1 + x^2} \tag{2.27}$$

2.3.4 Virial radius

The virial radius, r_{δ_c}, is a distance from the cluster center within which the mean density is δ_c times the current critical density of universe, ρ_c, as

$$\rho_c = \frac{3H(z)^2}{8\pi G} \ , \tag{2.28}$$

where $H(z)$ is the Hubble parameter at the redshift of z. Under assuming a spherically symmetric gas density distribution of the β-model (subsection 2.3.3) form, the total gravitating mass within the virial radius, M_{δ_c}, is expressed as

$$M_{\delta_c} = \delta_c \, \rho_c \cdot \frac{4\pi}{3} \, r_{\delta_c}^3 = \frac{3k \, T_g \, \beta \, r_{\delta_c}}{\mu \, m_p \, G} \frac{x_{\delta_c}^2}{1 + x_{\delta_c}^2} \ , \tag{2.29}$$

where x_{δ_c} is r_{δ_c}/r_c. M_{δ_c} is often called as virial mass.

As discussed in Navarro et al. (1995, 1996), clusters of different scale are expected to show similar structures when scaled to such a virial radius. For the calculation of r_{180}, we used the r_δ–T relation obtained from the numerical simulation by Evrard et al. (1996),

$$r_{180} = 1.95 h^{-1} (T_X / 10 \text{ keV})^{1/2} (1+z)^{-3/2} \text{ Mpc} \ , \tag{2.30}$$

where T_X is emission-weighted temperature of the ICM. Thus, the virial radius and the virial mass have simply relations with T_X as follows,

$$r_{\delta_c} \propto (1+z)^{-3/2} \, T_X^{1/2} \ , \tag{2.31}$$

$$M_{\delta_c} \propto (1+z)^{-3/2} \, T_X^{3/2} \ . \tag{2.32}$$

Arnaud et al. (2005) also reported the r_δ–T relation which is slightly different from that of Evrard et al. (1996).

2.3.5 Adiabatic and polytropic distributions

We described the ICM in the case of isothermal conditions. However, recently, it has been becoming clear that the temperature of cluster is not exactly isothermal. Therefore, we describe the adiabatic and polytropic distribution in this subsection.

If thermal condition is slow, but the ICM is well-mixed, then the entropy per atom in the gas will be constant. In an adiabatic gas, the pressure and density are simply related,

$$P \propto \rho^\gamma \ , \tag{2.33}$$

where γ is the usual ratio of specific heats and is $\gamma = 5/3$ for a monatomic ideal gas. While the value of 5/3 would be expected to apply if the ICM was strictly adiabatic, eq.

(2.33) is often used to parametrize the thermal distribution of the ICM, with γ taken to be a fitting parameter. For example, $\gamma = 1$ implies that the gas distribution is isothermal. Intracluster gas models with an arbitrary value of γ are often referred to as "polytropic" models, and γ is called the polytropic index.

If the ICM was hydrostatic but had a steep temperature gradient

$$-\frac{d\ln T_g}{dr} > -\frac{2}{3}\frac{d\ln n_g}{dr} \ , \tag{2.34}$$

it would be unstable to convective mixing. If the temperature gradient in eq. (2.34) were exeeded by a significant amount, mixing would occur within several sound crossing times in the cluster. Since this is a rather sort time, it is reasonable to assume that the temperature gradient is smaller than that in eq. (2.34).

On the other hand, combining the equation of state (eq. 2.7), eq. (2.33) can be converted as,

$$\frac{n_g}{n_{g0}} = \left(\frac{T_g}{T_{g0}}\right)^{1/(\gamma-1)} \ , \tag{2.35}$$

where n_{g0} and T_{g0} are the central values of the ICM temperature and the density, respectively. Then, this equation is differentiated with respect to the radius as follows,

$$\frac{d\ln T_g}{dr} = (\gamma-1)\frac{d\ln n_g}{dr} \ . \tag{2.36}$$

From this equation, eq. (2.34) implies that hydrostatic polytropic models must have $1 \leq \gamma \leq 5/3$.

Here, we describe the distribution of the adiabatic and polytropic ICM. Given eq. (2.33), the hydrostatic equation (2.5) can be rewritten by noting that

$$\frac{1}{\rho_g}\nabla P = \frac{\gamma}{\gamma-1}\frac{k}{\mu m_p}\nabla T_g \ , \tag{2.37}$$

so that

$$\frac{T_g}{T_{g0}} = 1 + (\alpha-1)\left[1 - \frac{\phi(r)}{\phi_0}\right] \ , \tag{2.38}$$

where ϕ_0 is the central values of the cluster gravitational potential. The integration constant α is defined as

$$\alpha \equiv \frac{T_{g0}}{T_{g\infty}} \ , \tag{2.39}$$

where $T_{g\infty}$ is the gas temperature at infinity. If $\alpha > 1$, from eq. (2.38), the ICM temperature always decrease with increasing distance from the cluster center in adiabatic or polytropic models.

Markevitch et al. (1999) obtained the polytropic gas-temperature profile under assuming a spherically symmetric gas density distribution of the β-model (eq. 2.25) form and assuming the polytropic temperature profile

$$T(r) \propto \rho_g^{\gamma-1}(r) \ . \tag{2.40}$$

The temperature profile, $T(x)$, that is emission-weighted (by ρ_g^2) along the line of sight l, as a function of the projected distance from the center x (such that $r^2 = x^2 + l^2$), is calculated as

$$\begin{aligned} T(x) &= \frac{\int_0^\infty T(r)\rho_g^2(r)\,dl}{\int_0^\infty \rho_g^2(r)\,dl} \propto \frac{\int_0^\infty \rho_g^{1+\gamma}(r)\,dl}{\int_0^\infty \rho_g^2(r)\,dl} \propto \frac{\int_0^\infty (1+x^2+l^2)^{-(3/2)\beta(1+\gamma)}\,dl}{\int_0^\infty (1+x^2+l^2)^{-3\beta}\,dl} \\ &\propto \frac{(1+x^2)^{-(3/2)\beta(1+\gamma)+1/2}}{(1+x^2)^{-3\beta+1/2}} = (1+x^2)^{-(3/2)\beta(\gamma-1)} \ . \end{aligned} \tag{2.41}$$

That is, the resulting projected temperature profile has the sample shape as the real (three-dimensional) profile in eq. (2.40).

Chapter 3

Suzaku

Astro-E2, the fifth in the series of Japanese X-ray astronomy satellites devoted to observations of celestial X-ray sources, was launched by JAXA on July 10, 2005 as the recovery mission of Astro-E, and was renamed Suzaku. Suzaku is developed by the Institute of Space and Astronautical Science of JAXA (ISAS/JAXA) in collaboration with the National Aeronautics and Space Administration's Goddard Space Flight Center (NASA/GSFC) and many other institutions, including Osaka Univ. It is in a near circular orbit at 570 km altitude with an inclination angle of 31° and the orbital period of about 96 minutes. Its total mass at launch was 1706 kg, and the spacecraft length is 6.5 m along the telescope axis after deployment of the extensible optical bench (EOB). Schematic views are shown in Fig. 3.1.

Suzaku is equipped with three scientific instruments: the XIS (Koyama et al. 2007a), the Hard X-ray Detector (HXD, Takahashi et al. 2007), and the X-ray Spectrometer (XRS, Kelley et al. 2007). The XIS is comprised of four X-ray CCDs, capable of moderate energy resolution. Each XIS is located in the focal plane of a dedicated X-ray Telescope (XRT, Serlemitsos et al. 2007). The capabilities of the XIS and the XRT are summarized in table 3.1. The HXD is a non-imaging, collimated detector, which extends the bandpass of the observatory to much higher energies with its 10–600 keV bandpass (Kokubun et al. 2007). The XRS is no longer operational and will not be discussed further. Nevertheless, Suzaku still has the wide-energy range of 0.2–600 keV, moderate energy resolution at low energy band, and a low and extremely stable background level compared with other major X-ray satellites.

Table 3.1: Overview of Suzaku capabililties.

S/C	Orbit apogee	568 km
	Orbital period	96 min
	Observing efficiency	$\sim 43\,\%$
XRT	Focal length	4.75 m
	Field of view	$17'$ at 1.5 keV
		$13'$ at 8 keV
	Effective area	440 cm^2 at 1.5 keV
		250 cm^2 at 8 keV
	Angular resolution	$2'$ (half power diameter: HPD)
XIS	Field of view	$17.'8 \times 17.'8$
	Bandpass	0.2-12 keV
	Pixel grid	1024×1024
	Pixel size	$24\,\mu$m $\times$ $24\,\mu$m
	Enegy resolution	$\sim$ 130 eV at 6 keV (FWHM) and at launch
	Effective area	330 cm^2 (FI), 370 cm^2 (BI) at 1.5 keV
	(incl XRT)	160 cm^2 (FI), 110 cm^2 (BI) at 8 keV
	Time resolution	8 s (normal mode), 7.8 ms (P-sum mode)

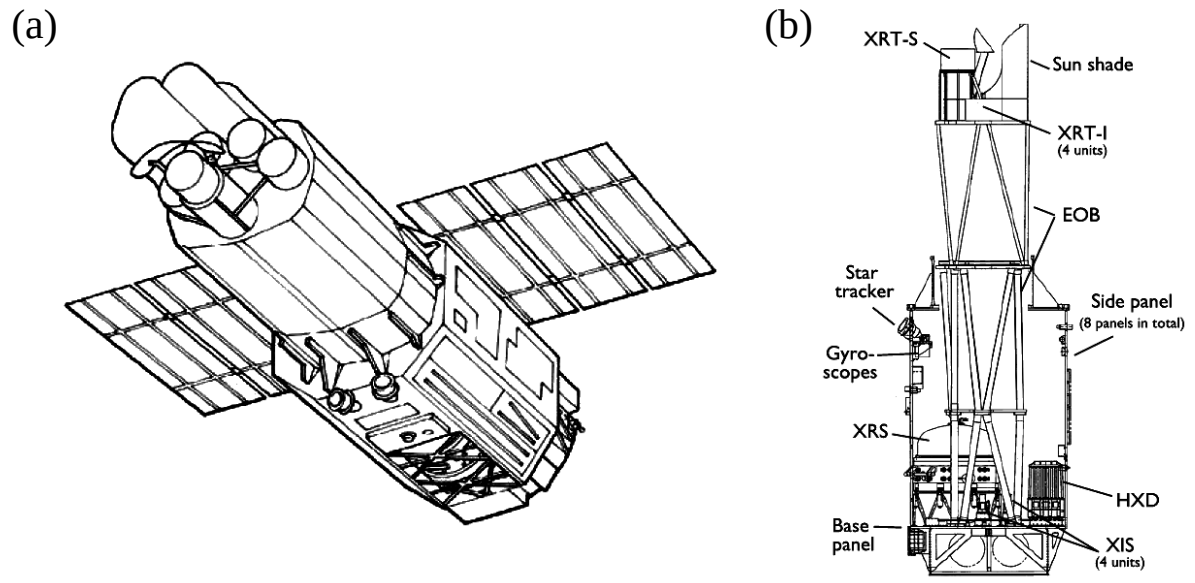

Figure 3.1: (a) Schematic picture of the bottom of the Suzaku satellite. (b) Side view of Suzaku with the internal structures after EOB deployment. (a) and (b) are taken from Figs. 1 and 2 of Mitsuda et al. (2007), respectively.

3.1 XIS

All sensors of the XIS were developed through the collaboration of the Center for Space Research at Massachusetts Institute of Technology, ISAS/JAXA, Osaka Univ., Kyoto Univ., Rikkyo Univ., Kogakuin Univ., and Ehime Univ.

The XIS employs the X-ray CCD, which is operated in a photon-counting mode, similar to that used in the ASCA SIS (Burke et al. 1991; Yamashita et al. 1997), Chandra ACIS (Garmire et al. 1992; Bautz et al. 1998), and XMM-Newton EPIC (Strüder et al. 2001; Turner et al. 2001). In general, an X-ray CCD converts an incident X-ray photon into a charge cloud, with the magnitude of charge proportional to the energy of the absorbed X-ray. This charge is then shifted out onto the gate of an output transistor via an application of a time-varying electrical potential. This results in a voltage level (often referred to as "pulse height") proportional to the energy of the X-ray photon.

The XIS has four sensors (XIS0, XIS1, XIS2, and XIS3), and each sensor has one X-ray CCD chip, which is a MOS-type three-phase CCD operated in the frame transfer mode. A single CCD chip consists of an array of 1024×1024 picture elements ("pixels") and covers an $17.'8 \times 17.'8$ region on the sky, combined with the XRT. Each pixel is $24\,\mu$m square, and the size of the CCD is $25\,\mathrm{mm} \times 25\,\mathrm{mm}$. Three sensors of the XIS (XIS0, 2, and 3) have FI CCDs (energy range 0.4–12 keV), while the other (XIS1) has a BI CCD

(energy range 0.2–12 keV). Since the front side of the CCD has a gate structure made of thin Si (thickness of $\sim$0.28 μm) and SiO_2 (thickness of $\sim$0.44 μm) layers, the FI CCD is less sensitive than the BI CCD to soft X-rays. The surface dead layers of the BI CCD is very thin, consisting of 5 nm HfO_2, 1 nm Ag, and 3 nm SiO_2. In contrast, the BI CCD has a thinner depletion layer ($\sim$42 μm) than the FI CCDs ($\sim$65 μm). Therefore, the quantum efficiency (QE) of the BI CCD at high energy is lower than the FI CCDs. The QEs for the FI and BI CCDs are shown as a function of energy in Fig. 3.2(a).

The energy resolution is defined as the full width at half maximum (FWHM) of the Gaussian function of the main peak. Figure 3.2(b) shows the time history of the energy resolution of the main peak of the calibration line (Mn Kα line emitted from ^{55}Fe). As shown in this figure, the energy resolution of the XIS gradually degrades in the space environment due to the radiation damage by cosmic-ray particles. This degradation can be considered by using the redistribution matrix file (RMF), which is generated by the *xisrmfgen* in FTOOLS, in the spectral fit. On the other hand, Spaced-row Charge Injection (SCI) is used to restore the performance of CCD, especially in the charge transfer efficiency (CTE) and the energy resolution. The SCI has been used by default since AO-2 observations whenever it is possible. The energy resolution at the iron band was improved from $\sim$200–220 eV (FWHM) to $\sim$140–150 eV (FWHM) at September 2007 by the SCI.

Figure 3.3 shows the background counting rate as a function of energy in the 0.5–10 keV range. Here, the background is normalized by the effective area and the field of view. This is a reasonable measure of sensitivity determined by the background for spatially extended sources. Among the instrument listed here, the ASCA SIS had the lowest background, and Suzaku XIS (BI and FI CCD) has a low background comparable to ASCA SIS owing to the low altitude of its orbit. Therefore, the XIS is best suited in the recent X-ray astronomy satellites such as ASCA, Chandra, and XMM-Newton for diffuse and low surface brightness sources owing to its large effective area and low and stable background level. We will study the XIS background in following chapters.

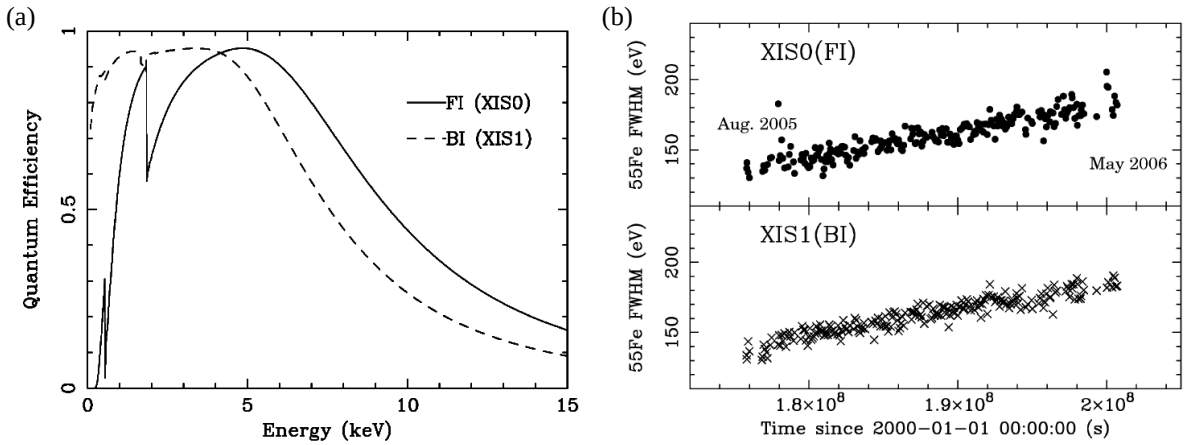

Figure 3.2: (a) The QE as a function of incident energy, calculated using best estimate values of the thickness of dead layers and depletion layer. The solid line represents the FI CCD (XIS0) and the broken line is for the BI CCD (XIS1). (b) The time history of the energy resolution (FWHM) of Mn Kα line from the ^{55}Fe calibration sources for XIS0 (FI: upper) and for XIS1 (BI: lower). (a) and (b) are taken from Figs. 4 and 12 of Koyama et al. (2007a), respectively.

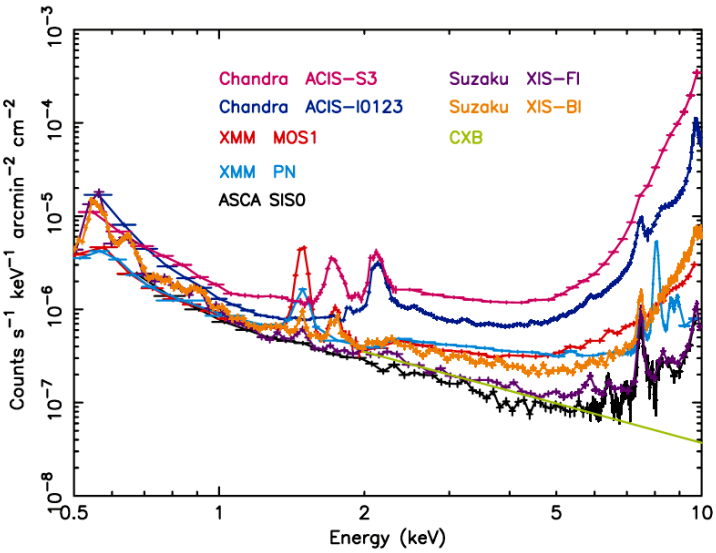

Figure 3.3: XIS background counting rate as a function of energy. The background rate was normalized with the effective area and the field of view, which is a good measure of the sensitivity determined by the background for spatially extended sources. The background rate of ASCA, Chandra, and XMM-Newton adopted from Katayama et al. (2004) are shown for comparisons. This figure is taken from Fig. 5 of Mitsuda et al. (2007).

Chapter 4

Non-X-ray Background

The background of the XIS consists of three components: (1) the NXB; (2) the solar component and (3) the sky X-ray background. While the X-ray background is produced by emission within the XRT FOV, the XIS NXB is caused by charged particles and γ-rays (Mizuno et al. 2004) entering the detector from various directions. Therefore, the NXB varies with time according to the radiation environment of the satellite, i.e. the particle or γ-ray spectra hitting on Suzaku. Since the altitude of orbit of Suzaku is lower than that of XMM-Newton or Chandra, the particle and γ-ray spectra of Suzaku are different from that of XMM-Newton or Chandra. Although these spectra are not entirely clear, their intensities of Suzaku are relatively lower and more stable than those of XMM-Newton or Chandra. In the case of XMM-Newton EPIC, solar soft protons produce flares of up to 10 times of the quiescent background level and affect 30%–40% of XMM-Newton observation time (Carter et al. 2007). However, this component hardly affects Suzaku.

Among the three components of the XIS background, the solar component varies with time, and hence, is the most difficult to model. We try to minimize it by using the orbital and altitude data, which are elevation angles from the day or night Earth edge, and the solar wind data. The sky X-ray background is basically stable and can be evaluated by observation of other fields by Suzaku. We will discuss the solar component and the sky X-ray background in the next chapter. The target of this chapter is to properly estimate the NXB so that we can use it as a background model. It is most important to establish a method to accurately evaluate the NXB spectra and time variations in order to maximize the advantage of the low background level of the XIS. We thus construct an XIS NXB database to be used in the evaluation of the NXB and introduce a method to generate the NXB model given the intensity of charged particles. We also examine and confirm the reproducibility of our NXB model. The contents in this chapter have been already summarized by Tawa et al. (2008) and will be published in PASJ Suzaku 2nd special

issue.

4.1 NXB of the XIS

4.1.1 NXB database

We constructed the database of the XIS NXB from the events collected while Suzaku was pointed toward the night Earth (NTE). Under this condition, the sky X-ray background (3) is blocked, and the solar component (2) does not contaminate. The criteria with which we selected the NTE events are as follows.

- Rev0.7 products (Mitsuda et al. 2007) of which the XIS mode was normal 5×5 or 3×3 mode (without burst or window options). The events were further filtered with the condition of T_SAA_HXD > 436 s, where T_SAA_HXD means time after the passage of the south atlantic anomaly (SAA). This criterion is used in revision 1.2 or 1.3 products (Mitsuda et al. 2007), and this filtering excludes flares in the NXB intensity just after Suzaku passed through the SAA. The events during the telemetry saturation were also excluded.

- The *cleansis* in FTOOLS was applied with the default parameters to exclude the flickering pixels.

- The NTE events were extracted for Earth elevation angles (ELV) less than $-5°$ and Earth day-time elevation angles (DYE_ELV) greater than $100°$.

Since the XIS was in initial operation during August 2005, we collected the NTE events from data observed between September 2005 and May 2006 with the above criteria. The total exposure time of the NTE data is $\sim$785 ks for each XIS. The NXB database[1] consists of the NTE event files and the associated enhanced house keeping (EHK) file, in which orbital information is listed with time. Two associated tools, *mk_corsorted_spec_v1.0.pl* and *mk_corweighted_bgd_v1.1.pl*, to generate the NXB model using the cut-off-rigidity were also prepared. Since the event files in the database can be processed with various FTOOLS including XSELECT, the NXB spectra can be easily created. The subject of this paper is to generate the most appropriate NXB spectra for a given observation.

[1]The first version of the database is accessible via Suzaku web page at ISAS/JAXA ⟨http://www.astro.isas.jaxa.jp/suzaku/analysis/xis/nte/⟩ and GSFC/NASA ⟨http://heasarc.gsfc.nasa.gov/docs/suzaku/analysis/xisbgd0.html⟩, but the NXB data in this database lack T_SAA_HXD and telemetry saturation filtering described here, leading to a total exposure of 800 ks. The second version (the product of this paper) will be released in October 2007.

We hereafter refer to the "NTE events" as the NXB events and refer to the data comprising the NXB events as the "NXB data". Additionally, the "NXB database" indicates the data set which contains the NXB event files and the associated EHK file.

4.1.2 NXB spectra

Figure 4.1 shows the NXB spectra of XIS0 and XIS1. The spectra are extracted from the whole region of the CCD except for the calibration source regions [two corners of the CCD chip (Koyama et al. 2007a)]. The XIS FOV is ∼287 arcmin^2, which is 91% of the FOV of the whole CCD chip. The spectra show fluorescence lines of Al, Si, Au, Mn, and Ni in the XIS and XRT. Table 4.1 shows the intensities of these emission lines, and table 4.2 shows the origin for each fluorescence line. The XIS0 has relatively strong Mn-K emission lines at 5.9 and 6.5 keV as shown in table 4.1. This is due to stray X-rays from the ^{55}Fe calibration source, although why the radiation is detected outside the calibration source regions remains unknown (Yamaguchi et al. 2006). Since the XIS-FIs have a thick neutral layer beneath the depletion layer, most of the background events generated by charged particles produce charge over many pixels and are rejected as ASCA grade 7 events[2]. On the other hand, the XIS1 (BI-CCD) has a relatively thin depletion layer and almost no neutral layer, resulting in relatively many background events in grades 0, 2, 3, 4, and 6 (Yamaguchi et al. 2006). Therefore, the background count rate of the XIS1 is higher than those of the XIS-FIs, especially above ∼7 keV as shown in Fig. 4.1.

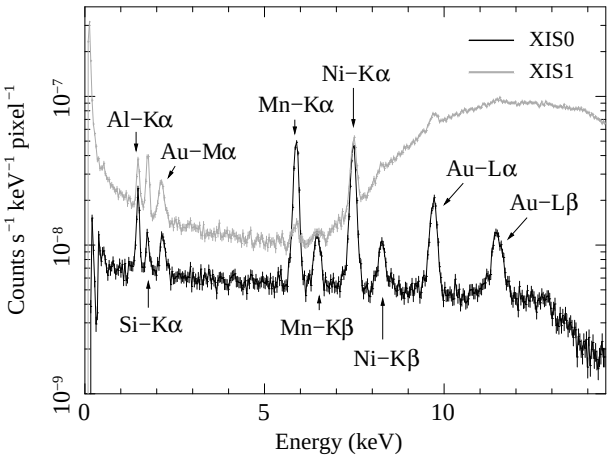

Figure 4.1: Spectra of the NXB in the XIS0 (black) and the XIS1 (gray).

[2]The ASCA grade shows the spread of an event. In the case of the XIS, we consider that most of the X-ray events do not split into a region larger than 2 × 2 pixels. Grade 7 events, in which the spread of event contains more than 2 × 2 pixels, are regarded as background events (Koyama et al. 2007a).

Table 4.1: Energies and count rates of the line components in the NXB spectra.

Line	Energy	Count rate* (10^{-9} cts s^{-1} $pixel^{-1}$)			
	(keV)	XIS0	XIS1	XIS2	XIS3
Al-Kα	1.486	1.45 ± 0.11	1.84 ± 0.14	1.41 ± 0.10	1.41 ± 0.10
Si-Kα	1.740	0.479 ± 0.081	2.27 ± 0.15	0.476 ± 0.080	0.497 ± 0.082
Au-Mα	2.123	0.63 ± 0.093	1.10 ± 0.13	0.776 ± 0.097	0.619 ± 0.092
Mn-Kα	5.895	6.92 ± 0.19	0.43 ± 0.14	1.19 ± 0.13	0.76 ± 0.11
Mn-Kβ	6.490	1.10 ± 0.11	0.26 ± 0.13	0.40 ± 0.11	0.253 ± 0.094
Ni-Kα	7.470	7.12 ± 0.19	7.06 ± 0.37	8.01 ± 0.20	7.50 ± 0.20
Ni-Kβ	8.265	0.96 ± 0.10	0.75 ± 0.22	1.16 ± 0.11	1.18 ± 0.11
Au-Lα	9.671	3.42 ± 0.15	4.15 ± 0.49	3.45 ± 0.15	3.30 ± 0.15
Au-Lβ	11.51	2.04 ± 0.14	1.93 ± 0.48	1.97 ± 0.14	1.83 ± 0.14

* The count rates are obtained from the whole CCD chip excluding the calibration source regions. Errors are 90% confidence level.

Table 4.2: Origins of the fluorescence lines in the NXB spectra.

Line	Origin
Al-Kα	Optical blocking filter, housing, alumina substrate to mount CCD
Si-Kα	CCD (Si fluorescence line)
Au-Mα, Lα, Lβ	Housing, CCD substrate, heatsink
Mn-Kα, Kβ	Scattered X-rays from calibration sources
Ni-Kα, Kβ	Housing, heatsink

4.1.3 Positional dependencies

The NXB is not uniform over the CCD chip. Figure 4.2 shows the NXB count rates of the continuum component (2.5–5.5 keV band) and the Ni-Kα line (7.2–7.8 keV band) as a function of "ACTY". Actual coordinate (ACTX and ACTY) defines the actual pixel position on the CCD imaging area. These count rates tend to be slightly higher at larger ACTY. This is because some fraction of NXB is produced in the frame-store region. The fraction may be different between the fluorescent lines and the continuum, which causes slight difference in the ACTY dependence of the NXB.

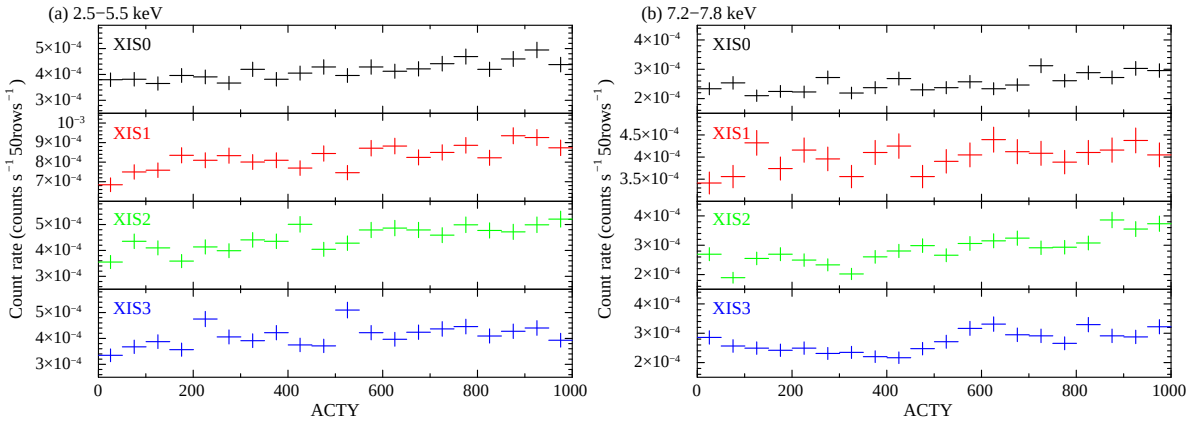

Figure 4.2: The NXB count rates of (a) the continuum component (2.5–5.5 keV band) and (b) the Ni-Kα line (7.2–7.8 keV band) as a function of ACTY. These count rates tend to be slightly higher at larger ACTY.

In addition, we find the positional dependence of the Mn-Kα line in the XIS0 as shown in Fig. 4.3(a). In contrast, the other sensors (XIS1, 2, 3) do not have this dependence, e.g., as shown in Fig. 4.3(b). This is thought to be due to stray X-rays from the ^{55}Fe calibration source as well as the strong Mn-K emission lines of the XIS0 (subsection 4.1.2), although details are not well understood.

We have to be careful about these dependences when the NXB is subtracted. Details about the NXB subtraction procedure will be described in section 4.3.

4.1.4 Cut-off-rigidity and PIN-UD

Since the NXB is caused by charged particles, the NXB should depend on the intensity of charged particles striking Suzaku, and this is strongly correlated with the geomagnetic cut-off-rigidity. We introduce a new type of cut-off-rigidity, *COR2*, for Suzaku. The calculation for the *COR2* is independent from that for the conventional cut-off-rigidity,

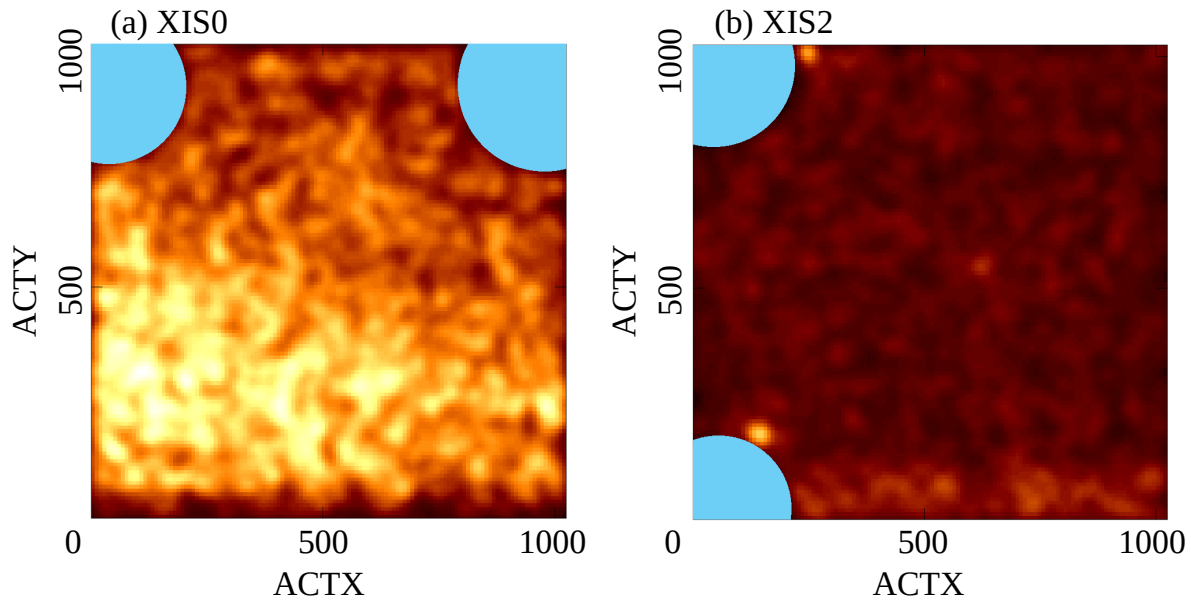

Figure 4.3: The NXB images in the 5.7–6.0 keV band (Mn-Kα) of (a) the XIS0 and (b) the XIS2. The color scale is the same in both images. The regions drawn with cyan color represent the calibration source regions.

COR. The *COR* has been employed in the analysis of Tenma, Ginga, ASCA, and Suzaku. We summarize the characteristics of *COR* and *COR2* in appendix A. In the main text, we use *COR2* when discussing the NXB.

Suzaku carries a non-imaging hard X-ray instrument, the Hard X-ray Detector (HXD). The HXD sensor contains 4×4 well-type phoswich units (well units) with 4 PIN silicon diodes in each (Takahashi et al. 2007; Kokubun et al. 2007). When a charged particle generates a large signal in a PIN silicon diode, the PIN upper discriminator (PIN-UD) is activated at a threshold around 90 keV. This can be a good monitor of the real-time intensity of the charged particles striking Suzaku. The number of PIN-UD counts is recorded with each well unit. We sum up the PIN-UD count rates for all well units and average them for each 32 seconds to reduce the statistical error. The typical number of PIN-UD counts in 32 seconds is $\sim$5100 counts by summing up all well units. We hereafter call this count rate the PIN-UD. Figure 4.4 shows the PIN-UD as a function of the *COR2*. There is a strong anti-correlation between the PIN-UD and the *COR2*. However, the anti-correlation is widely distributed. This is because that the PIN-UD mirrors the real-time intensity of the charged particles, while the *COR2* is calculated from a COR map (shown in Fig. A.1(b)) and the orbital position of Suzaku. Therefore, the *COR2* might not correctly reproduce the real-time intensity of the charged particles. In addition, some events deviate from the correlation as shown in the region of A and

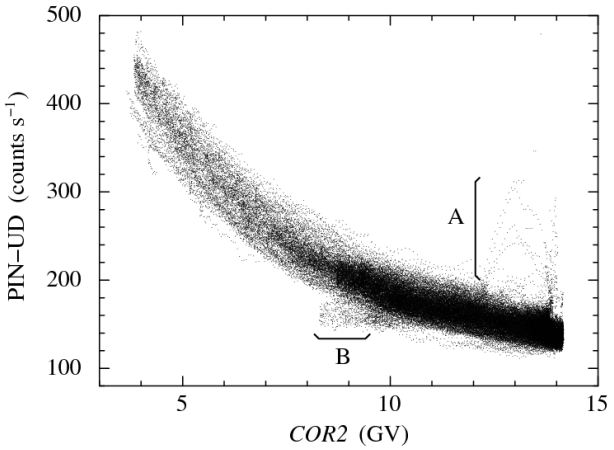

Figure 4.4: The PIN-UD is anti-correlated with the *COR2*, although there is noticeable scatter such as the region of A and B. The events in region A occurred just before Suzaku entered the SAA. The events in region B occurred at the time when Suzaku passed near the region of (longitude, latitude) = (350°, 19°).

B of Fig. 4.4. The events in region A occurred just before Suzaku entered the SAA. The events in region B occurred at the time when Suzaku passed near the region of (longitude, latitude) = (350°, 19°). We assume that this is because the *COR2* values in this region are approximately calculated as shown in appendix A. However, the number of events in regions A and B is less than 1% of the total number of events. We will discuss which parameters of the *COR2* or PIN-UD can correctly reproduce the NXB in the next section.

Figure 4.5(a) shows the count rate of the NXB for each XIS in the 5–12 keV energy band as a function of the *COR2*. The count rate of each bin of XIS1 is about 6 times higher than those of XIS-FIs. This is because the XIS1 has a relatively thin depletion layer and almost no neutral layer, as discussed in section 2.2. Therefore, the NXB intensity of XIS1 depends on the intensity of charged particles as well as the XIS-FIs. On the other hand, spectra are different between the low *COR2* region (*COR2* $\leq$ 8 GV) and high *COR2* region (*COR2* $>$ 8 GV) as shown in Figure 4.5(b). The differences mainly appear in normalization of the spectra. The periods of the NXB variations primarily correspond to the orbital period of Suzaku, 96 minutes, since the NXB depends on the cut-off rigidity. We should also note that the NXB does not have apparent long-term changes in 9 months. For details, we will discuss in sections 3.3 and 4.

Since the *COR2* and the NXB count rate are anti-correlated, we can use the *COR2* to estimate the NXB spectra to be subtracted as background for a given observation. The PIN-UD can also be used as such a parameter to estimate the NXB spectra, considering

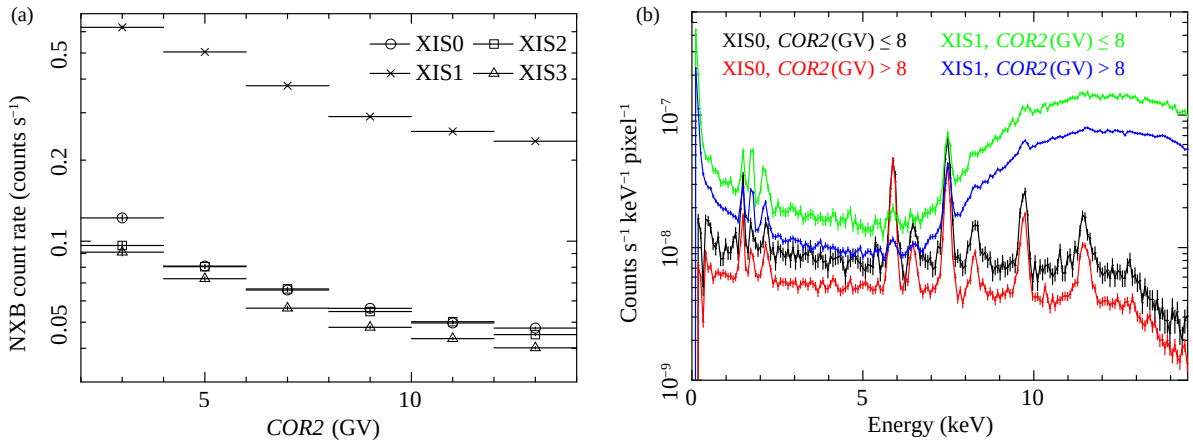

Figure 4.5: (a) *COR2* dependence of the NXB (average count rate in 5–12 keV) for each XIS. (b) NXB spectra in *COR2* $\leq$ 8 and *COR2* $>$ 8 GV. Black and red lines show the XIS0 spectra. Green and blue lines show the XIS1 spectra. The NXB count rate is anti-correlated with the *COR2*, and the count rate of XIS1 is higher than those of XIS-FIs.

the anti-correlation between the *COR2* and the PIN-UD. In the following section, we will attempt to model the NXB spectra from the NXB data by employing either of the *COR2* or the PIN-UD. The two kinds of NXB models, one with the *COR2* and the other with the PIN-UD, will be compared by their reproducibilities.

4.2 NXB models and their Reproducibility

4.2.1 NXB models: NXB data sorted by *COR2* or PIN-UD

In order to correctly subtract the NXB from on-source observation, we introduce method to model the NXB. Since the spectra of charged particles and γ-ray causing the NXB are not fully understood, this is a semi-empirical method. We prepared two tools, *mk_corsorted_spec* and *mk_corweighted_bgd*[3], to generate the NXB model. *Mk_corsorted_spec* is to sort with modeling parameter, i.e. *COR2* or PIN-UD, bin and generates the NXB spectra for each modeling parameter bin. *Mk_corweighted_bgd* is to generate the NXB model spectrum for a given on-source observation by summing up the sorted spectra with

[3]These tools are new versions of *mk_corsorted_spec_v1.0.pl* and *mk_corweighted_bgd_v1.1.pl*. *mk_corsorted_spec_v1.0.pl* and *mk_corweighted_bgd_v1.1.pl* support the *COR* only. These new tools were merged in one and were released as *xisnxbgen* in FTOOLS in HEAsoft version 6.4 at December 2007. The NXB data were also included in CALDB and will be periodically updated. Hereafter, the *xisnxbgen* should be used.

appropriate weights. The weighted NXB model spectrum, S_w, is expressed as follows,

$$S_w = \frac{\sum_{i=1}^{n} T_i S_i}{\sum_{i=1}^{n} T_i} = \sum_{i=1}^{n} \frac{T_i}{T_{total}} S_i \ , \tag{4.1}$$

where the modeling parameter is sorted into n bins. T_i and S_i are the exposure time of the on-source observation and the spectrum of the NXB data in the ith modeling parameter bin, respectively. T_{total} is the total exposure time of the on-source observation. Equation (4.1) makes equal the modeling parameter distribution for the on-source observation and that for the NXB data.

We sorted the NXB and on-source data into 14 bins with either the *COR2* or PIN-UD. The *COR2* and PIN-UD bins are defined as shown in table 4.3. In addition, table 4.3 shows the NXB count rate (5-12 keV) and exposure time for each *COR2* and PIN-UD bin in the XIS0. We defined the bin ranges at even intervals of the PIN-UD and set the *COR2* bins so as to get the approximately comparable count rate of the corresponding PIN-UD bins. We should note that the NXB model obtained by sorting into even intervals with the exposure time has comparable level to that by sorting into the bins shown in table 4.3.

4.2.2 Reproducibility of the NXB models

We first calculate the intrinsic variability of the NXB data to compare with the reproducibility of the NXB model. The standard deviation of the NXB count rate contains the systematic error and statistical error. We define the systematic error (1σ confidence level) as the intrinsic variability. To calculate the intrinsic variability, we divide the NXB data into 5 ks exposure bins (generally spanning a few days) and obtain the count rate for each. Since the NXB intensity is particularly low, the count rates are obtained in the 5–12 keV energy band to reduce the statistical error. There are typically 250 counts per 5 ks exposure bin in this energy range for the XIS-FIs. Figure 4.6 shows the distribution of this count rate, hereafter called C_j for the jth bin. We calculate the standard deviation of C_j (σ_c) as follows,

$$\sigma_c^2 = \frac{1}{n-1} \sum_{j=1}^{n} (C_j - \mu_c)^2 \ , \tag{4.2}$$

where n is the number of the 5 ks NXB data, and μ_c is the average of C_i, $\mu_c = (1/N) \sum_{j=1}^{n} C_j$. Then, the statistical error of C_j is assumed by Poisson statistics and is calculated by $\sqrt{C_j/T_j}$, where T_j is a exposure time of the jth bin (in this case, T_j is 5 ks). Since we divided the NXB data into 5 ks exposure, the statistical error of each C_j is approximately

Table 4.3: The PIN-UD and the *COR2* bins ranges.

Bin #	PIN-UD	Count rate*	Exposure†	*COR2*	Count rate*	Exposure†
	(cts s^{-1})	10^{-2} (cts s^{-1})	(ks)	(GV)	10^{-2} (cts s^{-1})	(ks)
1	100–150	4.551 ± 0.051	175.4	15–12.8	4.746 ± 0.048	208.3
2	150–175	4.857 ± 0.045	236.6	12.8–10.5	4.877 ± 0.045	246.2
3	175–200	5.329 ± 0.062	137.7	10.5–9.1	5.347 ± 0.061	142.6
4	200–225	5.533 ± 0.089	70.0	9.1–8.1	5.73 ± 0.10	53.6
5	225–250	6.24 ± 0.15	28.3	8.1–7.3	6.24 ± 0.15	27.6
6	250–275	6.74 ± 0.18	20.7	7.3–6.6	6.49 ± 0.18	19.2
7	275–300	6.85 ± 0.20	17.9	6.6–6.0	7.17 ± 0.20	17.5
8	300–325	7.83 ± 0.23	14.3	6.0–5.5	7.29 ± 0.24	13.0
9	325–350	7.42 ± 0.23	13.6	5.5–5.1	7.83 ± 0.27	10.8
10	350–375	8.35 ± 0.26	12.5	5.1–4.7	7.52 ± 0.25	12.2
11	375–400	9.33 ± 0.27	12.4	4.7–4.3	8.60 ± 0.28	11.3
12	400–425	10.61 ± 0.31	10.8	4.3–4.0	9.55 ± 0.32	9.5
13	425–450	11.53 ± 0.48	4.9	4.0–3.7	11.37 ± 0.39	7.3
14	450–500	7.4 ± 1.3	0.4	3.7–2.0	13.74 ± 0.59	4.0

* The count rates are obtained from the NXB data of the XIS0 in the 5–12 keV band. Errors are 1σ confidence level.

† The exposure times are obtained from the NXB data of the XIS0.

constant. We therefore obtain the statistical error contained in σ_c ($\sigma_{sta,c}$) as follows,

$$\sigma_{sta,c} = \frac{1}{n}\sum_{j=1}^{n}\sqrt{\frac{C_j}{T_j}} \ . \tag{4.3}$$

We then calculate the systematic error ($\sigma_{sys,c}$) as follows,

$$\sigma_{sys,c} = \sqrt{\sigma_c^2 - \sigma_{sta,c}^2} \ . \tag{4.4}$$

$\sigma_{sys,c}$ is the intrinsic variability and is summarized in table 4.4. The intrinsic variability shows the reproducibility of the NXB without being modeled. Details about the errors of σ_c, $\sigma_{sta,c}$, and $\sigma_{sys,c}$ shown in table 4.4, are presented in appendix B.

We next calculate the reproducibility of NXB model described in eq. (4.1). The NXB spectra, S_i in eq. (4.1), are obtained from the NXB data according to the modeling parameter. The weights of each bin, T_i/T_{total} in eq. (4.1), are calculated by the modeling parameter for each 5 ks NXB data bin. We thus obtained the NXB models for each 5 ks bin and calculated the residual, data minus model. The jth residual (ΔC_j) is calculated by $C_j - M_j$, where M_j is the count rate of the NXB model for the jth 5 ks NXB data bin. There are two kinds of ΔC_j, ΔC_{COR2} and $\Delta C_{\rm PIN-UD}$, which are calculated based on the *COR2* and the PIN-UD, respectively. Figure 4.7 shows the distributions of ΔC_{COR2} and $\Delta C_{\rm PIN-UD}$ in the 5–12 keV energy band. These distributions are relatively narrow compared with the distribution of C_j shown in Fig. 4.6. This indicates that the NXB models correctly reproduce the NXB data. Since the way to calculate the reproducibility is the same with ΔC_{COR2} and $\Delta C_{\rm PIN-UD}$, we express this with ΔC_j. The standard deviation of ΔC_j ($\sigma_{\Delta c}$) is calculated as follows,

$$\sigma_{\Delta c}^2 = \frac{1}{n-1}\sum_{j=1}^{n}(\Delta C_j - \mu_{\Delta c})^2 \ , \tag{4.5}$$

where $\mu_{\Delta c}$ is the average of ΔC_j and is expected to be zero. The statistical error of ΔC_j is $\sqrt{C_j/T_j + M_j/T}$, where T is total exposure time of the NXB data. The average of these statistical errors ($\sigma_{sta,\Delta c}$) is expressed as follows,

$$\sigma_{sta,\Delta c} = \frac{1}{n}\sum_{j=1}^{n}\sqrt{\frac{C_j}{T_j} + \frac{M_j}{T}} \ . \tag{4.6}$$

Since $T \sim 157 T_j$, the value of $\sigma_{sta,\Delta c}$ is approximately $\sigma_{sta,c}$ (eq. 4.3). By using $\sigma_{\Delta c}$ and $\sigma_{sta,\Delta c}$, the systematic error of ΔC_j ($\sigma_{sys,\Delta c}$) is calculated as follows,

$$\sigma_{sys,\Delta c} = \sqrt{\sigma_{\Delta c}^2 - \sigma_{sta,\Delta c}^2} \ . \tag{4.7}$$

Hear $\sigma_{sys,\Delta c}$ is defined as the "reproducibility" of the NXB model. We independently calculate the reproducibility for each XIS and show them in table 4.5(a). Details about the errors of the reproducibilities are presented in appendix B. Since the PIN-UD sometimes exceeds the range of 100–500 cts s^{-1}, the total exposure time reduces to ∼760 ks. On the other hand, for the NXB model with the *COR2*, the whole NXB data set of ∼785 ks is available. The reproducibilities of the NXB models (table 4.5a) are about 1/3 of the intrinsic variability of the NXB count rate (table 4.4). However, the residuals sometimes becomes large in both NXB models, as shown in Fig. 4.7.

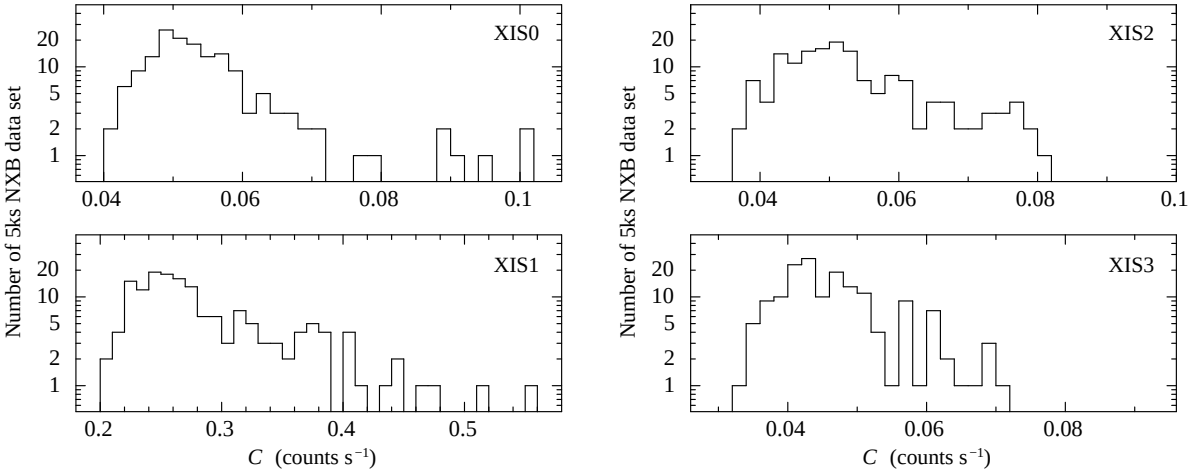

Figure 4.6: Distribution of C_j in the XIS0, 1, 2, and 3. C_j is calculated in the 5–12 keV energy band.

Table 4.4: Statistical summary of the NXB data.

Sensor	Average count rate* 10^{-2} (cts s^{-1})	Standard deviation† (%)	Statistical error† (%)	Intrinsic variability† (%)
XIS0	5.464 ± 0.026	19.2 ± 1.1	6.03 ± 0.34	18.2 ± 1.1
XIS1	28.758 ± 0.060	22.5 ± 1.3	2.62 ± 0.15	22.4 ± 1.3
XIS2	5.317 ± 0.026	19.1 ± 1.1	6.11 ± 0.35	18.1 ± 1.1
XIS3	4.685 ± 0.024	16.85 ± 0.95	6.51 ± 0.37	15.5 ± 1.0

* The count rates are obtained from the NXB data in the 5–12 keV band. Errors are 1σ confidence level.

† These values are normalized by the average count rate.

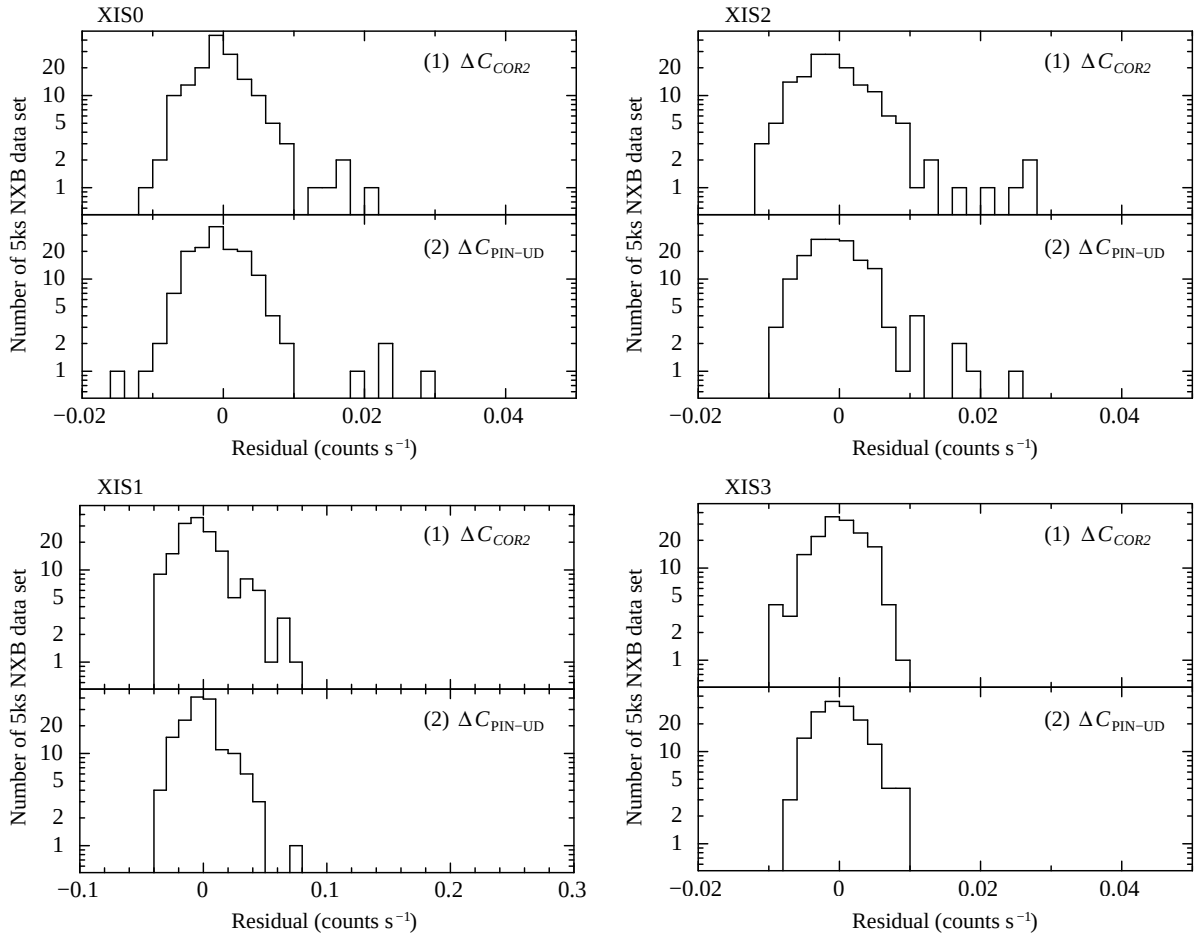

Figure 4.7: Distributions of (1) ΔC_{COR2}, and (2) $\Delta C_{\rm PIN-UD}$ in the XIS0, 1, 2, and 3.

4.2.3 Improvements to the NXB model by filtering the data

To further improve the reproducibilities of the NXB models, we examined the time and orbital position of Suzaku when the count rate significantly deviates from the NXB model, i.e. > 0.01 cts s^{-1} for the XIS-FIs in Fig. 4.7. We found that those data are obtained from 2005/10/09 ($t = 1.822 \times 10^8$ s, where t is time since 2000/01/01 00:00:00) to 2005/10/28 ($t = 1.838 \times 10^8$ s) and from 2005/11/29 ($t = 1.866 \times 10^8$ s) to 2005/12/20 ($t = 1.884 \times 10^8$ s). We call these time periods period-A. Figure 4.8 shows the light curve of ΔC_{PIN-UD}. The count rate of ΔC_{PIN-UD} increase at the first time period of period-A, especially in the XIS0.

Figure 4.9(a) shows the orbital position during period-A, and Fig. 4.9(b) shows the orbital position at other times. These plots indicate that the residuals increase when Suzaku passes through high latitude and high altitude region. We therefore exclude the NXB events during the time when the orbital positions of Suzaku were latitude $\leq -23°$, altitude ≥ 576.5 km or latitude $\geq 29°$, altitude ≥ 577.5 km (hereafter the "orbit filter") from the NXB data. The total exposure time of the NXB data with the orbit filter (hereafter "*NXB1*") is $\sim$730 ks, while that with the PIN-UD is $\sim$710 ks. The reproducibilities of the NXB models for the *NXB1* data are independently evaluated for each XIS by the same way as that in section 4.2.2 . Figure 4.10(a) shows the distribution of $\Delta C_{\rm PIN-UD}$ obtained from the *NXB1* data, and table 4.5(b) shows their reproducibilities. We can improve reproducibilities by employing the orbit filter. Especially, the reproducibility of the XIS0 is 3 times better than that without orbit filter.

The NXB model of XIS2 with the orbit filter applied has almost the same level of the reproducibility as that without the orbit filter. In addition, the reproducibility of XIS2 is the worst among the XIS-FIs (XIS0, 2, 3) (table 4.5a and b). We therefore investigate the long-term variation of the NXB intensity. Figure 4.11 shows the light curve of $\Delta C_{\rm PIN-UD}$ obtained from the *NXB1* data. We found that $\Delta C_{\rm PIN-UD}$ during September 2005 had been higher than that after October 2005, especially in the XIS2. We speculate that this is because the solar activity was particularly high during September 2005. The proton and solar X-ray intensities are continuously monitored by the Geostationary Operational Environmental Satellites (GOES)[4]. These intensities in September 2005 frequently exceeded 100 times those of the normal state of the Sun. We fitted the light curve after October 2005 with a linear function, finding that the NXB intensities of the XIS-FIs were constant with time within $\pm 6\%$ per year. On the other hand, the NXB intensity of XIS1 decreased with a gradient of $(-7.8 \pm 5.8)\%$ per year (90% confidence level). However, since the gradient is small, we continue to apply the same method of modeling as the

[4]The GOES data are available at ⟨http://www.ngdc.noaa.gov/stp/GOES/goes.html⟩

XIS-FIs to XIS1.

We therefore exclude the NXB events during September 2005 from the *NXB1* data (hereafter "*NXB2*") and independently evaluate their reproducibilities for each XIS. Figure 4.10(b) shows the distribution of $\Delta C_{\rm PIN-UD}$ obtained from the *NXB2* data, and table 4.5(c) shows their reproducibilities. Better reproducibilities than the unfiltered NXB data can be obtained for all the XIS. In addition, we found that the NXB model with the PIN-UD has better reproducibility than that with the *COR2*. The total exposure time of this *NXB2* data is ∼560 ks, but for the PIN-UD model, the exposure time is ∼550 ks. Since the exposure time is long enough, excluding the data during September 2005 is not a serious problem for the observations after October 2005.

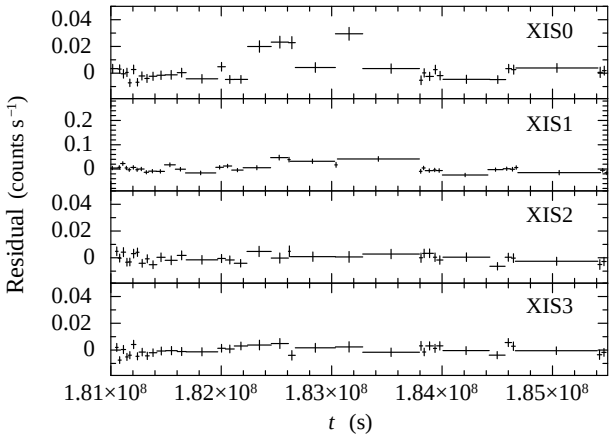

Figure 4.8: Light curve of $\Delta C_{\rm PIN-UD}$ in the XIS0, 1, 2, and 3. The residuals are obtained from the unfiltered NXB data in the 5–12keV band.

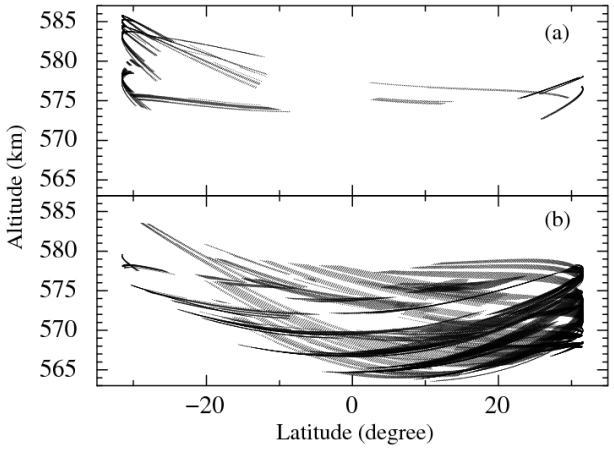

Figure 4.9: Orbital positions of Suzaku for XIS observations of the NTE during (a) period-A and (b) other times.

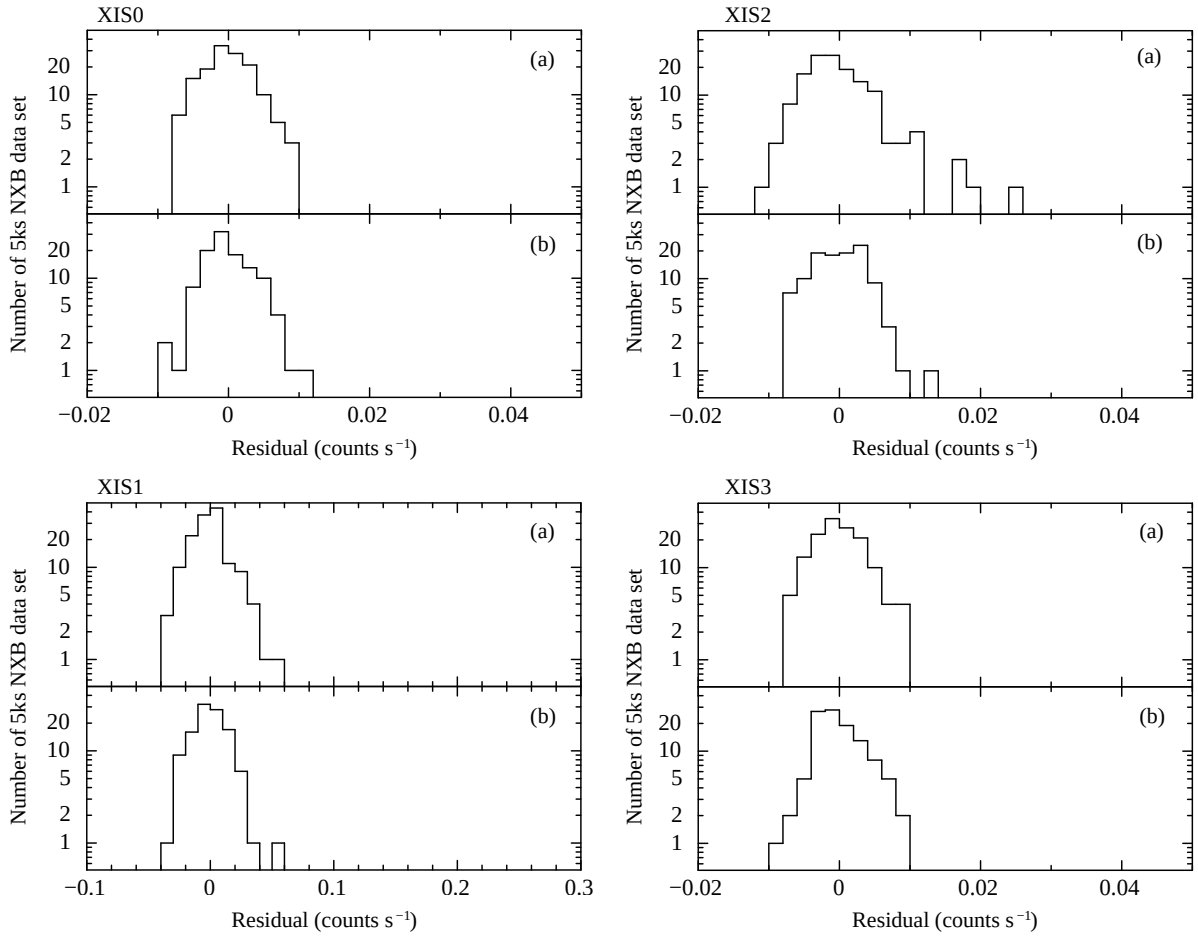

Figure 4.10: Distribution of $\Delta C_{\mathrm{PIN-UD}}$ in the XIS0, 1, 2, and 3. The residuals are obtained from (a) the *NXB1* and (b) the *NXB2* data in 5–12 keV energy band.

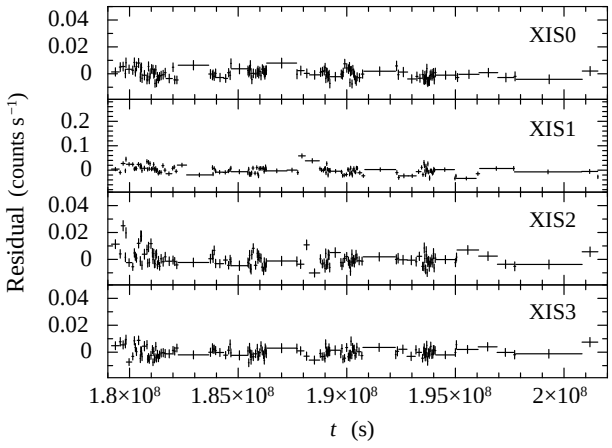

Figure 4.11: Light curve of $\Delta C_{\mathrm{PIN-UD}}$ in the XIS0, 1, 2, and 3. The residuals are obtained from the *NXB1* data in 5–12 keV energy band.

Table 4.5: Reproducibilities of two kinds of the NXB models which are calculated for the 5 ks NXB data in the 5–12 keV energy band.

NXB	Sensor	*COR2**(%)	PIN-UD* (%)
(a) Unfiltered	XIS0	6.60 ± 0.61	8.12 ± 0.68
	XIS1	7.18 ± 0.46	5.57 ± 0.39
	XIS2	10.33 ± 0.77	7.85 ± 0.68
	XIS3	3.32 ± 0.56	3.42 ± 0.57
(b) *NXB1*	XIS0	4.05 ± 0.55	2.67 ± 0.53
	XIS1	6.32 ± 0.43	4.81 ± 0.36
	XIS2	9.77 ± 0.76	8.49 ± 0.72
	XIS3	4.09 ± 0.59	4.11 ± 0.60
(c) *NXB2*	XIS0	3.54 ± 0.61	2.79 ± 0.60
	XIS1	6.95 ± 0.53	4.36 ± 0.39
	XIS2	5.67 ± 0.69	3.96 ± 0.64
	XIS3	2.34 ± 0.64	3.82 ± 0.68

* These values are normalized by the average count rate shown in table 4.4. Errors are 1σ confidence level.

4.2.4 Reproducibility of the NXB for the 1–7 keV band

We evaluate the reproducibility of the NXB in the 1–7 keV energy band by the same method as that in section 4.2.2. The CXB is dominant compared with the NXB in this energy band. Table 4.6 shows the average count rate, statistical error, and reproducibility for the 5 ks *NXB2* data. The reproducibilities are as good as those for the 5–12 keV energy band (table 4.5c), and the NXB model with the PIN-UD has better reproducibility than that with the *COR2*.

Table 4.6: Reproducibilities of the NXB models which are calculated by dividing the *NXB2* data into 5 ks exposure bins in the 1–7 keV energy band.

Sensor	Average count rate	Statistical error*	Reproducibility*	
	10^{-2} (cts s^{-1})	(%)	*COR2* (%)	PIN-UD (%)
XIS0	4.163 ± 0.027	6.94 ± 0.47	5.06 ± 0.74	4.55 ± 0.74
XIS1	7.321 ± 0.036	5.22 ± 0.35	7.55 ± 0.71	5.63 ± 0.63
XIS2	3.871 ± 0.026	7.19 ± 0.49	7.31 ± 0.84	5.18 ± 0.78
XIS3	3.475 ± 0.025	7.59 ± 0.52	6.34 ± 0.84	4.76 ± 0.80

* These values are normalized by the average count rate. Errors are 1σ confidence level.

4.2.5 Reproducibility with longer exposure data

We have so far calculated the NXB reproducibility by dividing the NXB data into each 5 ks exposure bins. Here we examine the NXB reproducibility for a longer exposure time of 50 ks, typical for on-source observations. Each 50 ks NXB exposure typically spans a few weeks. Table 4.7 shows the reproducibilities of the NXB models for the exposure time of 50 ks in the energy bands of 1–7 keV and 5–12 keV. The reproducibilities of the 50 ks NXB models are improved from those for the 5 ks NXB models. This is because fluctuations of the residuals are smoothed by integrating for a long time.

4.3 Subtraction of the NXB from on-source observation

In this section, we consider the practical manner of how to subtract the NXB for on-source science observations. First, since the intensity of the NXB is not uniform over

Table 4.7: Reproducibilities of the NXB models which are calculated by dividing the *NXB2* data into 50 ks exposure bins.

Energy range (keV)	Sensor	Statistical error* (%)	Reproducibility*	
			COR2 (%)	PIN-UD (%)
$1-7$	XIS0	2.29 ± 0.54	1.89 ± 0.84	2.02 ± 0.90
	XIS1	1.72 ± 0.39	2.61 ± 0.80	2.70 ± 0.81
	XIS2	2.37 ± 0.56	1.73 ± 0.84	0.31 ± 0.79
	XIS3	2.50 ± 0.59	2.08 ± 0.92	1.20 ± 0.88
$5-12$	XIS0	1.96 ± 0.46	1.03 ± 0.66	1.89 ± 0.79
	XIS1	0.85 ± 0.19	2.98 ± 0.72	2.36 ± 0.59
	XIS2	1.98 ± 0.47	1.87 ± 0.75	1.20 ± 0.72
	XIS3	2.14 ± 0.50	1.51 ± 0.75	0.40 ± 0.72

* These values are normalized by the average count rate in the energy bands of the 1–7 keV (table 4.6) or the 5–12 keV (table 4.4). Errors are 1σ confidence level.

the CCD chip as shown in Figs. 4.2 and 4.3, the NXB spectrum needs to be extracted from the same region as the on-source spectrum in detector (DET) coordinates (Ishisaki et al. 2007). We can extract the NXB spectra sorted by the cut-off-rigidity for a given region defined in the DET coordinate with the *mk_corsorted_spec* (same applies to the *mk_corsorted_spec_v1.0.pl*). Next, the sorted NXB spectra are summed up with appropriate weights calculated for the on-source observation using the *mk_corweighted_bgd* (same applies to the *mk_corweighted_bgd_v1.1.pl*). The summed-up spectrum is the NXB model to be subtracted from on-source spectra.

One of the problems in this procedure is the presence of emission line components in the NXB spectra. These components are time-dependent; the energy resolution of the XIS degrades with time (Koyama et al. 2007a), and the intensities of the Mn-K emission lines decrease with the half life of ^{55}Fe, 2.73 years. Since the NXB data contained in the NXB database are made from the NXB events between September 2005 and May 2006 and this time dependence is not taken into account, the emission line components in the NXB spectra cannot be reproduced correctly for a given on-source observation. This problem becomes prominent for the observations after June 2006. Figure 4.12 shows an example of a raw on-source spectrum and the NXB model spectrum which we have described above. These are the averaged spectra of the XIS-FIs, hereafter called "FI spectra".

Figure 4.13(a) shows the on-source spectrum from which the NXB model spectrum is subtracted, black minus red line shown in Fig. 4.12. This on-source spectrum is obtained in the observation of the link region between the galaxy clusters A 399 and A 401 taken during August 19–22 2006 with an exposure time of 150 ks (observation ID is 801020010. For details, see Fujita et al. 2008). The model in Fig. 4.13(a) is a single thermal model (APEC in XSPEC) plus power-law model. The thermal model represents the ICM, and the power-law model represents the CXB. These are same models used by Fujita et al. (2008). Significant residuals are visible at the energies of Mn-Kα (5.9 keV) and Ni-Kα (7.4 keV) in Fig. 4.13(a). We have therefore developed a way to deal with these emission line components in the NXB spectra, as follows[5]:

1. The NXB model spectrum is constructed with the *COR2* or the PIN-UD using the method described in subsection 4.2.1.

2. The line components Mn-Kα, Mn-Kβ, Ni-Kα, Ni-Kβ, and Au-Lα, in the NXB model spectrum are fitted with the RMF for August 2005 observations, at which point the degradation of the energy resolution was negligible. For example, in the energy range of 5.5–7.0 keV where there are Mn-Kα and Mn-Kβ lines, the spectrum is fitted with two Gaussians plus a power-law continuum. We have set the line widths of the two Gaussian components as free parameters. The emission lines of Ni-Kα, Ni-Kβ, and Au-Lα are similarly fitted.

3. We simulate the spectrum of the five Gaussian components using the *fakeit* command in XSPEC, using the fitting parameters determined in step 2.

4. The spectrum created in the step 3 is subtracted from the NXB model spectrum from step 1. This should correspond to the NXB continuum spectrum from which the five Gaussian line components are removed.

5. We add the simulated line components to the NXB continuum spectrum created in step 4, using the *fakeit* command. To take into account the degradation of energy resolution, this simulation needs to be done with the RMF calculated for the epoch of the on-source observation by using the *xisrmfgen* command (version 2006-11-26) in FTOOLS. The *xisrmfgen* is a response generator for the Suzaku XIS. The normalizations and line center energies of the five Gaussian components are fixed with those obtained in step 2, though radioactive decay of ^{55}Fe is taken into account. The intrinsic widths of these lines are fixed to be zero. We then get the NXB model

[5]Note that this procedure is not considered in the *xisnxbgen*.

spectrum in which degradation in the energy resolution and the ^{55}Fe decay are taken into account.

The NXB model spectrum with the correction for the emission line components is shown as a green line in Fig. 4.12. The line widths of this spectrum are larger than those of the NXB model spectrum without the correction (red line shown in Fig. 4.12). Additionally, the intensities of Mn-K lines decrease with the correction. Figure 4.13(b) shows the on-source spectrum from which the NXB model with the correction for the emission line components is subtracted. The model in Fig. 4.13(b) is the same as that in Fig. 4.13(a). This correction can reduce the residuals in the energy bands including Mn-Kα and Ni-Kα, improving the reduced χ^2 from 1.77 to 1.16, in this case.

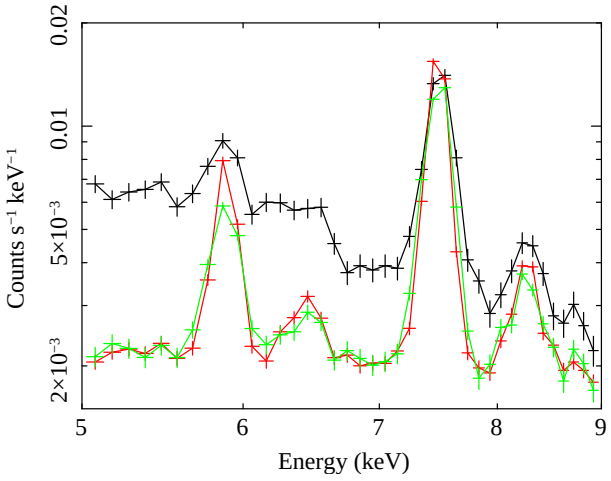

Figure 4.12: (black) On-source observation spectrum. (red) The NXB model spectrum without the correction for the emission line components. (green) The NXB model spectrum with the correction for the emission line components. These are averaged spectra of the XIS-FIs.

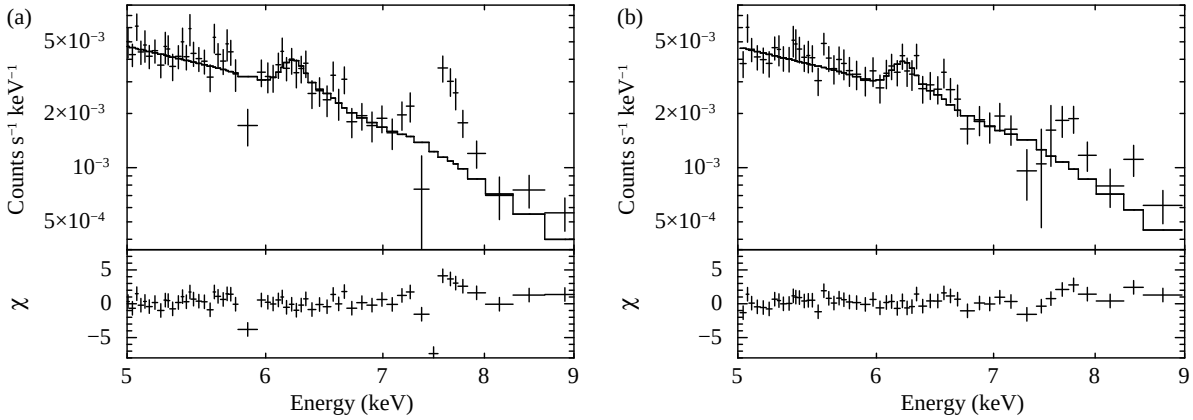

Figure 4.13: On-source observation with or without the correction for the emission line components. (a) The FI spectrum from which the NXB model spectrum is subtracted without the correction for the emission line components. (b) The FI spectrum from which the NXB model spectrum is subtracted with the correction for the emission line components.

Chapter 5

X-ray Background

The XIS background consists of three components: (1) the NXB, (2) the solar component, and (3) the sky X-ray background. We have discussed the NXB in chapter 4. The other two components, (2) and (3), depend on the position of the CCD chip, time, and direction of the sky. Therefore, we describe these components in this chapter.

5.1 Solar component

The solar component includes the fluorescence lines of nitrogen and oxygen from the earth's atmosphere and scattered solar X-rays. The intensity of the solar component depends on both the solar activity and elevation angle from the sunlit earth edge. Figure 5.1 shows the XIS1 spectra of the north ecliptic pole (NEP) (shown in table 5.1) as a function of the DYE_ELV. These spectra have been screened with the same criteria as the cleaned event file (subsection 5.2.2), excluding the DYE_ELV. The spectrum filtered with $5^\circ <$ DYE_ELV $< 10^\circ$ has strong lines of Ni I Kα and O I Kα, while these lines are weak when the DYE_ELV is large. In contrast, the O VII Kα line remains almost constant, even in the spectrum filtered with $30^\circ <$ DYE_ELV $< 40^\circ$ according to the fact that this line is emitted from the LHB and MWH, which we will described in the next section. For the solar component, we have to choose a proper threshold of the elevation angle for a given observation, particularly in a spectral analysis of the low energy band ($\lesssim$1 keV).

In addition, it is noted that the XIS sometimes detects the emission lines created by the charge exchange between neutral atoms in the earth's magnetosheath and heavy ions in the solar wind (Fujimoto et al. 2007). It is difficult to eliminate these lines by filtering with the elevation angles. However, by referring to the solar wind data, i.e., solar proton and X-ray flux, the evaluation of this component is possible.

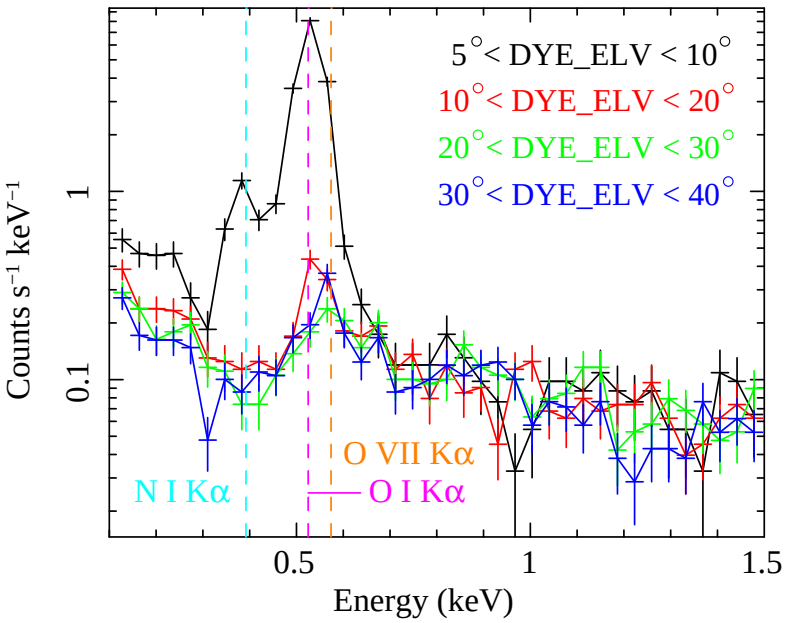

Figure 5.1: DYE_ELV dependence on the background spectrum. These are raw spectra, from which the NXB has not been subtracted, of the XIS1 obtained from the observation of the NEP field. The dashed lines of cyan, magenta, and orange show the line center energies of Ni I Kα (392 eV), O I Kα (525 eV), and O VII Kα (574 eV), respectively.

5.2 Sky X-ray background

The sky X-ray background is always detected when the Suzaku XRT is directed toward the sky. Therefore, we have to subtract this background from the observed spectrum to obtain the source spectrum. When a point source is analyzed, the sky X-ray background can be estimated from the source free region in the same FOV. However, when the target is diffuse emission over the XIS FOV, we have to estimate the sky X-ray background from the observations of other fields by Suzaku.

The sky X-ray background could be divided into three components: the LHB, MWH, and CXB. The LHB is the hot gas surrounding the solar system with a $\sim$100 pc scale; and hence, it has no galactic absorption. In contrast, the MWH is the hot gas surrounding the Milky Way; and hence, it has galactic absorption. Since typical temperatures are approximately 0.1 keV for the LHB and 0.2–0.3 keV for the MWH, the LHB and MWH are dominant in the low energy band ($\lesssim$1 keV). These components of a given sky direction can be estimated from the ROSAT All-Sky Survey diffuse background maps (Snowden et al. 1998) by using the "X-ray background tool"[1]. However, since the spectral resolution of the ROSAT PSPC is much lower than that of the XIS, the results obtained with the

[1]http://heasarc.gsfc.nasa.gov/cgi-bin/Tools/xraybg/xraybg.pl

X-ray background tool should not be perfect. Therefore, the LHB and MWH are two components that must be studied using the Suzaku XIS.

A significant part of the CXB is known to be a collection of faint unresolved extragalactic sources (Hasinger et al. 2001; Giacconi et al. 2001). It can be reproduced by a power-law component whose photon index is ∼1.4 and is dominant in the high energy band ($\gtrsim$1 keV). The CXB is not completely uniform over the sky reflecting the distribution of the sources. Lumb et al. (2002) have reported that its deviation from field to field of the 2–10 keV flux is ∼3.5% using the XMM-Newton EPIC. Hereafter, we refer to the deviation as spatial fluctuation. On the other hand, Kushino et al. (2002) have reported that the spatial fluctuation of the 2–10 keV flux is 6.49% using the ASCA GIS. Thus, the spatial fluctuation differs in each instrument due to the differences in the effective area and the point spread function (PSF). In order to consider the spatial fluctuation in the XIS, we analyze blank sky fields where there are no bright sources.

5.2.1 Vignetting and contamination

Since the sky X-ray background is focused by the XRT, it is affected by the vignetting of the XRT, as shown in Fig. 5.2. The intensity of the sky X-ray background decreases as the radius increases. The intensity at the annular region of 8–9 arcmin is ∼65% of that of the center region in the 1–5 keV band. The sky X-ray background is also affected by the contamination on the XIS optical blocking filters (OBFs) (Koyama et al. 2007a), particularly in the energy band of $\lesssim$1 keV. The thickness of the contamination varies with position on the OBF and increases with time. In the spectral analysis, the effects of contamination for each observation can be estimated by using the ancillary response file, ARF, calculated by *xissimarfgen* in FTOOLS (Ishisaki et al. 2007).

5.2.2 Data screening

We selected 6 blank sky observations with Suzaku whose net exposure times are longer than 40 ks. These observations are listed in table 5.1. These data are rev1.2 products (Mitsuda et al. 2007) whose XIS modes are normal 5×5 or 3×3 modes (without burst or window options). We screen these data with the following criteria:

1. Events generated by the particles and in the bad columns are excluded. We select events whose ASCA grades are 0, 2, 3, 4, and 6. Almost all particle events can be excluded by this grade selection.

2. X-ray events are extracted for the ELV greater than 5° and the DYE_ELV greater

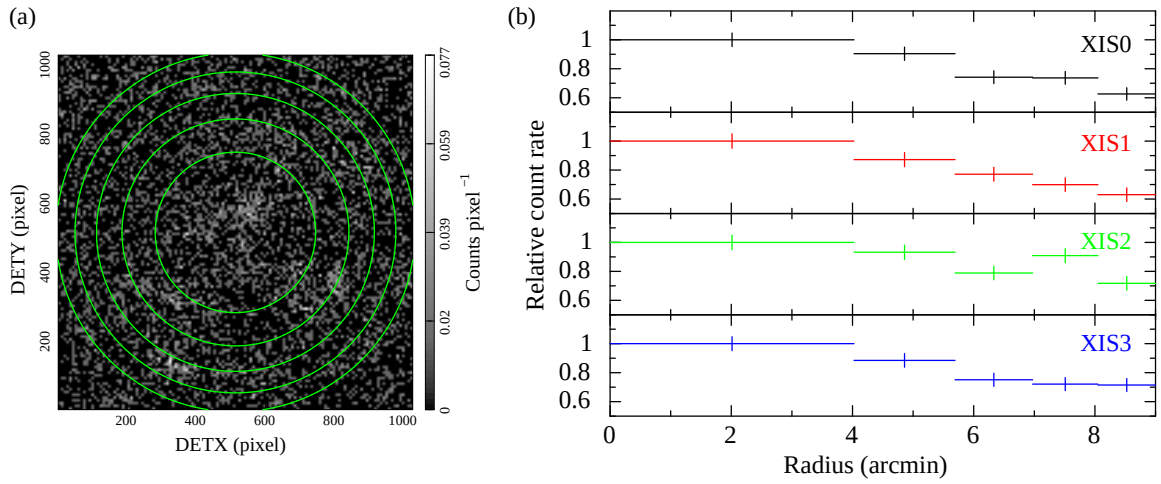

Figure 5.2: XRT vignetting effect for the XIS. (a) Blank sky image of the XIS0, from which the NXB model has been subtracted, with the detector (DET) coordinate. DETX/Y shows the axes of X/Y with the DET coordinate. (b) Radial profile of the blank sky background. The annular region of each bin is represented by the green circles in (a). The image and profile are obtained from the observation of the north ecliptic pole (NEP) shown in table 5.1. Their energy bands are 1–5 keV.

than 20°. Additionally, we filter the events with the condition of T_SAA_HXD > 436 s.

3. The *cleansis* command in FTOOLS is applied with the default parameters to exclude the flickering pixels.

4. The events during telemetry saturation are excluded by using the *xisgtigen* command in FTOOLS.

5. The orbit filter is applied.

Steps 1–3 are the default criteria for the "cleaned event files," which are accessible via the Suzaku web page[2].

5.2.3 Point source elimination

Since the CXB depends on the threshold for point source elimination, S_0, as shown in eqs. (5.11) and (5.12), we determine the threshold in this subsection. First, we search the point sources (hereafter referred to as "point source candidates") from the XIS image of each blank sky observation by visual inspection and extract their spectra. The point

[2]http://darts.isas.jaxa.jp/astro/suzaku/

Table 5.1: Blank sky observations

Field ID	Field name	Date*	Exposure† (ks)	Aim point (l, b)	N_H‡ (10^{20} cm^{-2})
1	North ecliptic pole	2006/02/10	85.9	(95.°77, 28.°67)	4.5
2	A2218 offset A	2005/10/01	42.5	(97.°74, 40.°12)	2.9
3	High latitude A	2006/02/14	70.2	(68.°40, 44.°40)	1.0
4	Lockman hole A	2005/11/14	72.6	(149.°00, 53.°15)	0.56
5	Lockman hole B	2006/05/17	75.7	(149.°68, 53.°19)	0.56
6	High latitude B	2006/02/17	92.1	(272.°43, −58.°27)	3.4

* Date when the observation was started.

† Net exposure time performed the orbit filter.

‡ Galactic hydrogen column density toward to the observed field estimated by Kalberla et al. (2005).

source candidates are indicated in Fig. 5.3 by red and blue circles. Their background spectra, which contain both the NXB and sky X-ray background, are estimated from the source free regions in the same FOV. Then, we fit the spectra with an absorbed power-law model. All the parameters for the model — hydrogen column density, photon index, and normalization for the power-law model — are free in the fit.

Figure 5.4 shows the histogram of fluxes (0.7–8 keV energy band) for the point source candidates. Although the number of point sources should continuously increase as their fluxes decrease, the number of point source candidates detected by us decreases at the flux lower than 2.5×10^{-14} erg cm^{-2} s^{-1}. Therefore, we assume that this flux indicates the sensitivity limit for the point source detection in our sample of the blank sky observations. The point source candidate whose flux is greater than 2.5×10^{-14} erg cm^{-2} s^{-1} is recognized as a point source.

5.2.4 Spectral analysis

The spatial fluctuation of the CXB depends on the effective beam size of the region where a spectrum is extracted (eq. 5.12). In the analysis of galaxy clusters (chapter 6), we will divide the XIS FOV into several regions. Therefore, to correctly evaluate the CXB fluctuation in the cluster analysis, we analyze the sky X-ray background by dividing the FOV of each blank sky observation into three parts. We note that the CXB fluctuation has not yet been considered in most of the previous studies of clusters. The effective beam

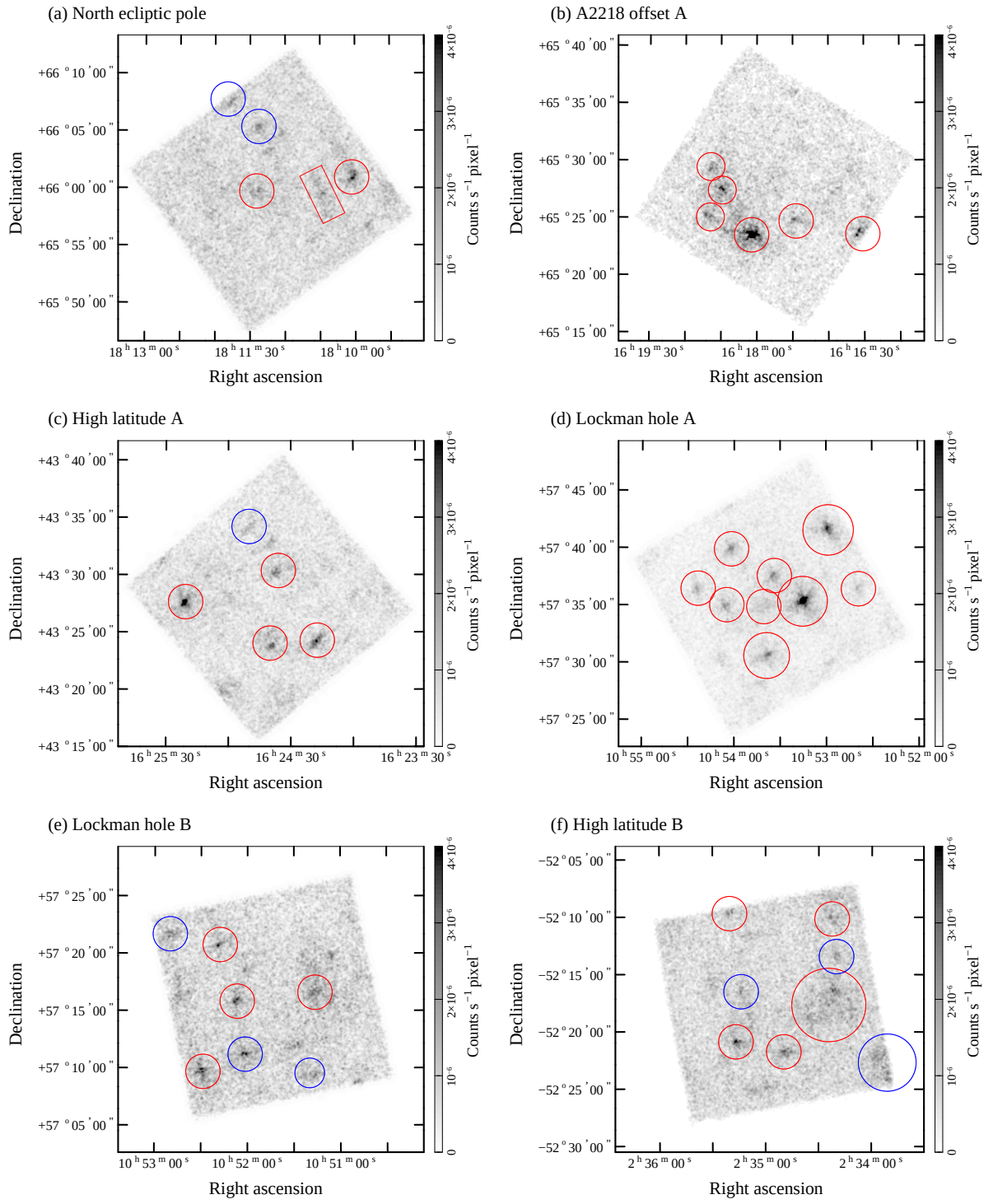

Figure 5.3: X-ray images of the 0.4–5 keV energy band in 6 blank sky fields. The data from the four XISs are merged. The NXB component are not subtracted from these images. The source candidates of the flux (0.7–8 keV energy range) greater than 2.5×10^{-14} erg cm^{-2} s^{-1} are marked with red circles, while those of the flux lower than 2.5×10^{-14} erg cm^{-2} s^{-1} are marked with blue circles.

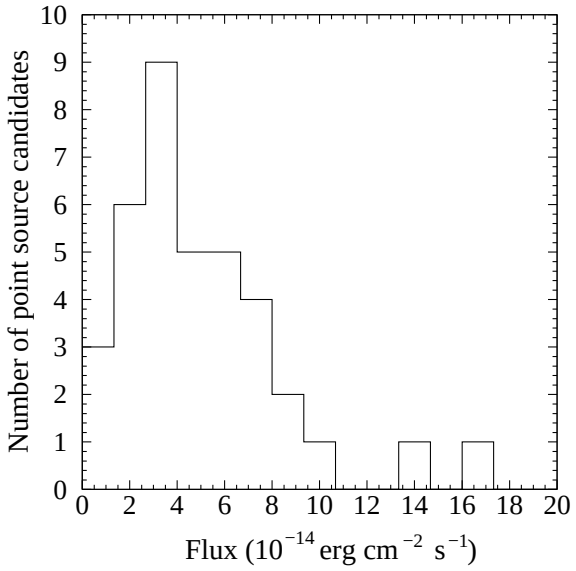

Figure 5.4: Histogram of fluxes of point source candidates. Energy range of the fluxes is the 0.7–8 keV.

size of the 1/3 region of the FOV is approximately consistent with that of the regions for the cluster analysis within a factor of 0.5–2. We divide the FOV with the DET coordinate (DETX, DETY), as shown in Fig. 5.5(a), and call the three 1/3 regions as DET-1, DET-2, and DET-3. The DETX ranges of DET-1, DET-2, and DET-3 are $0 < \mathrm{DETX} \leq 340$, $340 < \mathrm{DETX} \leq 680$, and $680 < \mathrm{DETX} \leq 1024$ (pixel), respectively. We extract the spectrum for each DET region excluding the point sources indicated by the red circles in Fig. 5.3, whose fluxes are greater than 2.5×10^{-14} erg cm^{-2} s^{-1}. The vignetting does not affect this spectral analysis because we use the ARF generated by assuming a uniform-sky emission. Details about the ARF are described below.

We generate the NXB spectrum modeled with the PIN-UD for each blank sky spectrum by using the method described in subsection 4.2.1 and subtract it from the blank sky spectrum. We simultaneously fit the FI and BI spectra of the three DET regions with two thermal models (APECs) for the LHB and MWH and a power-law model for the CXB in XSPEC (version 12). The CXB and MWH components are absorbed by galactic absorption (WABS) characterized by the galactic hydrogen column density N_H shown in table 5.1. The abundance and redshift for the LHB and MWH are set to 1 and 0, respectively. The other parameters are free in the fit, while the temperatures for the LHB and MWH and the photon index for the CXB are set to the same values for each DET region. The normalizations of the FI and BI sensors are allowed to take different values.

In the fit, we use the RMF calculated for the epoch of the blank sky observation by using the *xisrmfgen* command (version 2006-11-26) in FTOOLS and the ARF generated by using the *xissimarfgen* command (version 2006-11-26) in FTOOLS. The ARF are generated assuming the uniform-sky emission from the circular region with a radius of 20′ to consider a fraction of the photons which come from outside of the sky direction corresponding to the extraction region of the spectra. In addition, the effects of the contamination on the OBF are considered in the ARF.

Figure 5.6 shows the spectra and the best-fit model for the DET-2 region of the high latitude A observation. We use the 0.4–10 keV and 0.25–8 keV energy bands for the FI and the BI spectra, respectively. The energy band of 1.82–1.845 keV is ignored for both. As shown in this figure, the blank sky spectra are well modeled with two thermal models and a power-law model.

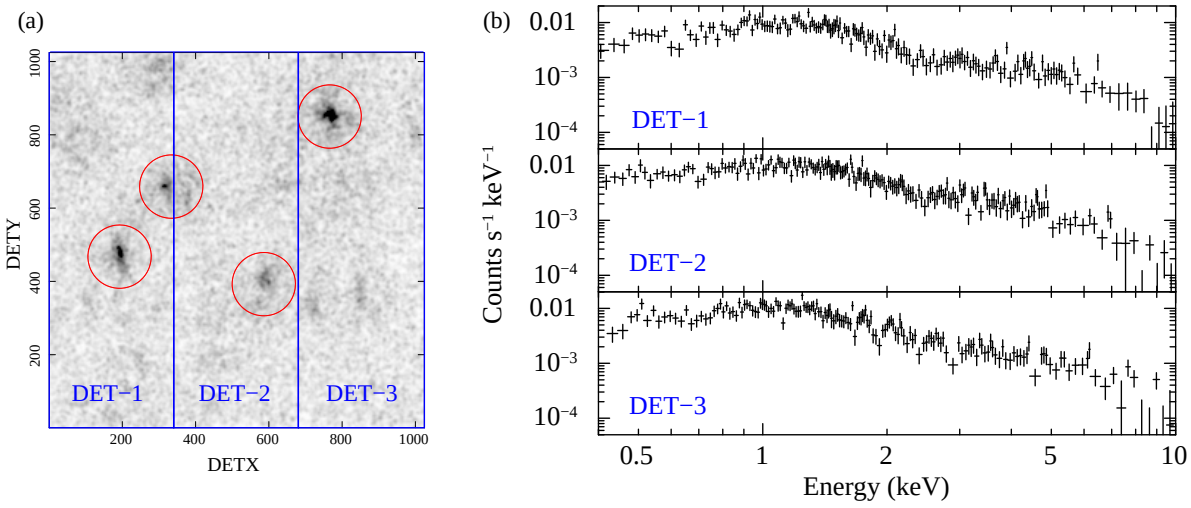

Figure 5.5: (a) X-ray image of the high latitude A field in the 0.4–5 keV energy band. This is the same image as that in Fig. 5.3(c). (b) FI spectra of the high latitude A field where the NXB models were subtracted. Each spectrum was extracted from the region marked with the blue box in (a) from which the regions marked with the red circles were excluded.

5.2.5 Results

Here, we describe the results of the spectral analysis. Figure 5.7 shows the best-fit parameters of the blank sky observations. Additionally, Figs. 5.8(a) and (b) show the fluxes in the low energy band (0.4–1 keV) and the high energy band (2–10 keV), respectively. The fluxes in the low and high energy bands mainly indicate those of the sum of the LHB and

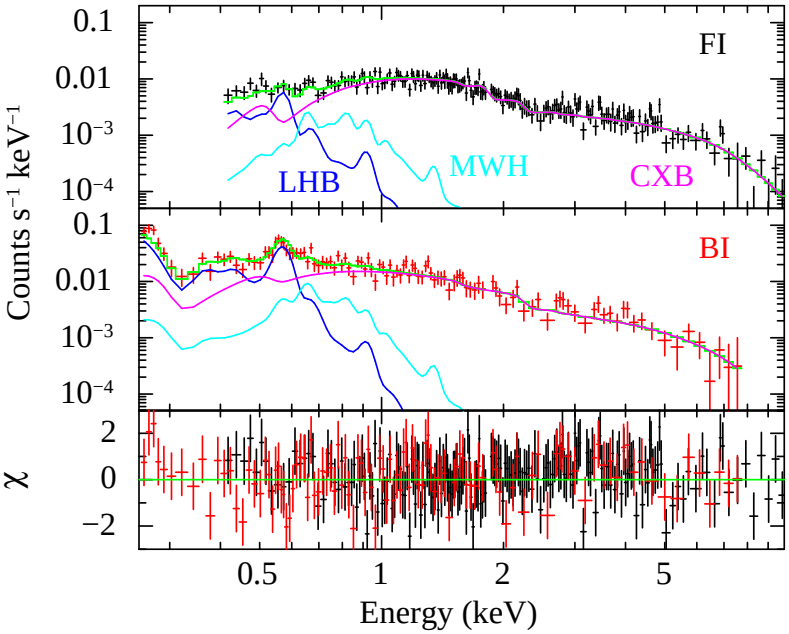

Figure 5.6: XIS spectra in the DET-2 region of the high latitude A field, best-fit models, and residuals. Blue, cyan, and magenta lines show the LHB, MWH, and CXB, respectively. Green lines show the model for the sum of the LHB, MWH, and CXB.

MWH, and CXB, respectively.

First, we calculate the spatial fluctuations of the best-fit parameters by using a method similar to that of Kushino et al. (2002). Since each parameter has individual statistical errors of fitting, we calculate the weighted average $\mathrm{P_A}(y)$ and its 1σ error $\delta\mathrm{P_A}(y)$ for a parameter y as

$$\mathrm{P_A}(y) = \sum_{i=1}^{6} \frac{y_i}{\sigma_i^2} \Big/ \sum_{i=1}^{6} \frac{1}{\sigma_i^2} \ , \tag{5.1}$$

$$\delta\mathrm{P_A}(y) = \left(\frac{1}{6-1} \sum_{i=1}^{6} \frac{[y_i - \mathrm{P_A}(y)]^2}{\sigma_i^2} \Big/ \sum_{i=1}^{6} \frac{1}{\sigma_i^2} \right)^{1/2} \ , \tag{5.2}$$

where i denotes the field ID of the blank sky observations (table 5.1), and y_i and σ_i denote the best-fit value and its 1σ error, respectively. The intrinsic variance $\mathrm{P_{Sd}}^2(y)$ and its 1σ error $\delta\mathrm{P_{Sd}}^2(y)$, obtained after subtracting the statistical error, are computed as

$$\mathrm{P_{Sd}}^2(y) = \left(\sum_{i=1}^{6} \frac{[y_i - \mathrm{P_A}(y)]^2}{\sigma_i^2} \Big/ \sum_{i=1}^{6} \frac{1}{\sigma_i^2} \right) - \left(6 \Big/ \sum_{i=1}^{6} \frac{1}{\sigma_i^2} \right) \ , \tag{5.3}$$

$$\delta\mathrm{P_{Sd}}^2(y) = \sqrt{\frac{2}{6-1}} \sum_{i=1}^{6} \frac{[y_i - \mathrm{P_A}(y)]^2}{\sigma_i^2} \Big/ \sum_{i=1}^{6} \frac{1}{\sigma_i^2} \ . \tag{5.4}$$

Equations (5.1)–(5.4) are correct when the intrinsic distribution of y and the distribution of the statistical error of y_i have Gaussian shapes. However, we cannot confirm their distributions because we have used a small number of blank sky fields. Therefore, assuming that the distributions have a Gaussian shape, we calculate $\mathrm{P_A}(y)$, $\delta\mathrm{P_A}(y)$, $\mathrm{P_{Sd}}(y)$, and $\delta\mathrm{P_{Sd}}(y)$ and summarize from in table 5.2.

Next, we calculate the averages and spatial fluctuations of the fluxes by using a method similar to that used for obtaining the best-fit parameters, as described above. An average, $\mathrm{F_A}(f)$, and its 1σ error, $\delta\mathrm{F_A}(f)$, for flux in a energy range e are calculated as follows:

$$\mathrm{F_A}(e) = \sum_{i=1}^{6}\sum_{j=1}^{3}\frac{f_{ij}}{\sigma_{ij}^2}\Big/\sum_{i=1}^{6}\sum_{j=1}^{3}\frac{1}{\sigma_{ij}^2}\ , \tag{5.5}$$

$$\delta\mathrm{F_A}(e) = \left(\frac{1}{6\times 3-1}\sum_{i=1}^{6}\sum_{j=1}^{3}\frac{[f_{ij}-\mathrm{F_A}(e)]^2}{\sigma_{ij}^2}\Big/\sum_{i=1}^{6}\sum_{j=1}^{3}\frac{1}{\sigma_{ij}^2}\right)^{1/2}\ , \tag{5.6}$$

where j denotes the DET region number, i.e., DET-j, and f_{ij} and σ_{ij} denote the values of the flux and its 1σ error, respectively. The intrinsic variance $\mathrm{F_{Sd}}^2(e)$ and its 1σ error $\delta\mathrm{F_{Sd}}^2(e)$, obtained after subtracting the statistical error, are computed as

$$\mathrm{F_{Sd}}^2(e) = \left(\sum_{i=1}^{6}\sum_{j=1}^{3}\frac{[f_{ij}-\mathrm{F_A}(e)]^2}{\sigma_{ij}^2}\Big/\sum_{i=1}^{6}\sum_{j=1}^{3}\frac{1}{\sigma_{ij}^2}\right) - \left(6\times 3\Big/\sum_{i=1}^{6}\sum_{j=1}^{3}\frac{1}{\sigma_{ij}^2}\right)\ , \tag{5.7}$$

$$\delta\mathrm{F_{Sd}}^2(e) = \sqrt{\frac{2}{6\times 3-1}}\sum_{i=1}^{6}\sum_{j=1}^{3}\frac{[f_{ij}-\mathrm{F_A}(e)]^2}{\sigma_{ij}^2}\Big/\sum_{i=1}^{6}\sum_{j=1}^{3}\frac{1}{\sigma_{ij}^2}\ . \tag{5.8}$$

The values of the fluxes in the 0.4–1 keV band and 2–10 keV band are summarized in table 5.2. Although the errors in these fluctuations are large, an increase in the number of blank sky fields will reduce the errors further.

5.2.6 CXB

We have measured the CXB spectrum and its spatial fluctuation using the Suzaku observations. However, since we have used only 6 blank sky fields, we compare the observed CXB fluctuation with that expected from the analytical method.

The origin of the CXB is mostly considered to be the extra galactic point sources, and its distribution reflects a beam-to-beam fluctuation of X-ray sources in the observed field. First, we assume a certain $\log N - \log S$ relation that defines the intensity distribution of X-ray sources in the sky. The differential form of the flux (S) vs. number (n) relation is expressed using a normalization k and a slope γ as

$$n(S) = -\frac{dN(>S)}{dS} = \begin{cases} 0 & (S < S_{\min})\ , \\ kS^{-\gamma} & (S_{\min} < S)\ , \end{cases} \tag{5.9}$$

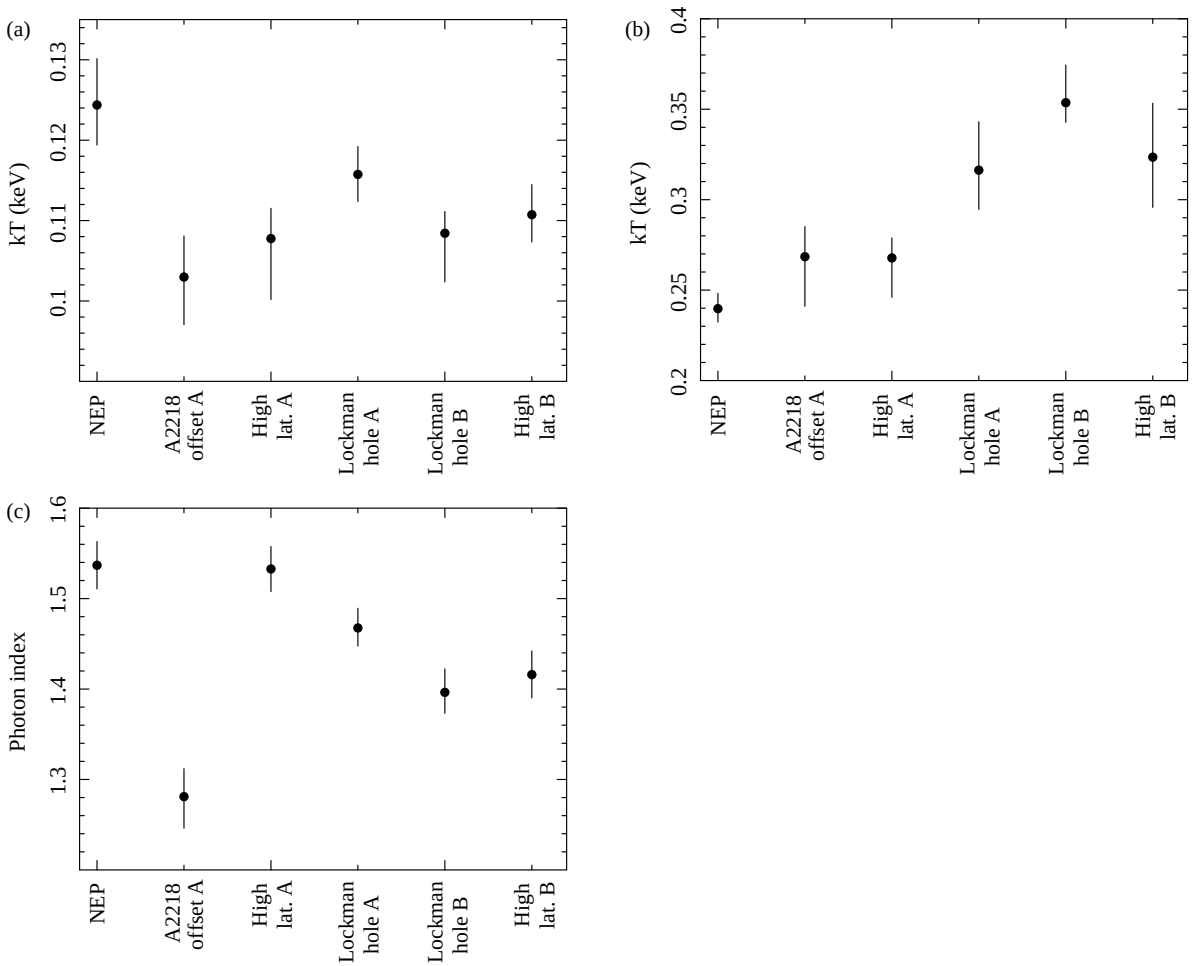

Figure 5.7: Best-fit parameters of temperatures of the (a) LHW, (b) MWH, and (c) photon index of the power-law component. Errors are 1σ confidence level.

Table 5.2: Averages and spatial fluctuations of the best-fit values and the fluxes of the blank sky analysis

Parameter	Average P_A	Fluctuation P_{Sd}* (%)
LHB kT	0.1121 ± 0.0026 keV	3.4 ± 2.5
MWH kT	0.270 ± 0.019 keV	14.5 ± 5.2
$\Gamma^\dagger$	1.451 ± 0.034	5.0 ± 1.8
Energy band	Average F_A	Fluctuation F_{Sd}* (%)
0.4–1 keV	$(1.695 \pm 0.083) \times 10^{-15\ddagger}$	18.4 ± 3.8
2–10 keV	$(4.37 \pm 0.14) \times 10^{-15\ddagger}$	12.0 ± 2.4

Errors are 1σ confidence level.

* This value is normalized by its average, F_A.

† Photon index of a power-law component.

‡ Unit of this value is erg cm^{-2} s^{-1} arcmin^{-2}.

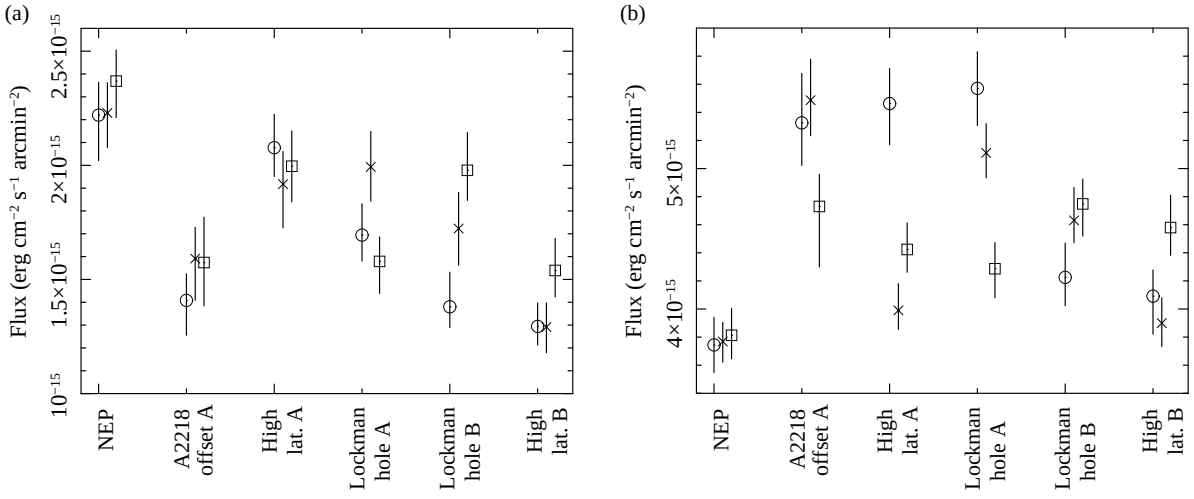

Figure 5.8: Fluxes in the (a) 0.4–1 keV band and (b) 2–10 keV band. Open circles, crosses, and open boxes show the fluxes of DET-1, DET-2, and DET-3 regions, respectively. Errors are 1σ confidence level.

where the notation $N(>S)$ signifies the number density of sources brighter than S per steradian. The γ value equals 2.5 in the Euclidean Universe, which is a good approximation. Then, the integrated form is given as

$$N(>S) = \begin{cases} \dfrac{k}{\gamma-1} S_{\rm min}^{-\gamma+1} & (S < S_{\rm min}) \ , \\ \dfrac{k}{\gamma-1} S^{-\gamma+1} & (S_{\rm min} < S) \ . \end{cases} \tag{5.10}$$

The CXB flux in the flux range of $S < S_0$ is calculated as

$$F(S_0) = \int_{S_{\rm min}}^{S_0} n(S) S \, dS = \frac{k}{\gamma-2} \left(S_{\rm min}^{-\gamma+2} - S_0^{-\gamma+2} \right) \ . \tag{5.11}$$

We adopt $k = 1.58 \times 10^{-15}$ and $\gamma = 2.5$ as reported by Kushino et al. (2002).

In this blank sky analysis, since we exclude the point sources whose fluxes are greater than 2.5×10^{-14} erg cm^{-2} s^{-1} in the 0.7–8 keV band, we adopt the corresponding 2–10 keV flux of 2.0×10^{-14} erg cm^{-2} s^{-1} as S_0 in eq. (5.11). Thus, the value of $S_{\rm min}$ is obtained as 1.75×10^{-15} erg cm^{-2} s^{-1} (2–10 keV), using $F(S_0) = 5.31 \times 10^{-8}$ erg cm^{-2} s^{-1} sr^{-1} (2–10 keV) determined from the observations (subsection 5.2.5).

According to Condon (1974), the CXB fluctuation width, $\sigma_{\rm F}$, is given analytically as

$$\sigma_{\rm F} = \frac{{\rm F_{Sd}}}{{\rm F_A}} = \frac{\gamma-2}{S_{\rm min}^{-\gamma+2} - S_0^{-\gamma+2}} \sqrt{\frac{S_0^{3-\gamma} - S_{\rm min}^{3-\gamma}}{(3-\gamma) k \Omega_{\rm eff}}} \ , \tag{5.12}$$

where $\Omega_{\rm eff}$ represents the effective beam size of the XRT + XIS system. Since we have divided the XIS FOV into three regions and excluded the point sources, $\Omega_{\rm eff}$ is 78.66 arcmin^2 $= 6.656 \times 10^{-6}$ sr on average. Using the $\Omega_{\rm eff}$ and $S_{\rm min}$ values mentioned above, $\sigma_{\rm F}$ is calculated as 13.3% from eq. (5.12). This value is consistent with the observed spatial fluctuation of the 2–10 keV flux, $12.0 \pm 2.4\%$ (table 5.2).

5.2.7 LHB and MWH

Our results indicate that the mean temperatures of the LHB and MWH are 0.11 keV and 0.27 keV, respectively. Using the ROSAT PSPC, Kuntz & Snowden (2000) have reported that the temperatures are $0.118^{+0.038}_{-0.023}$ keV and $0.250^{+0.079}_{-0.045}$ keV for the LHB and MWH, respectively. In addition, using the XMM-Newton EPIC, Lumb et al. (2002) reported the temperatures are $0.099^{+0.054}_{-0.037}$ keV and $0.24^{+0.08}_{-0.03}$ keV for the LHB and MWH, respectively. These values are consistent with our results within the errors.

We have also measured the spatial fluctuations of the flux in the 0.4–1 keV band, where the LHB and MWH are dominant, and the temperatures for the LHB and MWH. As shown

in table 5.2, while the fluctuation of the temperature for the LHB is small, the fluctuations of the flux and the MWH temperature are relatively large. The large fluctuation of the low energy flux is also reported by previous observations (Kushino et al. 2002; Lumb et al. 2002). Therefore, in the spectral analysis of clusters, the temperatures and the normalizations for the LHB and MWH must be evaluated for each cluster to correctly subtract these components. If many pointing observations around the target cluster are available, they may be very useful to estimate the LHB and MWH components. In our case, however, since there are only a few pointing observations, we fit the cluster spectrum simultaneously with the ICM component and the sky X-ray background component, where the temperatures and normalizations of the LHB and MWH will be free in the fit. The details will be described in subsection 6.2.5.

5.2.8 Uncertainties in background subtraction

First, we demonstrate the extent to which the uncertainty of the source intensity depends on the NXB reproducibility and CXB fluctuation. We assume an extended source over the XIS FOV whose flux is comparable to that of the CXB. We also assume an exposure time of 100 ks, which is typical for this type of extended source, and an effective beam size of 78.66 arcmin^2. Such an observation typically spans over two days, corresponding to an NTE exposure of 5 ks in our database. We concentrate on the energy band of 5–12 keV of the XIS-FIs. We find the count rate of the NXB, I_{NXB}, to be 1.38×10^{-2} cts s^{-1} and the reproducibility, ΔI_{NXB}, to be 4.8×10^{-4} cts s^{-1} (3.5% of I_{NXB}) based on table 4.5(c). The average photon index for the CXB is 1.451, and the average CXB flux is 5.31×10^{-8} erg cm^{-2} s^{-1} sr^{-1}, as reported in this chapter. We also estimate the spatial fluctuation of the CXB flux to be 12.0% (1σ). Employing these values, we evaluate the expected count rate of the CXB for the XIS-FIs, I_{CXB}, to be 2.32×10^{-3} cts s^{-1} and the CXB fluctuation in the effective beam size of 78.66 arcmin^2, ΔI_{CXB}, to be 2.8×10^{-4} cts s^{-1}. We should note that ΔI_{CXB} is slightly less than or comparable to ΔI_{NXB} in our case.

When we obtain the count rate of the raw data, I_{raw}, we will subtract the NXB and CXB from it in order to evaluate the source count rate, I_{src}. Since we assume I_{src} to be comparable to I_{CXB}, I_{raw} is $(1.38 + 0.232 + 0.232) \times 10^{-2} = 1.84 \times 10^{-2}$ cts s^{-1} and its statistical error, ΔI_{raw}, is 4.29×10^{-4} cts s^{-1}. We will obtain I_{src} by subtracting $(I_{CXB} + I_{NXB})$ from I_{raw}. We can calculate the error of I_{src}, ΔI_{src}, to be $\sqrt{\Delta I_{NXB}^2 + \Delta I_{CXB}^2 + \Delta I_{raw}^2} = 7.0 \times 10^{-3}$ cts s^{-1}. ΔI_{NXB} and ΔI_{CXB} contribute almost equally to ΔI_{src}, while the contribution of the statistical error ΔI_{raw} is less than these two. Similarly, we evaluate the NXB reproducibility and the CXB fluctuation of the

XIS-FIs in the 1–7 keV energy band by using the same method as that employed for the 5–12 keV band. The calculations show that $\Delta I_{NXB} = 0.048 I_{NXB} = 4.6 \times 10^{-4}$ cts s^{-1}, $\Delta I_{CXB} = 0.12 I_{CXB} = 1.6 \times 10^{-3}$ cts s^{-1}, and $\Delta I_{src} = 1.8 \times 10^{-3}$ cts s^{-1}, where $I_{NXB} = 9.64 \times 10^{-3}$ cts s^{-1} and $I_{CXB} = 1.37 \times 10^{-2}$ cts s^{-1}. We should note that I_{NXB} does not change significantly, while I_{CXB} in the 1–7 keV band in 6 times larger than that in the 5–12 keV band. Therefore, ΔI_{src} is mainly determined by ΔI_{CXB}, rather than by ΔI_{NXB}.

Next, we evaluate an exposure time T for the diffuse source whose flux is comparable to that of the CXB, $I_{src} = 1.37 \times 10^{-2}$ cts s^{-1}, in the 1–7 keV band. In this case, ΔI_{src} is expressed as

$$\Delta I_{src}^2 = \Delta I_{raw}^2 + \Delta I_{NXB}^2 + \Delta I_{CXB}^2 \tag{5.13}$$

$$= \frac{I_{src} + I_{NXB} + I_{CXB}}{T} + \Delta I_{NXB}^2 + \Delta I_{CXB}^2 \ . \tag{5.14}$$

We calculate the exposure time T that ΔI_{raw}^2 is by a factor of 5 lower than the sum of ΔI_{NXB}^2 and ΔI_{CXB}^2, as follows:

$$T = \frac{5\ (I_{src} + I_{NXB} + I_{CXB})}{\Delta I_{NXB}^2 + \Delta I_{CXB}^2} = 67\,\mathrm{k}s \ . \tag{5.15}$$

This indicates that for the source of I_{src}, the exposure time of 67 ks is required to maximize the advantage of the low NXB level of the XIS. Such an evaluation also implies that diffuse and extremely faint sources cannot be accurately observed using the XIS, even with sufficiently long exposure times, because ΔI_{NXB} and ΔI_{CXB} do not depend on T. Thus, when the observations of diffuse sources are planned, the NXB reproducibility and the CXB fluctuation should be considered. It should be noted that the exposure time required by the analysis of emission lines, e.g., measurement of metal abundances, is longer than that required by the analysis of continuum components, e.g., measurement of temperature.

Chapter 6

Temperature Profiles of Regular Clusters

The temperature and density are important measurable characteristics to study the physical properties of the diffuse cosmic baryons in the ICM. Under the action of gravity, these baryons follows the dark matter during the process of hierarchical structure formation, in which they are heated by adiabatic compression during the halo mass growth and by shocks induced by supersonic accretion or merger events. Under the assumptions that provided gravity dominates the process of gas heating, and gas is in hydrostatic equilibrium within the dark matter, scaling relations for cluster properties, e.g., temperature and density, are predicted because gravity is a scale-free force. These scaling relations has been also predicted by hydrodynamical simulations of galaxy clusters in the CDM model (e.g. Navarro et al. 1995; Evrard et al. 1996; Loken et al. 2002; Borgani et al. 2004). In addition, if the density and temperature profiles of the ICM have the scaling relations, the global temperature of ICM, excluding the core region, should be a good proxy for the total gravitating mass.

In order to investigate the scaling relations for cluster properties, it is important to perform the temperature and density measurements up to the outermost region of clusters. However, these measurements are difficult at large cluster radii because the X-ray surface brightness of a cluster decreases rapidly as the distance from the cluster center increases, e.g. eq. (2.26). In particular, for the determination of temperature from an observed spectrum, sufficient photon statistics are required to fit the spectrum. Moreover, the observed spectrum is contaminated with cosmic, solar, and instrumental backgrounds. Consequently, at large cluster radii, accurate temperature and density measurements become challenging tasks.

ASCA was the first satellite with the spectro-imaging capability required for such

studies. Using ASCA data, Markevitch et al. (1998) obtained the temperature profiles for a sample of 30 nearby clusters, which showed significant declines with radius between $r = 0.1r_{180}$ and $r = 0.6r_{180}$. BeppoSAX was another satellite capable of spatially resolved spectroscopy with a better spatial resolution. De Grandi & Molendi (2002) analyzed 21 clusters and found declining temperature profiles, in good agreement with Markevitch et al. (1998), outside the cores [$r > (0.15–0.2)r_{180}$]. However, ASCA and BeppoSAX data are complicated by the mirror effects such as the energy dependence of the point-spread function (PSF) and sometimes stray light. The radial temperature profiles of clusters are sensitive to these effects. As a result, at the end of the ASCA/BeppoSAX era, the exact shape of cluster temperature profile was still under vigorous debate (Irwin et al. 1999; White 2000; Irwin & Bregman 2000; Finoguenov et al. 2001a).

Analyses with Chandra and XMM-Newton do not suffer from the above mentioned PSF problems since they have a much better PSF than ASCA and BeppoSAX. Recent observations of Vikhlinin et al. (2005) and Pratt et al. (2007) have largely validated the original ASCA results of Markevitch et al. (1998), which suggested that temperature profiles decline from the centers of clusters to their outer regions. However, these measurements have been limited up to $0.5–0.6r_{180}$ because of small effective areas or high/unstable background levels. In addition, some observations with Chandra and XMM-Newton (Allen et al. 2001; Arnaud et al. 2001; Kaastra et al. 2004b) have found flatter profiles. Therefore, it is important to determine the ICM temperature in the outermost region ($r \sim r_{180}$) of clusters in order to know their properties.

Suzaku XIS has large effective area and relatively low and much stable background level, and the stray light of the Suzaku XRT is more suppressed than that of the ASCA XRT. The XIS is thus suited for the temperature measurements in the outermost regions of clusters. In this chapter, we measure the temperature and surface brightness, which is proportional to the squared gas density, profiles for a sample of 8 regular clusters observed using Suzaku in order to investigate the scaling relations for cluster properties and therefore the heating mechanisms of ICM.

We assume $h = 0.71$, $\Omega_m = 0.3$, and $\Omega_\Lambda = 0.7$. We use the solar metal abundances reported by Anders & Grevesse (1989). Measurement uncertainties in this chapter correspond to 1σ confidence level, unless otherwise specified.

6.1 Sample clusters

We selected 20 Suzaku observations of 8 sample clusters where outer regions were observed using the XIS and whose overall X-ray morphology is regular. These clusters and their

Suzaku observations are listed in tables 6.1 and 6.2, respectively. In this chapter, we mainly discuss the radial temperature profiles of the ICM using these observations of the sample clusters, while the details about the radial metallicity profiles will be discussed in the next chapter.

We will normalize the radial temperature of a cluster and calculate its virial radius from a global gas temperature, T_X, which should be representative of the cluster's virial temperature. However, because of the limited angular resolution of the Suzaku XRT and the small FOV of the XIS, the XIS is not suited for the measurement of the global temperature. Therefore, we mainly utilize the global temperatures measured using other satellites, as shown in table 6.1.

Table 6.1: Cluster sample

ID	Cluster	$N_H{}^*$ (10^{20} cm^{-2})	z	$D_A{}^\dagger$ (Mpc)	$T_X{}^\ddagger$ (keV)
1	A1060	4.94	0.0114	47.5	3.20[§]
2	A1413	2.19	0.1430	510.8	7.3[‖]
3	A1795	1.19	0.0620	234.0	6.1[‖]
4	A2052	2.71	0.0356	144.0	2.96[§]
5	A2218	3.24	0.1756	605.0	6.97[§]
6	A2801	1.79	0.1080	401.4	2.53[§]
7	A2804	1.71	0.1080	401.4	1.28[#]
8	A2811	1.60	0.1080	401.4	5.17[§]

* Galactic hydrogen column density toward the observed field estimated from Kalberla et al. (2005).

† Angular distance at redshift z.

‡ Measured global temperature.

§ Horner et al. (2000)

‖ Vikhlinin et al. (2005)

This work (see subsection 6.3.7)

6.2 Analysis method

6.2.1 Procedure of spectral analysis

Here, we outline the procedure used for the spectral analysis of each cluster.

Table 6.2: Cluster observations

Observation		Sequence number	Pointing direction (l, b)	Date*	Exposure† (ks)
A1060	center	800003010	(269.°60, 26.°49)	2005/11/22	23.9
	offset	800004010	(269.°88, 26.°65)	2005/11/20	30.2
A1413		800001010	(225.°21, 76.°86)	2005/11/15	88.5
A1795	center	800012010	(33.°81, 77.°19)	2005/12/10	10.9
	near north	800012020	(34.°71, 77.°20)	2005/12/10	22.9
	near south	800012040	(32.°91, 77.°16)	2005/12/11	26.0
	far north	800012030	(35.°61, 77.°22)	2005/12/11	27.7
	far south	800012050	(32.°02, 77.°14)	2005/12/12	39.3
A2052	south east	100006010	(9.°31, 49.°96)	2005/08/20	13.4
	north east	100006020	(9.°65, 50.°06)	2005/08/20	20.8
	north west	100006030	(9.°50, 50.°27)	2005/08/21	12.3
	south west	100006040	(9.°17, 50.°18)	2005/08/21	13.4
A2218	center-1	100030010	(97.°72, 38.°12)	2005/10/01	40.3
	center-2	800019010	(97.°73, 38.°12)	2005/10/26	29.1
	offset-A	100030020	(97.°74, 40.°12)	2005/10/02	42.5
	offset-B	800020010	(96.°38, 38.°09)	2005/10/27	14.9
A2801		800008010	(357.°12, −86.°54)	2005/11/27	24.3
A2804		800007010	(357.°93, −86.°83)	2005/12/02	23.9
A2811	center	800005010	(358.°34, −87.°45)	2005/11/28	23.2
	offset	800006010	(358.°19, −87.°14)	2005/11/28	25.4

* Date when the observation was started.

† Net exposure time performed the orbit filter.

1. The observation data are screened by using the same method as that used for the blank sky analysis described in subsection 5.2.2.

2. The spectra are extracted from the annular regions centered on the cluster.

3. For each annular region, the NXB model spectrum is created using PIN-UD by employing the method described in subsection 4.2.1. These NXB spectra are subtracted from the observed cluster spectra extracted in step 2.

4. The RMF for the epoch of the cluster observation is generated by using the *xisrmfgen* command (version 2006-11-26).

5. The surface brightness profile is created.

6. Two types of ARFs are generated by using the *xissimarfgen* command (versions 2006-11-26 or 2007-07-16).[1]

7. The most probable values of the CXB model parameters, photon index and normalization parameter, are determined for the cluster.

8. The spectra are fitted with the ICM and the sky X-ray background components. To take account of the CXB fluctuation, we apply three normalizations for the CXB in the fit: (i) the most probable value, (ii) +12% of that value, and (iii) −12% of that value.

Details about steps 5, 6, 7, and 8 will be described in subsections 6.2.2, 6.2.3, 6.2.4, and 6.2.5, respectively.

6.2.2 Surface brightness profile

An observed image contains (a) emission from the ICM, (b) the sky X-ray background, i.e., LHB, MWH, and CXB, and (c) the NXB. The NXB image can be estimated using the same method as that used for creating the NXB spectrum (see subsection 4.2.1) and subtracted from the observed image. Here, the X-ray surface brightness profile in the 1–5 keV is created because the LHB and MWH are almost negligible. In order to obtain the surface brightness of the ICM, we further need to subtract the CXB component from the NXB-subtracted surface brightness and correct for the vignetting effect.

We estimate the CXB component by using the *xissim* (version 2006-11-26) command in FTOOLS in the following manner: (1) Assuming the uniform sky, 10^8 counts of incident

[1]The differences between these versions have no effect on the results of spectral analysis.

photons are generated by the *mkphlist* (version 2006-11-26) command in FTOOLS. The spectrum of the photons has a shape of an absorbed power-law with the photon index of 1.451 and the normalization of 9.07×10^{-4} photons keV^{-1} cm^{-2} s^{-1} at 1 keV. These values are consistent with the observed values shown in table 5.2. The absorption is estimated from the neutral hydrogen column density N_H for each cluster (table 6.1). (2) Simulated event file is generated by using the *xissim* command. (3) Simulated CXB image is created from the event file generated in step (2) by using the *xselect* task.

The photon distribution of the CXB over the CCD chip can be estimated in this manner. This distribution also represents the vignetting effect. To correct for the vignetting effect, we normalize the ICM surface brightness, from which the NXB and the simulated CXB are subtracted, by the count rate of the simulated CXB in the circular region of $4'$ radius from the center of the CCD chip.

6.2.3 ARF

An observed spectrum contains the following components: (a) emission from the ICM, (b) the sky X-ray background, and (c) the NXB. (c) can be subtracted by using the NXB model. The spectra of LHB and MWH contained in (b) are well reproduced by two thermal models, and the CXB spectrum has the shape of an absorbed power-law. However, we cannot fit the observed spectrum directly by the sum of (a) and (b) because their spatial distributions are different in the sky (Ishisaki et al. 2007).

Therefore, we create two types of ARFs by using the *xissimarfgen* command. One type of ARF is calculated by assuming the uniform-sky emission from a circular region with a radius of $20'$. The radius of $20'$ is selected to take into account a fraction of the photons that originate outside of the sky direction corresponding to the extraction region of the spectra. This is the same type of ARF that we employed in the analysis of the sky X-ray background (section 5.2). Hereafter, we call it as uniform ARF. The other type of ARF is calculated assuming the surface brightness from the ICM as given by a model such as β-model or double β-model. The β-model is expressed by eq. (2.26), and the double β-model is the sum of two β-models. When there is a large excess emission from the β-model in a cluster center, we apply the double β-model. The model parameters are mainly obtained by fitting the surface brightness obtained from the XIS. We generate the ICM image over the circular region with a radius of $20'$ centered on the direction of observation by the β-model or double β-model. Choosing this image and 5×10^5 photons as the *source_image* and *num_photon* parameters for *xissimarfgen*, respectively, we calculate the ARF. This ARF is hereafter referred to as β-ARF.

6.2.4 Spatial fluctuation of CXB

As discussed in section 5.2, CXB has spatial fluctuation. Therefore, we employ the following method to take account of the fluctuation in the spectral analysis.

First, we obtain the most probable values of the CXB model parameters, namely, the photon index, $\Gamma_{\rm CXB}$, and the normalization parameter, $N_{\rm CXB}$, for a power-law model, for each cluster. If there is a region where the ICM is not significantly detected in the FOV, we extract a spectrum from this region. This spectrum is fitted with a model of the sky X-ray background, APEC + WABS (APEC + POWERLAW) model, in XSPEC (version 12). In this fit, the neutral hydrogen column density N_H for WABS, which reproduces photo-electric absorption, is set equal to the value shown in table 6.1. The abundance and redshift of the two APECs are set to 1 and 0, respectively. The other parameters are free in the fit. The best-fit values of photon index and normalization are adopted as $\Gamma_{\rm CXB}$ and $N_{\rm CXB}$, respectively. On the other hand, if there is no region where the ICM component is not significantly detected, we use the average values obtained by the blank sky analysis (shown in table 5.2) as $\Gamma_{\rm CXB}$ and $N_{\rm CXB}$.

The average effective beam size of the annular regions used for cluster analysis corresponds to about 50%–200% of that used for the blank sky analysis, $\Omega_{\rm eff} = 78.66$ arcmin^2. Therefore, we estimate that the CXB fluctuation for each annular cluster region is 12%. The cluster spectra are first fitted with the CXB normalization parameter set equal to $N_{\rm CXB}$, as shown in step 8(i). Then, they are refitted with the CXB normalization set equal to $\pm$12% of $N_{\rm CXB}$ as described in steps 8(ii) and (iii). The photon index of the power law is always set equal to $\Gamma_{\rm CXB}$.

We calculate the errors in which the CXB fluctuation is taken into account, $E_{\rm sta+sys}$, as

$$E_{\rm sta+sys} = \sqrt{(P_{12\%} - P_0)^2 + E_{\rm sta}^2}\ , \tag{6.1}$$

where $P_{12\%}$ and P_0 are the best-fit values of the fits in steps 8(ii, iii) and (i), respectively, and $E_{\rm sta}$ is the statistical error of the fit in step 8(i). We note that this approach is conservative in terms of error estimation.

6.2.5 Spectral fitting

We fit the spectra from which the NXB model has been subtracted with a model consisting of the sky X-ray background and the thin thermal plasma emission from the ICM. We employ APEC + WABS (APEC + POWERLAW) model in XSPEC as the sky X-ray background. On the other hand, WABS $\times$ APEC model is employed as the ICM component. Note that the sky X-ray background and the ICM component are reproduced by

using the uniform ARF and the β-ARF, respectively, as described in subsection 6.2.3. The galactic hydrogen column density shown in table 6.1 is adopted as the WABS parameter for both the sky X-ray background and the ICM component and is maintained constant in the fit. The temperature, metal abundances, and the normalization parameter for the ICM component are free parameters, while the redshift is set equal to the value for each cluster shown in table 6.1. The metal abundances of all elements considered in the APEC model (C, N, O, Ne, Mg, Al, Si, S, Ar, Ca, Fe, and Ni) are given relative to the solar value. The values of these abundances are set equal each other in the fit. This value represents the metallicity of the ICM.

The model parameters for the CXB and its spatial fluctuation are estimated as described in the above subsection. We also take account of the spatial fluctuations of LHB and MWH as follows. As discussed in subsection 5.2.7, the spatial fluctuations of LHB and MWH are larger than that of the CXB; therefore, it is difficult to estimate the LHB and MWH components from the observations of other fields by Suzaku. Therefore, the temperatures and normalizations of two APECs for the LHB and MWH are set as free parameters in the fit (step 8). In addition, under the assumption that the LHB and MWH are constant in adjacent sky regions, their parameters for each sample cluster are linked for its all annular spectra. However, if the ICM flux in the low-energy range is much higher than that of the sum of the LHB and MWH, the LHB and MWH components cannot be correctly estimated. Therefore, we do not employ the spectra that contain the ICM emission greater than $\sim 2 \times 10^{-14}$ erg cm^{-2} s^{-1} arcmin^{-2} in the 0.4–1 keV band in the fit of the LHB and MWH components. This threshold corresponds to about ten times of the average flux of the LHB and MWH shown in table 5.2.

Since the angular resolution of the Suzaku XRT ($\sim 2'$ in half-power diameter) is not as good as those of Chandra ($\sim 0.5''$) and XMM-Newton ($\sim 15''$), a fraction of the photons may become significant that originates outside of the sky direction corresponding to the extraction region of the spectra on the XIS detector plane. The fraction is often called as "stray light." However, the energy dependence of the stray light is almost negligible within $\sim$5% for the Suzaku XRT/XIS system (Sato et al. 2007). The stray light and its energy dependence have been significantly improved for Suzaku as compared to ASCA. Therefore, the effects of the stray light would be limited to only smoothing the spatial variation of the ICM properties by the contamination of the spectra collected from adjacent regions. In particular, since the stray light in the cluster center is more than that in outer regions (Fig. 15h of Sato et al. 2007), our results for the cluster centers, where the temperature gradients are strong, should be treated with caution. In contrast, the effects of stray light would be negligibly small in outer regions.

6.3 Results for individual clusters

6.3.1 A1060

A1060 has no cD galaxy and no strong cooling core. This cluster was closely observed using other instruments, e.g. Chandra and XMM-Newton. Yamasaki et al. (2002) detected very compact X-ray emissions from the two elliptical galaxies in the A1060 center. Hayakawa et al. (2006) also detected a temperature drop of $\sim$30% from the center to $r \sim 13'$ with XMM-Newton. Therefore, we measure a much more outer region than the previous observations.

Suzaku carried out two pointing observations for A1060, the central region and $20'$ east offset region. Figure 6.1 shows the image obtained from the two observations. We extract spectra from seven annular regions of $0'$–$2'$, $2'$–$4'$, $4'$–$6'$, $6'$–$9'$, $9'$–$14'$, $14'$–$21'$, and $>21'$, centered on (RA, Dec) = ($10^{\rm h}36^{\rm m}43^{\rm s}.8$, $-27^\circ31'21''$), as shown by the blue lines in Fig. 6.1(a). Figure 6.1(b) shows the surface brightness profile obtained from the XIS. However, since the XMM EPIC has better angular resolution than the Suzaku XIS, we generate the β-ARF by using the double β-model reported by Sato et al. (2007). Since the ICM component is significantly detected from the 7 annular regions, we adopt the mean values obtained by the blank sky analysis (table 5.2) as $\Gamma_{\rm CXB}$ and $N_{\rm CXB}$ for A1060. Then, we fit the 7 spectra as described in subsection 6.2.5 and obtain the temperature and abundance profiles shown in Fig. 6.1. The red, green, and blue diamonds in Fig. 6.1 show the best-fit values and their error ranges obtained by fitting in steps 8(i), (ii), and (iii), respectively. In addition, black bars show the error ranges in which the CXB fluctuation is taken into account, $E_{\rm sta+sys}$ in eq. (6.1).

6.3.2 A1413

A1413 was also closely observed using other instruments. XMM-Newton did not find any evidence of a cooling core (Pratt & Arnaud 2002), while Chandra detected the evidence (Vikhlinin et al. 2005). This should be due to the better angular resolution of Chandra with respect to that of XMM-Newton. In addition, there is a cD galaxy in the A1413 center (Feldmeier et al. 2002).

Fig. 6.3(a) shows the image of the A1413 north region observed using the XIS. We extract spectra from four annular regions of $<7'$, $7'$–$10'$, $10'$–$15'$, and $>15'$, centered on (RA, Dec) = ($11^{\rm h}55^{\rm m}18^{\rm s}.6$, $+23^\circ24'31''$). These spectra are excluded the point sources shown by the red circles in Fig. 6.3(a). Figure 6.3(b) shows the surface brightness profile in the 1–5 keV band. Since the XIS did not observe the center of A1413, we use the the

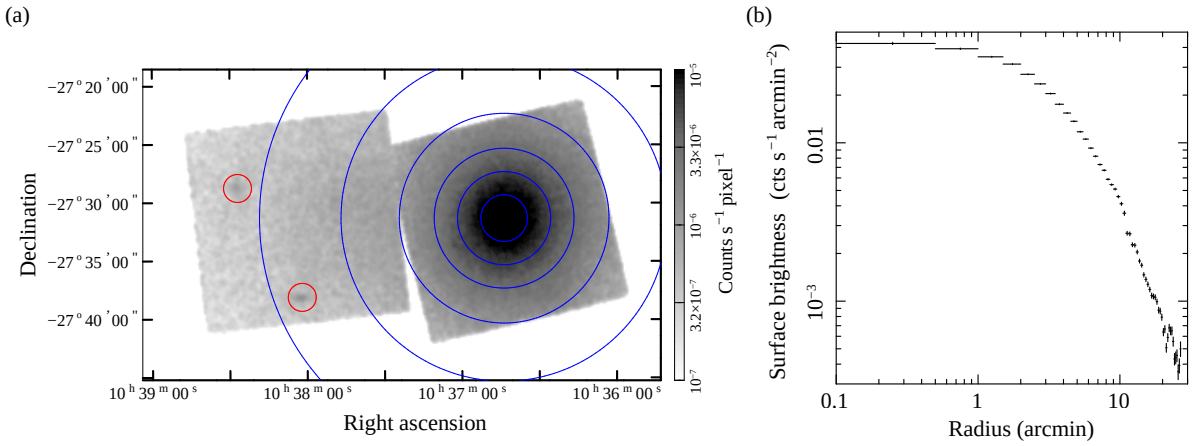

Figure 6.1: (a) A1060 X-ray image in the 0.4–5 keV energy band observed using the XIS. This image was obtained by averaging the four XISs, and the NXB and the vignetting effect were not corrected. The annular regions where the spectra were extracted are showed by the blue circles of the radii, $r = 2'$, $4'$, $6'$, $9'$, $14'$, and $21'$. The point sources showed by the red circles were excluded from the spectral analysis and the surface brightness profile. (b) Surface brightness profile in the 1–5 keV band. This profile was obtained by averaging the four XISs, and the NXB and the vignetting effects were corrected as described in subsection 6.2.2.

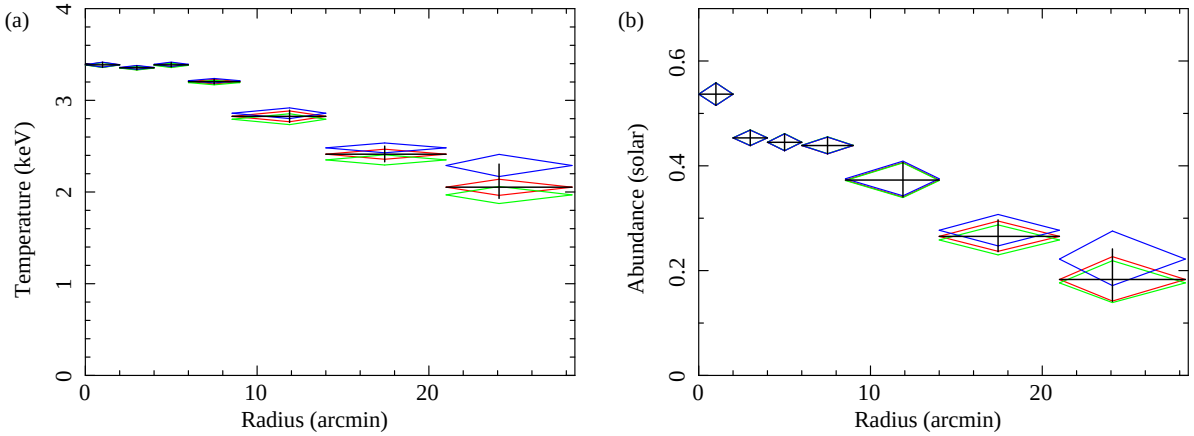

Figure 6.2: (a) Temperature and (b) metallicity profiles of A1060. The red, green, and blue diamonds show the best-fit values and $\pm 1\sigma$ error ranges of the fitting in steps 8(i), (ii), and (iii), respectively. The black bars denote the 1σ error ranges taking into account the CXB fluctuation of 12%. The metallicity in the $<7'$ radius was fixed to 0.5 solar, and hence is shown without the vertical error bars.

KBB model reported by Pratt & Arnaud (2002) to generate the β-ARF. Since the ICM component is not significantly detected in the outermost region (>15′), we determine $\Gamma_{\rm CXB}$ and $N_{\rm CXB}$ for A1413 by fitting the spectrum extracted from this region. These values are $\Gamma_{\rm CXB} = 1.489$ and $N_{\rm CXB} = 1.059 \times 10^3$ photons keV^{-1} cm^{-2} s^{-1} at 1 keV. Figure 6.4 shows the temperature and abundance profiles. Since the spectrum in the innermost region (<7′) is not excluded the calibration source regions to obtain good statistic, the 5.5–7 keV band of this spectrum is ignored in the spectral fit. Therefore, the metallicity of this region is set equal to $0.5 Z_{\odot}$. The errors of metallicities are relatively larger than those of the other clusters because the He-like Fe Kα line emitted from A1413 almost corresponds with the Mn Kα line emitted from the calibration sources due to the A1413 redshift of 0.143. Thus, our results of the A1413 metallicity should be treated with caution.

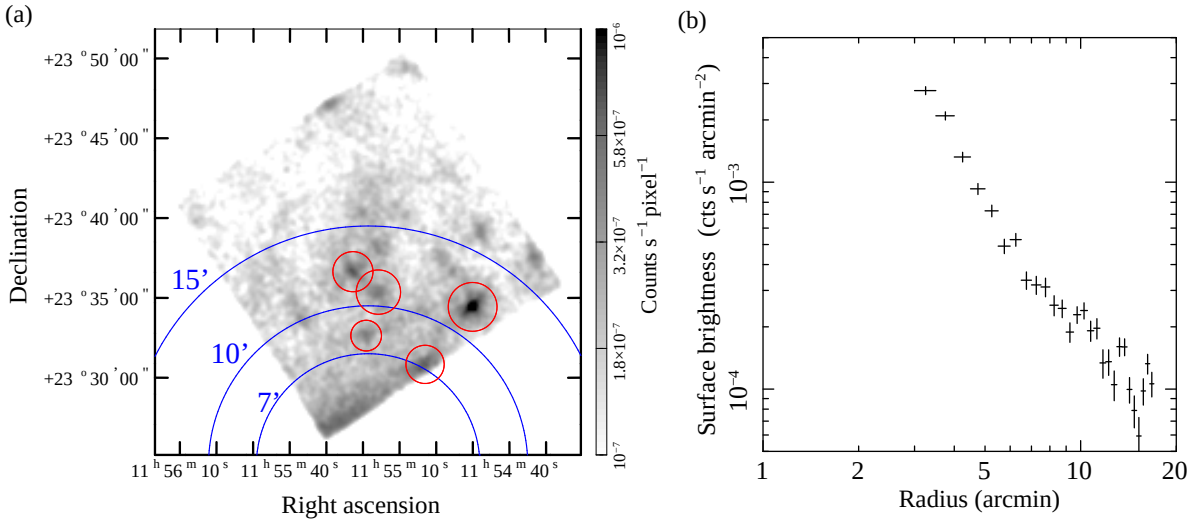

Figure 6.3: (a) A1413 X-ray image and (b) surface brightness profile.

6.3.3 A1795

A1795 has a strong cooling core and a cD galaxy. The previous observations with XMM-Newton (Nevalainen et al. 2005) and Chandra (Vikhlinin et al. 2005) obtained the temperature profiles from the center to ∼15′ and ∼17′, respectively.

A1795 was observed in five pointings, center, near north, near south, far north, and far south, as shown in Fig. 6.5(a). We extract spectra from seven annular regions of 0′–2′, 2′–4′, 4′–6′, 6′–9′, 9′–14′, 14′–19′, and >19′, centered on (RA, Dec) = ($13^{\rm h}48^{\rm m}50^{\rm s}.5$, +26°35′28″). The point sources shown by the red circles in Fig. 6.5(a) are excluded from these spectra. Figure 6.5(b) shows the surface brightness profile in the 1–5 keV band. Since the A1795 has a strong cooling core in the very center, and the XMM EPIC has

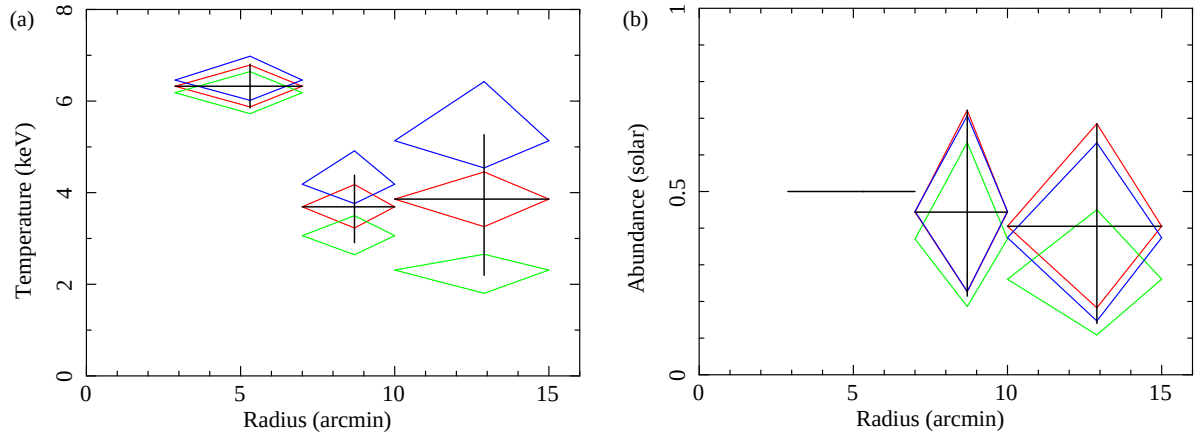

Figure 6.4: (a) Temperature and (b) metallicity profiles of A1413.

better angular resolution than the Suzaku XIS, we generate the β-ARF by using the double β-model obtained using the XMM-Newton EPIC (Ikebe et al. 2004). In the outermost region ($>19'$), since the ICM component is not significantly detected, we determine $\Gamma_{\rm CXB}$ and $N_{\rm CXB}$ for A1795 by fitting the spectrum extracted from this region. These values are $\Gamma_{\rm CXB} = 1.460$ and normalization of $N_{\rm CXB} = 9.950 \times 10^{-4}$ photons keV^{-1} cm^{-2} s^{-1} at 1 keV. Figure 6.6 shows the temperature and abundance profiles. In this spectral analysis, we do not employ the far north observation because there are extremely strong Al I Kα line and excess emission in the low energy band ($\lesssim$2 keV). Although the line and emissions would be due to the solar activity, we cannot subtract these from the spectrum by the NXB model. Since the ICM is almost not detected from the sky region of the far north observation, the effects by excluding this observation is not so significant.

6.3.4 A2052

A2052 has a strong cooling core and a cD galaxy, UGC 09799. Chandra observed the central region of A2052 and obtained its temperature profile up to $r \sim 6'$ (Blanton et al. 2003). Therefore, we measure a much more outer region than the Chandra observation.

A2052 was observed in four pointings, north east (NE), north west (NW), south east (SE), and south west (SW) as shown in Fig. 6.7. We extract spectra from seven annular regions of $0'$–$2'$, $2'$–$4'$, $4'$–$6'$, $6'$–$9'$, $9'$–$12'$, $12'$–$15'$, and $>15'$, centered on (RA, Dec) = ($15^{\rm h}16^{\rm m}44^{\rm s}.1$, $+07^\circ01'46''$). The point sources shown by the red circles in Fig. 6.7(a) are excluded from these spectra. Figure 6.7(b) shows the surface brightness profile and the best-fit double β-model, whose parameters are listed in table 6.3. Then, we generate the β-ARFs by using the double β-model. In the seven annular regions, since the ICM component is significantly detected, we adopt the mean values obtained by the blank sky

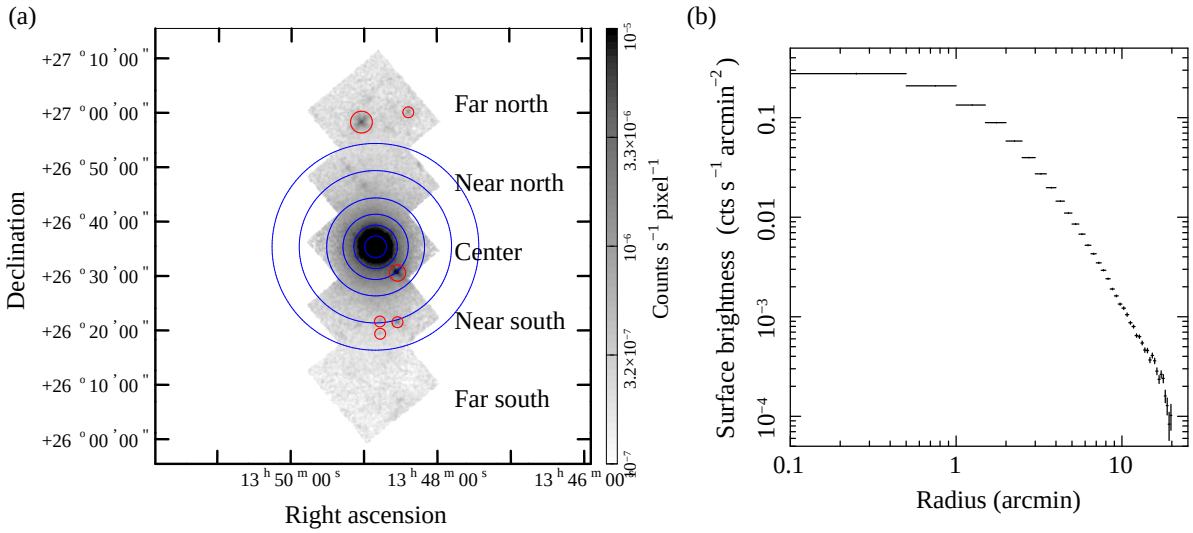

Figure 6.5: (a) A1795 X-ray image. The blue lines show the circular regions of the radii = 2′, 4′, 6′, 9′, 14′, and 19′. (b) Surface brightness profile.

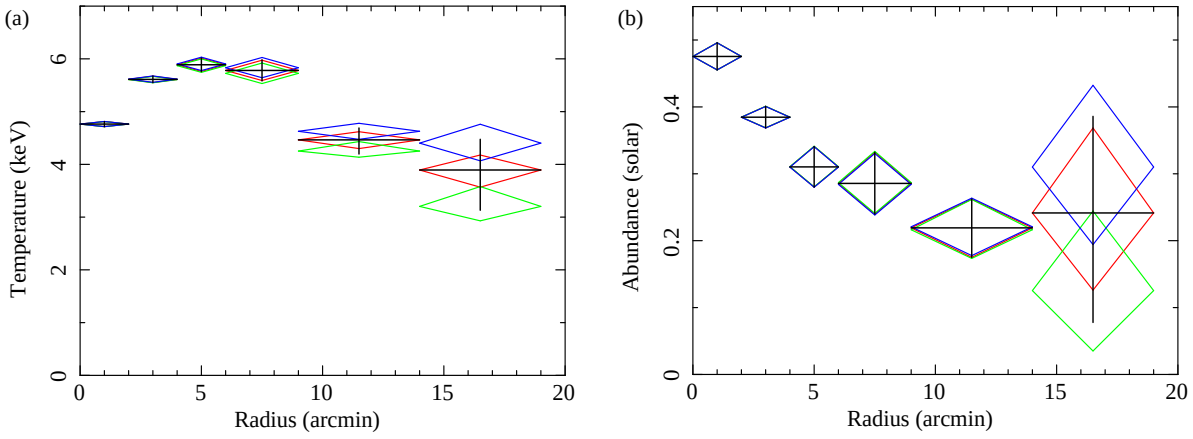

Figure 6.6: (a) Temperature and (b) metallicity profiles of A1795.

analysis (table 5.2) to $\Gamma_{\rm CXB}$ and $N_{\rm CXB}$. Figure 6.8 shows the temperature and abundance profiles.

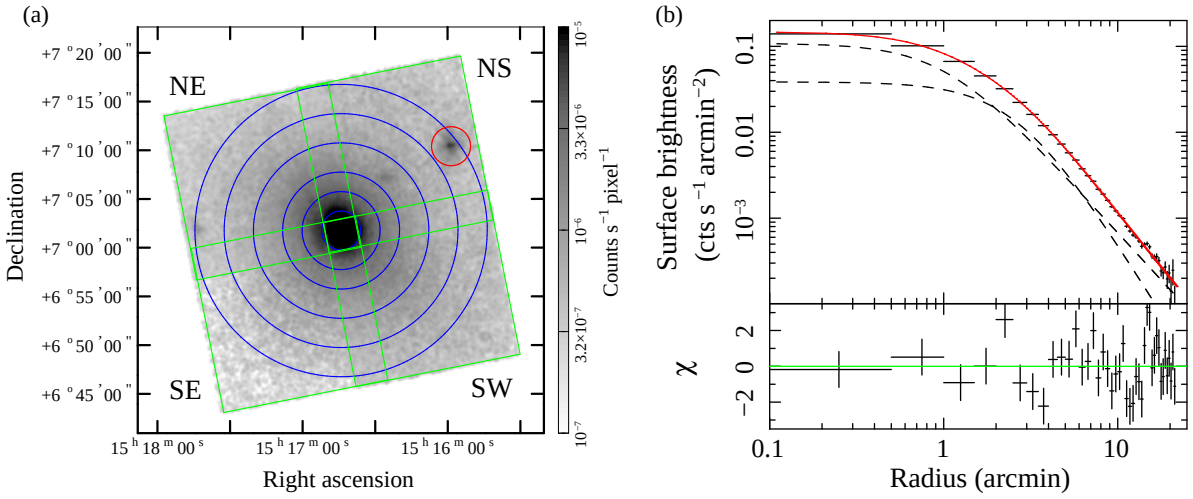

Figure 6.7: (a) A2052 X-ray image. The blue lines show the circular regions of the radii = 2′, 4′, 6′, 9′, 12′, and 15′. The green box shows the FOV of each observation. (b) Surface brightness profile. The red line shows the best-fit double β-model.

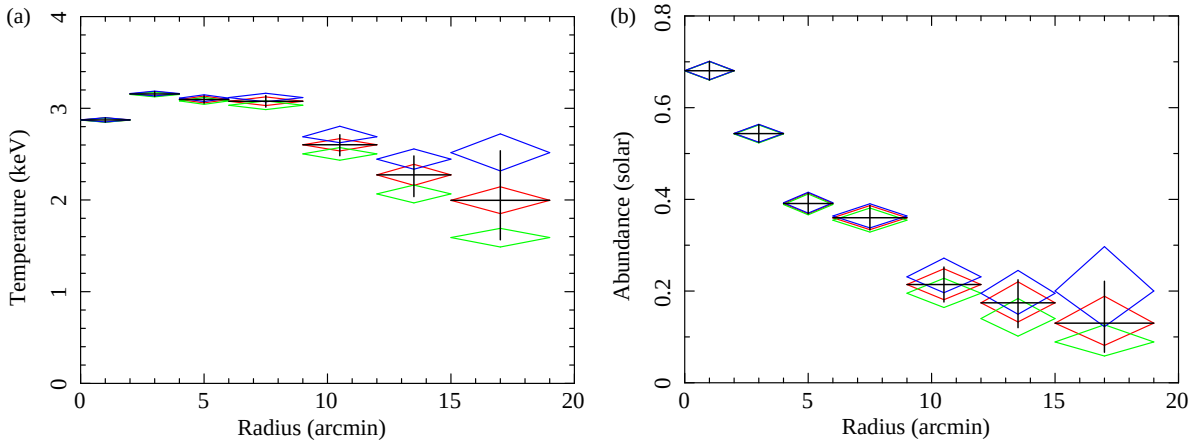

Figure 6.8: (a) Temperature and (b) metallicity profiles of A2052.

6.3.5 A2218

A2218 is a well-known cluster because of its strong gravitational lensing arcs. X-ray analysis suggests that the cluster core is not in hydrostatic equilibrium due to an ongoing or recent merger in the line-of-sight direction (Machacek et al. 2002; Pratt et al. 2005).

In addition, there is no evidence of the cooling core (Pratt et al. 2005), but A2218 has a cD galaxy.

We carried out four observations for A2218: two on the cluster (center-1 and center-2) and two in offset regions (offset-A and offset-B). To measure the sky X-ray background for A2218 analysis, the directions of the offset observations were sufficiently away from the A2218 center. Therefore, we obtain $\Gamma_{\rm CXB}$ and $N_{\rm CXB}$ values for A2218 by simultaneously fitting the spectra of offset-A and offset-B. The values are $\Gamma_{\rm CXB} = 1.383$ and $N_{\rm CXB} = 8.783 \times 10^{-4}$ photons keV^{-1} cm^{-2} s^{-1} at 1 keV. Figure 6.9(a) shows the A2218 X-ray image which the data of center-1 and center-2 observations have been merged. We extract spectra from five annular regions of 0′–2′, 2′–4′, 4′–6′, 6′–9′, and >9′, centered on (RA, Dec) = ($16^{\rm h}35^{\rm m}46^{\rm s}.8$, +66°13′09″). Fig. 6.9(b) shows the surface brightness profile obtained from the center-1 observation and its best-fit β-model. The best-fit parameters are summarized in table 6.3. We generate the β-ARFs by using the β-model. The results of the spectral analysis are shown in Fig. 6.10.

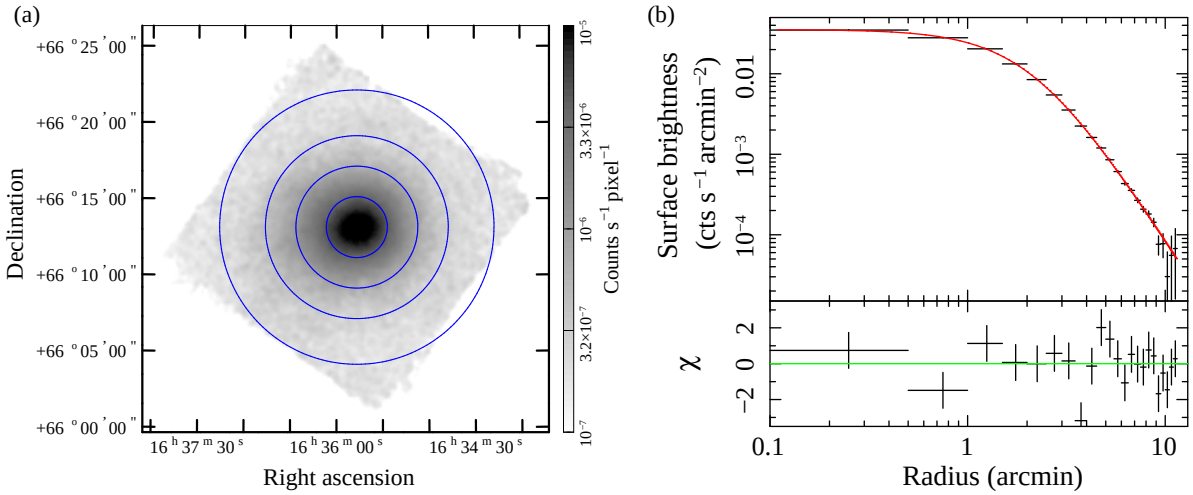

Figure 6.9: (a) A2218 X-ray image. The blue lines show the circular regions of the radii = 2′, 4′, 6′, and 9′. (b) Surface brightness profile.

6.3.6 A2801

Suzaku carried out four pointing observations for A2801, A2804, and A2811 which belong to the Sculptor supercluster. The Sculptor supercluster contains 25 clusters, which is one of the richest supercluster (Einasto et al. 2001). Since these clusters are adjacent each other as shown in Fig. 6.11, we adopt the same values of $\Gamma_{\rm CXB}$ and $N_{\rm CXB}$ to the spectral analysis of the clusters. Therefore, we extract the spectra from the four observations

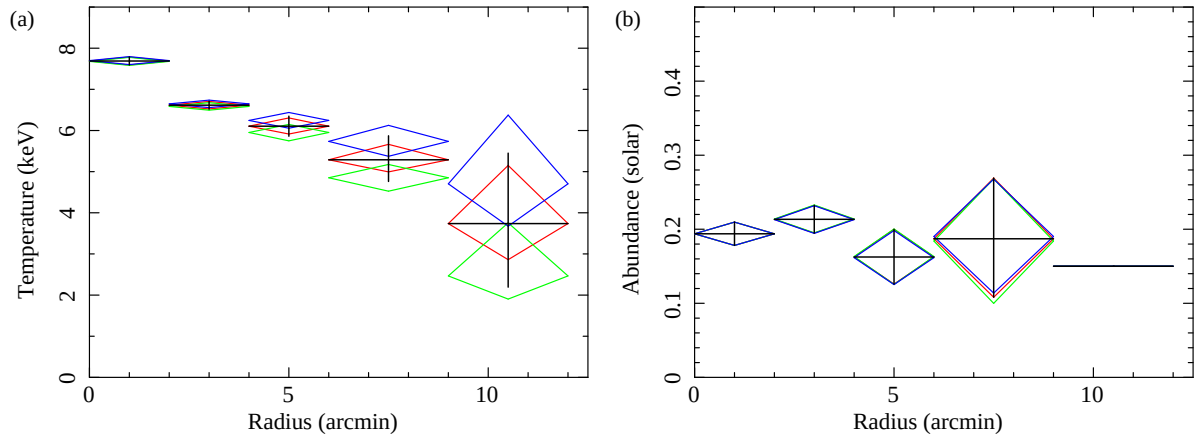

Figure 6.10: (a) Temperature and (b) metallicity profiles of A2218.

by excluding the red circle regions in Fig. 6.11, where the ICM or point source are significantly detected, and fit them with a model of the sky X-ray background. As the results, we obtain $\Gamma_{\rm CXB} = 1.413$ and $N_{\rm CXB} = 8.242 \times 10^{-4}$ photons keV^{-1} cm^{-2} s^{-1} at 1 keV.

The XIS image of A2801 is shown in Fig. 6.12(a). We extract spectra from four annular regions of 0′–2′, 2′–4′, 4′–6′, and 6′–9′, centered on (RA, Dec) = ($00^{\rm h}38^{\rm m}32^{\rm s}.5$, $-29°04'34''$). Fig. 6.12(b) shows the surface brightness profile. We fit the profile with a β-model and summarized the best-fit parameters in table 6.3. The β-ARF is generated by using the β-model. The results of the spectral analysis are shown in Fig. 6.13.

6.3.7 A2804

Suzaku carried out an observation for A2804. The XIS image is shown in Fig. 6.14(a). We extract spectra from five annular regions of 0′–2′, 2′–4′, and 4′–6′, centered on (RA, Dec) = ($00^{\rm h}39^{\rm m}40^{\rm s}.2$, $-28°54'21''$). We fit the surface brightness profile shown in Fig. 6.14(b) with a β-model and generate the β-ARF by using the model. As described in subsection 6.3.6, using $\Gamma_{\rm CXB} = 1.413$ and $N_{\rm CXB} = 8.242 \times 10^{-4}$ photons keV^{-1} cm^{-2} s^{-1} at 1 keV, we perform the spectral analysis. The temperature and abundance profiles are shown in Fig. 6.15.

The global temperature T_X of A2804 has not been measured yet. Therefore, we extract the spectrum from the circular region of $r = 4' \backsimeq 0.5 r_{180}$ and fit it. As the results, we obtain $kT = 1.28^{+0.30}_{-0.10}$ keV and utilize it as T_X.

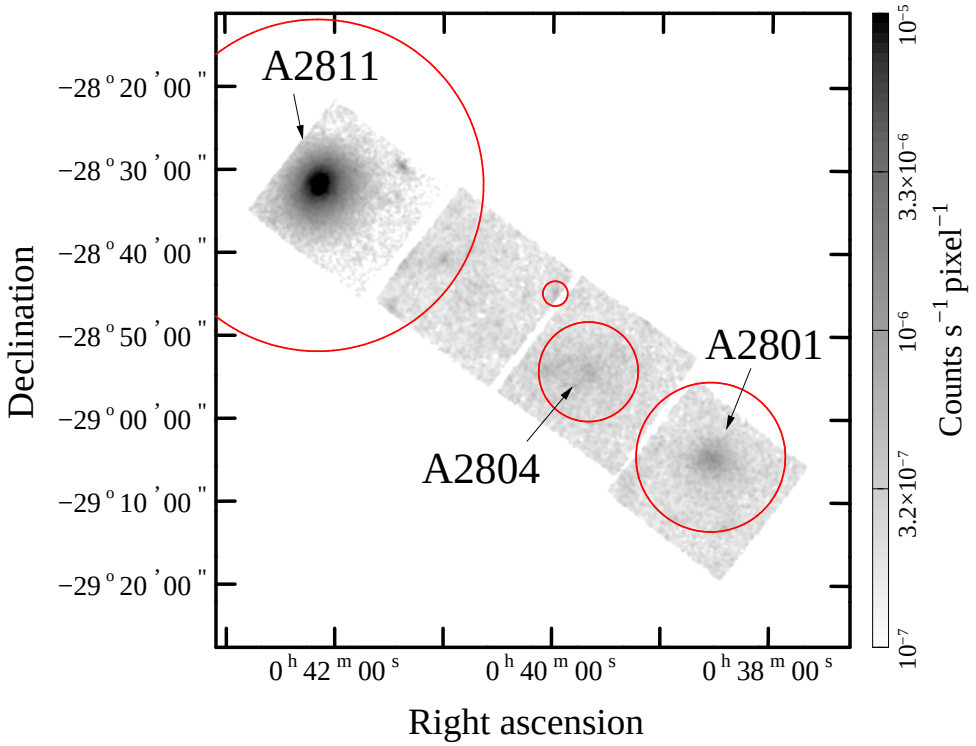

Figure 6.11: X-ray image of A2801, A2804, and A2811. The red circled regions were excluded from the analysis of the blank sky field in the Sculptor observations.

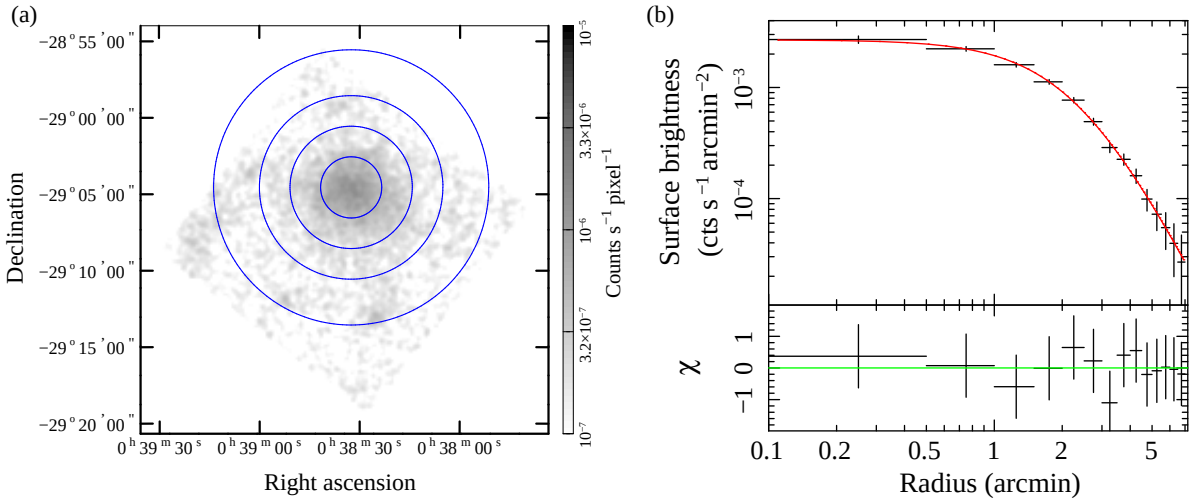

Figure 6.12: (a) A2801 X-ray image. The blue lines show the circular regions of the radii = 2′, 4′, 6′, and 9′. (b) Surface brightness profile.

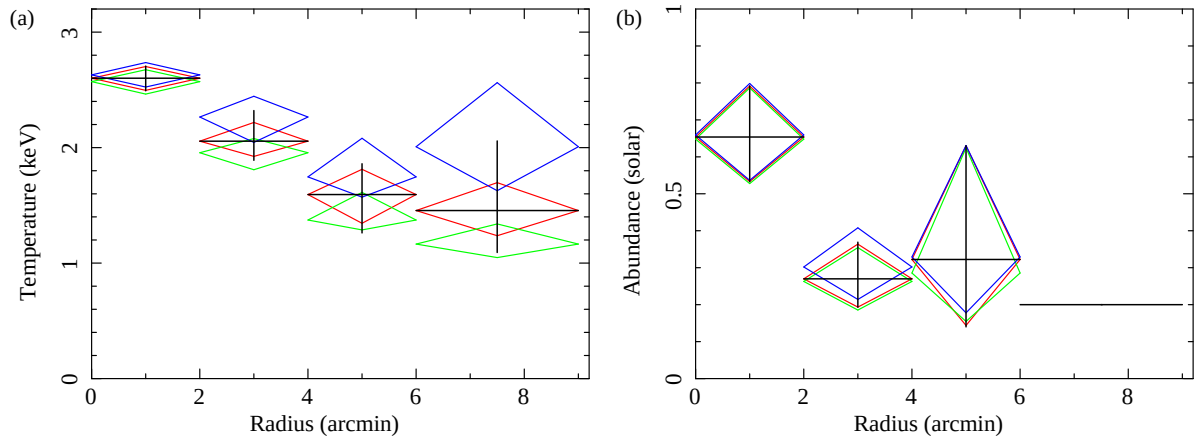

Figure 6.13: (a) Temperature and (b) metallicity profiles of A2801.

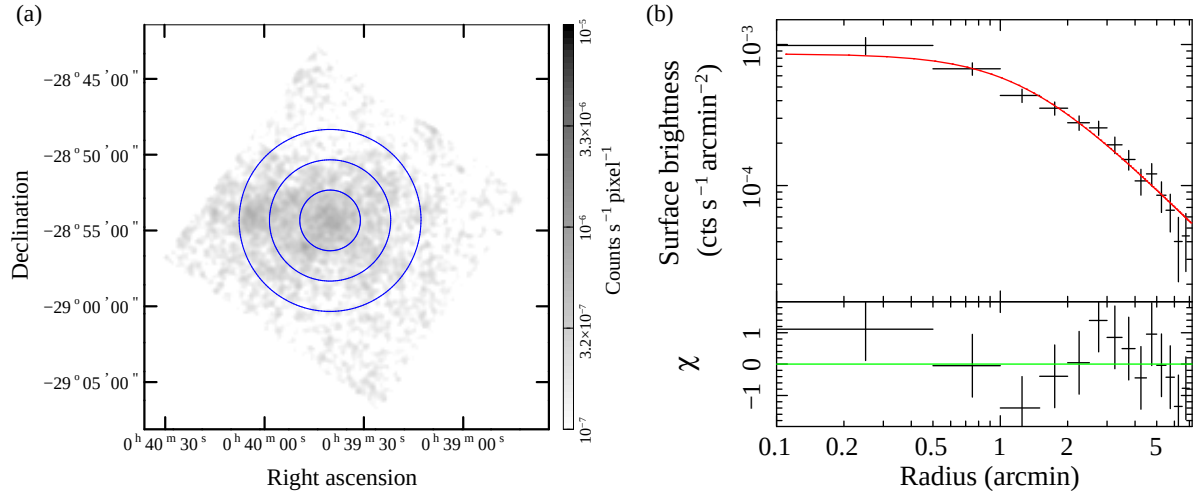

Figure 6.14: (a) A2804 image. Blue lines show the circular regions of the radii = 2′, 4′, and 6′. (b) Surface brightness profile.

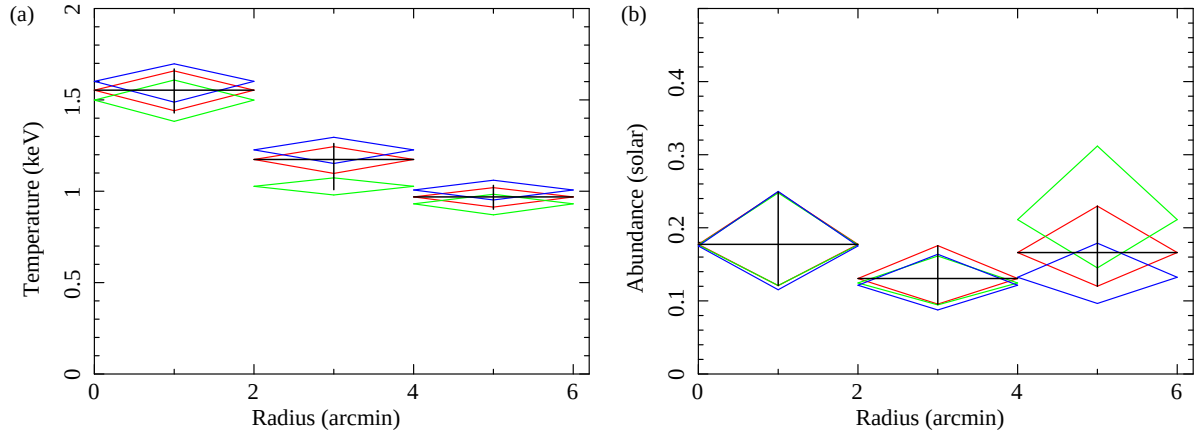

Figure 6.15: (a) Temperature and (b) metallicity profiles of A2804.

6.3.8 A2811

Suzaku carried out two pointing observations for A2811. The XIS images are shown in Fig. 6.16(a). We extract spectra from six annular regions of 0′–2′, 2′–4′, 4′–6′, 6′–9′, 9′–13′, and 13′–20′, centered on (RA, Dec) = ($00^{\rm h}42^{\rm m}09^{\rm s}.2$, $-28°31'56''$). We fit the surface brightness profile shown in Fig. 6.16(b) with a β-model and generate the β-ARF by using the model. As described in subsection 6.3.6, using $\Gamma_{\rm CXB} = 1.413$ and $N_{\rm CXB} = 8.242 \times 10^{-4}$ photons keV^{-1} cm^{-2} s^{-1} at 1 keV, we perform the spectral analysis. The temperature and abundance profiles are shown in Fig. 6.17.

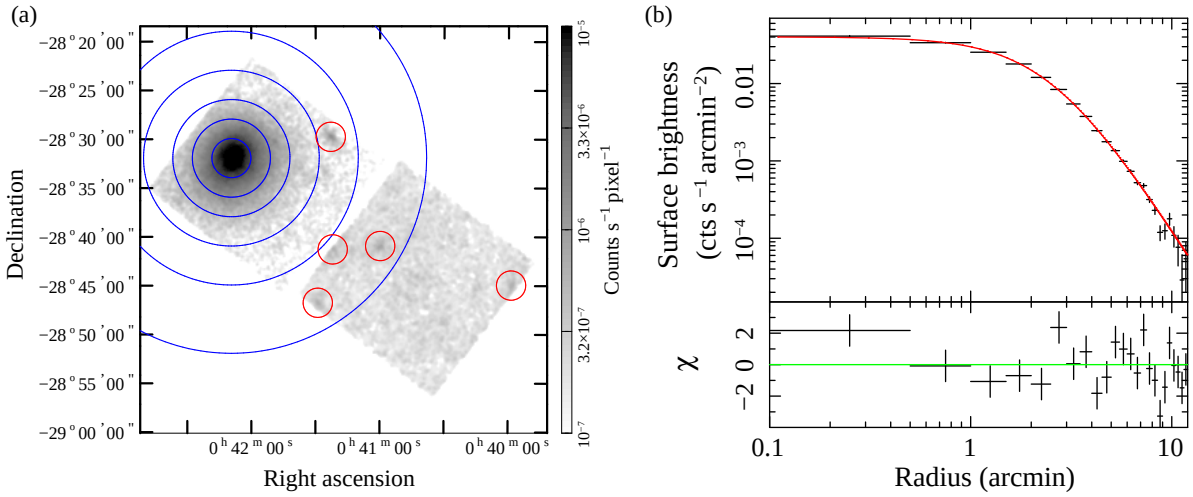

Figure 6.16: (a) A2811 X-ray image. The blue lines show the circular regions of the radii = 2′, 4′, 6′, 9′, 13′, and 20′. (b) Surface brightness profile.

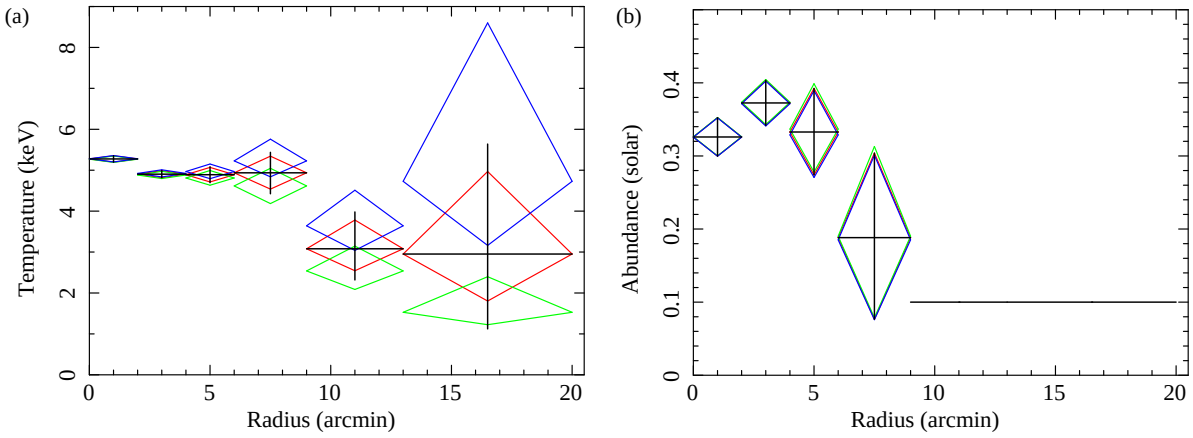

Figure 6.17: (a) Temperature and (b) metallicity profiles of A2811.

6.4 Surface brightness profile

6.4.1 Scaled surface brightness profile

Figure 6.18 shows the surface brightness profiles for the sample regular clusters. It is observed that these clusters have various surface brightness and cluster scales. In order to discuss the general trend of their surface brightness, we normalize the surface brightness profiles as discussed by Neumann & Arnaud (1999).

The emission measure along the line of sight at radius r, $EM(r)$, can be deduced from the X-ray surface brightness, $S(\theta)$, as

$$EM(r) = \frac{4\pi(1+z)^4 S(\theta)}{\Lambda(T,z)} \ ; \ r = D_A(z)\ \theta \ , \tag{6.2}$$

where $\Lambda(T,z)$ is the emissivity, and $D_A(z)$ is the angular distance at redshift z. $\Lambda(T,z)$ weakly depends on the redshift and is approximately proportional to $T^{1/2}$. Therefore, under the approximation that the ICM is isothermal, we newly define $EM'(r)$ as

$$EM(r) \propto \frac{4\pi(1+z)^4 S(\theta)}{T_X^{1/2}} \equiv EM'(r) \ , \tag{6.3}$$

where T_X is the global temperature of the sample cluster. On the other hand, the emission measure is related to the gas density n_g by

$$EM(r) = \int_r^\infty \frac{n_g^2(R) R}{\sqrt{R^2 - r^2}}\, dR \ . \tag{6.4}$$

The shape of the surface brightness profile is thus governed by the form of the gas distribution, whereas its normalization depends also on the cluster's overall gas content. The gas content can be estimated from the virial radius and the virial mass, as described in subsection 2.3.4. Using eqs. (2.31) and (2.32), the emission measure (eq. 6.3) then scales as

$$EM(r) \propto f_{gas}^2\, T_X^{1/2}\, (1+z)^{9/2}\, SEM(x) \ , \tag{6.5}$$

where $x = r/r_{180}$ is the scaled radius, and SEM is a dimensionless function that is the same for all clusters. The gas mass fraction f_{gas} is not necessarily a constant but similarity implies that it only depends on the cluster mass (or equivalently temperature).

Thus, we consider the observed scaled emission measure $SEM_X(x)$,

$$SEM_X(x) = \frac{S(\theta(x))}{(1+z)^{1/2}\, T_X} \ ; \ \theta(x) = x \frac{r_{180}}{D_A(z)} \ , \tag{6.6}$$

defined from eqs. (6.3) and (6.5) ignoring possible variation of f_{gas} with T_X. Using T_X listed in table 6.1, we calculate the scaled emission measure profiles shown in Fig.

6.19(b). They can be compared to the corresponding unscaled profiles $EM'(r)$ plotted in Fig. 6.19(a). We note that the scaling procedure has significantly decreased the difference between the unscaled profiles, but only in the outer region ($r/r_{180} \gtrsim 0.2$). However, the scaled profile of A1060 is relatively different from the general trend. This might be because the global temperature T_X of A1060 is overestimated. Since A1060 is a very nearby cluster at a redshift of 0.0114, further offset observations are required to determine the actual global temperature. If the actual value is $T_X = 2.5\,\mathrm{keV}$, the scaled profile corresponds with the general trend. The details about A1060 are discussed by Sato et al. (2007). Therefore, excepting A1060, we calculate a relative standard deviation of the profiles. The unscaled emission measures EM' show a relative standard deviation of about 148% in the 0–180 kpc range and 73% in the 720–900 kpc range. In comparison, the relative standard deviation of the scaled profiles is 94% in the $r/r_{180} \leq 0.1$ range and 34% in the $0.4 < r/r_{180} \leq 0.5$ range. The scaling procedure has thus reduced the scatter by about a factor of two. However, in the central regions ($r/r_{180} \lesssim 0.2$), the profiles still show a large dispersion. Since the scaled emission measure is a dimensionless function, for further quantitative discussions, we calculate the central gas densities in the next subsection.

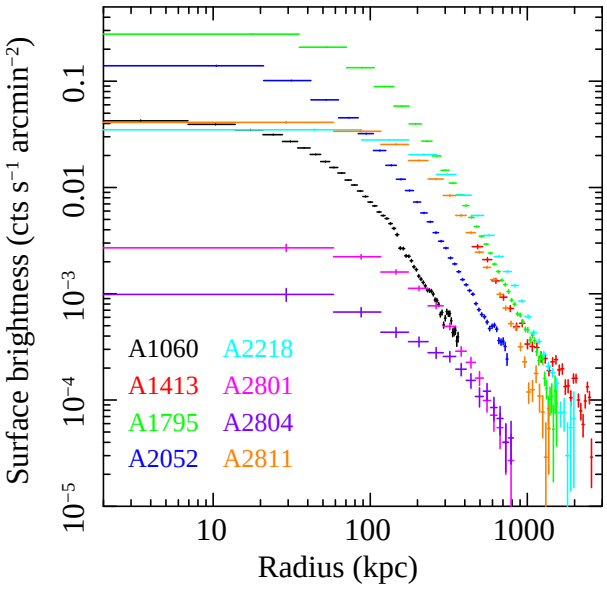

Figure 6.18: Surface brightness profiles of the sample clusters. The profiles were corrected for vignetting effects and the background was subtracted. The surface brightness was obtained by averaging four XISs.

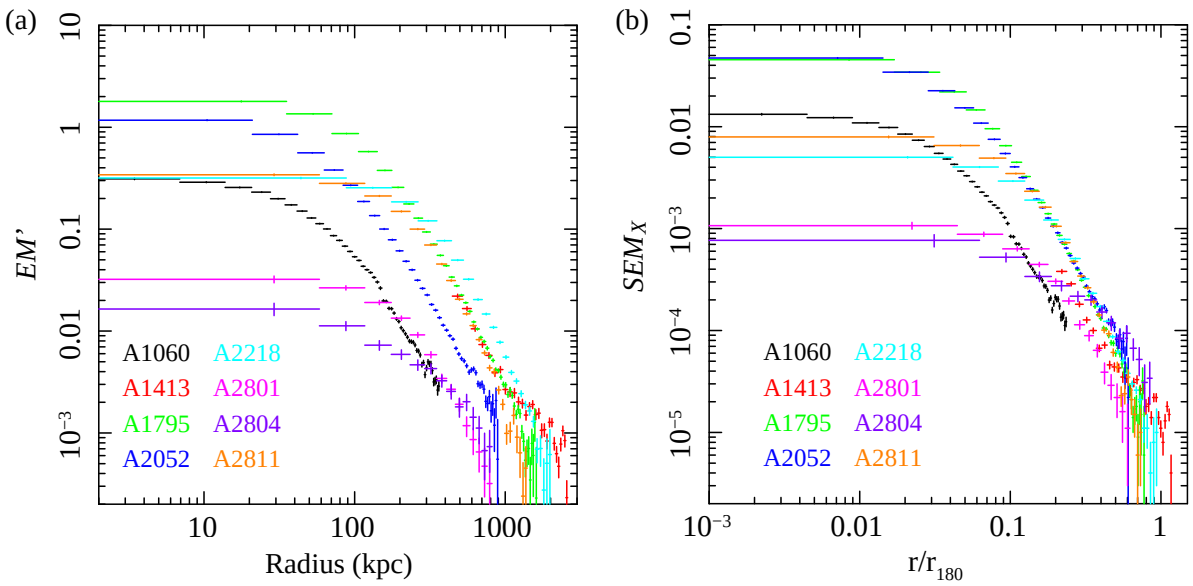

Figure 6.19: (a) Unscaled emission measure profiles (eq. 6.3) of the sample clusters. (b) Scaled emission measure profiles (eq. 6.6). The radius is normalized to r_{180} (eq. 2.30). Beyond $r/r_{180} \sim 0.2$, the profiles appear remarkably similar.

Table 6.3: Best-fit parameters of the β-model and the central gas density

Name		S_0* (10^{-2} cts s^{-1} arcmin^{-2})	r_c (arcmin)	β	Reduced-χ^2	Reference	n_{g0} (10^{-2} cm^{-3})
A1060†	Narrower	0.0454‡	3.7	1.3	-	Sato et al. (2007)	0.99
	Wider	0.035‡	7.3	0.69	-		
A1795†	Narrower	0.51§	0.438	0.562	-	Ikebe et al. (2004)	3.5
	Wider	0.069§	1.77	0.633	-		
A2052†	Narrower	10.9 ± 1.6	1.01 ± 0.11	0.535 ± 0.012	2.08		1.6
	Wider	3.9 ± 1.7	2.72 ± 0.58	0.714 ± 0.089			
A2218		3.545 ± 0.049	2.160 ± 0.044	0.816 ± 0.012	1.40		0.38
A2801		0.269 ± 0.021	2.41 ± 0.41	0.85 ± 0.13	0.25		0.11
A2804		0.086 ± 0.022	1.26 ± 0.61	0.431 ± 0.077	0.90		0.082
A2811		4.012 ± 0.067	2.558 ± 0.066	0.859 ± 0.017	2.14		0.42

* Surface brightness in the 1–5 keV band at the cluster center, excepting A1060 and A1795.

† Double β-model was applied.

‡ Surface brightness in the 0.8–3 keV band of XMM EPIC.

§ Surface brightness in the 0.8–10 keV band of XMM EPIC.

6.4.2 Central regions of clusters

The emission measures that we obtained by the spectral analysis are the projected squared gas densities. In order to obtain the central gas density, the radial density profile of the gas is required. Therefore, since the surface brightness profiles can be well reproduced by the β-model or the double β-model, we assume that the gas density profile also obeys these models.

Here, we describe the calculation procedure of the central gas density. The emission measure of the APEC model in XSPEC is defined by

$$EM_{\rm APEC} = \frac{10^{-14}}{4\pi[D_A(1+z)]^2} \int n_e n_p \, dV \ , \tag{6.7}$$

where n_e and n_p are the electron and proton densities, respectively. Here, we assume $n_p = 0.82 n_e$ in the ionized ICM and $n_g = n_e$. Under the approximation that the gas density obeys the β-model eq. (2.25), eq. (6.7) can be converted as follows

$$EM_{\rm APEC} = \frac{10^{-14}}{4\pi[D_A(1+z)]^2} \int 0.82\, n_{g0}^2 \, \left[1+(r/r_c)^2\right]^{-3\beta} \, dV \ , \tag{6.8}$$

$$= X(D_A, z)\, n_{g0}^2 \, r_c \, A(\beta) \int \left[1+(r/r_c)^2\right]^{-3\beta+1/2} \, dS \ , \tag{6.9}$$

where

$$X(D_A, z) = \frac{0.82 \times 10^{-14}}{4\pi[D_A(1+z)]^2} \ , \tag{6.10}$$

$$A(\beta) = \int_{-\pi/2}^{\pi/2} (\cos\theta)^{6\beta-2} \, d\theta \, . \tag{6.11}$$

If the central region considered for spectral analysis is a circular region of radius r_0, its emission measure, $EM_{\rm APEC,0}$, can be simplified as

$$EM_{\rm APEC,0} = X(D_A, z)\, n_{g0}^2 \, r_c \, A(\beta) \int_0^{r_0} 2\pi r \, \left[1+(r/r_c)^2\right]^{-3\beta+1/2} \, dr \ , \tag{6.12}$$

$$= \frac{\pi \, n_{g0}^2 \, r_c^3 \, X(D_A, z) \, A(\beta)}{-3\beta + 3/2} \, \left[\left\{ 1+(r_0/r_c)^2 \right\}^{-3\beta+3/2} - 1 \right] \ . \tag{6.13}$$

Although this is an equation for the β-model, this calculation procedure can be applied in the similar way for the double β-model. Thus, we calculate the central gas densities and summarize them in table 6.3.

We should note that these densities are preliminary values (therefore, their errors were not estimated). This is because the Suzaku XRT has relatively low angular resolution, and the projection effect has not been considered in our spectral analysis. However, our results for the densities of A1060 and A1795 correspond relatively well with those reported

in table 5.4 of Katayama (2003), namely, 0.68×10^{-2} cm^{-3} for A1060 and 3.96×10^{-2} cm^{-3} for A1795. Katayama (2003) measured the central gas densities of the sample clusters from the spectral analysis of Chandra observations by considering the Chandra PSF and the projection effect.

Our results suggest that the central gas densities of strong-cooling-core clusters, i.e., A1795 and A2052, are higher than those of weak or non cooling-core clusters, i.e., A2218. The cooling-core clusters also have high scaled emission measures at their centers because the X-ray emission depends on the squared gas density. Therefore, the presence of cooling cores of various strengths most probably explains the large scatter of the scaled emission measure at the cluster centers ($\lesssim 0.2 r_{180}$) (Fig. 6.19b). Neumann & Arnaud (1999) also reported the large scatter of the scaled emission measure profiles in the central regions by using 26 cluster observations with ROSAT.

A cooling core is explained by the radiative-cooling time-scale of the ICM. The cooling time, $t_{cool} = (d \ln T_g/dt)^{-1}$, is expressed as

$$t_{cool} = 8.5 \times 10^{10} \text{ yr} \left(\frac{n_g}{10^{-3} \text{ cm}^{-3}}\right)^{-1} \left(\frac{T_g}{10^8 \text{ K}}\right)^{1/2} , \tag{6.14}$$

where T_g is the gas temperature, t_{cool} is longer in most regions of a cluster than the Hubble time (age of the universe). However, at the centers of some clusters, the gas densities are higher than 10^{-2} cm^{-3}, where the cooling time is $t_{cool} \sim 10^8$–10^9 yr. In fact, X-ray observations, including our results, have revealed that the central gas of some clusters is cooled down, and its radiative cooling time is shorter than the Hubble time. In addition, the large scatter of the scaled emission measures, which we observed at the cluster centers, favors a scenario where the cooling cores are recurrent phenomena that are periodically erased by strong mergers. In this case, the large scatter of the scaled emission measures at the cluster centers would naturally reflect the statistics of the formation process via merger events.

However, the phenomena at the cluster centers have not yet been fully understood. For example, there is the following problem with the cooling flow model: This model predicts that a large amount of gas, $\sim 100 M_\odot/\text{yr}^{-1}$, is flowing into the cluster center to explain the X-ray spectrum emitted by the cluster center. However, such cooling flows have not been detected, hence this model cannot account for the said X-ray emissions. The ASCA observations (Makishima et al. 2001) also indicated that the mass of the flowing gas is much smaller than that predicted by the cooling flow model. Moreover, the observations with the reflection grating spectrometer on XMM-Newton (Peterson et al. 2003; Tamura et al. 2001) revealed a lack of emission from cool (<1–2 keV) gas in the cluster centers, which specifically indicated that the gas in the central regions of the

cooling-core clusters are very little cooled down. Therefore, the cooling flow model is recently thought to be unlikely. The results of Peterson et al. (2003) and Tamura et al. (2001) also suggested that there are extra heat sources at the cluster centers. Although AGN or thermal conduction are mainly suggested as the heat sources, the phenomena at the cluster centers are still under vigorous debate.

6.5 Temperature profile

It is widely believed that clusters should approximately have the scaling relations because they form scale-free density perturbations and their dynamics are governed by the scale-free gravitational force. Self-similarity implies, in particular, that the cluster temperature (and surface brightness, etc.) profiles are similar when their radii are scaled to their virial radii. In this section, this prediction is confirmed by our measurements.

6.5.1 Scaled temperature profiles

We normalize the radial temperature profile of each cluster by the global temperature T_X shown in table 6.1 and plot it against the radius in units of r_{180}. The scaled temperature profiles are shown in Fig. 6.20(b). They can be compared to the corresponding unscaled profiles plotted in Fig. 6.20(a). It is clear that there is a general trend; the cluster temperature profiles decline with distance from the center. In addition, we should note that the scaling procedure significantly reduces the scatter among the profiles of various clusters in the outer regions ($r/r_{180} \gtrsim 0.15$), except for the A1060 profile. This difference in the case of the A1060 temperature profile must be caused by the same reason as that is responsible for its scaled emission measure profile (see subsection 6.4.1). In Fig. 6.20(c), the A1060 temperature profile is scaled with $T_X = 2.5\,\mathrm{keV}$. In this case, the scaled profiles of all sample regular clusters exhibit similarity from $0.15r_{180}$ to the virial radii. In contrast, in the central regions, strong scatter of the scaled temperature profiles is observed. This is not strange because in these regions, nongravitational processes such as radiative cooling and energy output from the central AGNs are important, thus breaking the similarity.

Some of the previous studies of large cluster samples with ASCA and BeppoSAX have indicated the similarity of the cluster temperature profiles at large radii ($r \lesssim 0.5$–$0.6r_{180}$) (Markevitch et al. 1998; De Grandi & Molendi 2002). More recent investigations with Chandra (Vikhlinin et al. 2005) and XMM-Newton (Pratt et al. 2007) have allowed better constraints on the temperature profiles in the outer regions up to 0.5–$0.6r_{180}$. Our measurements agree well with these earlier results within 0.5–$0.6r_{180}$ and have extended the temperature profiles up to the virial radii. In particular, we have shown the similarity

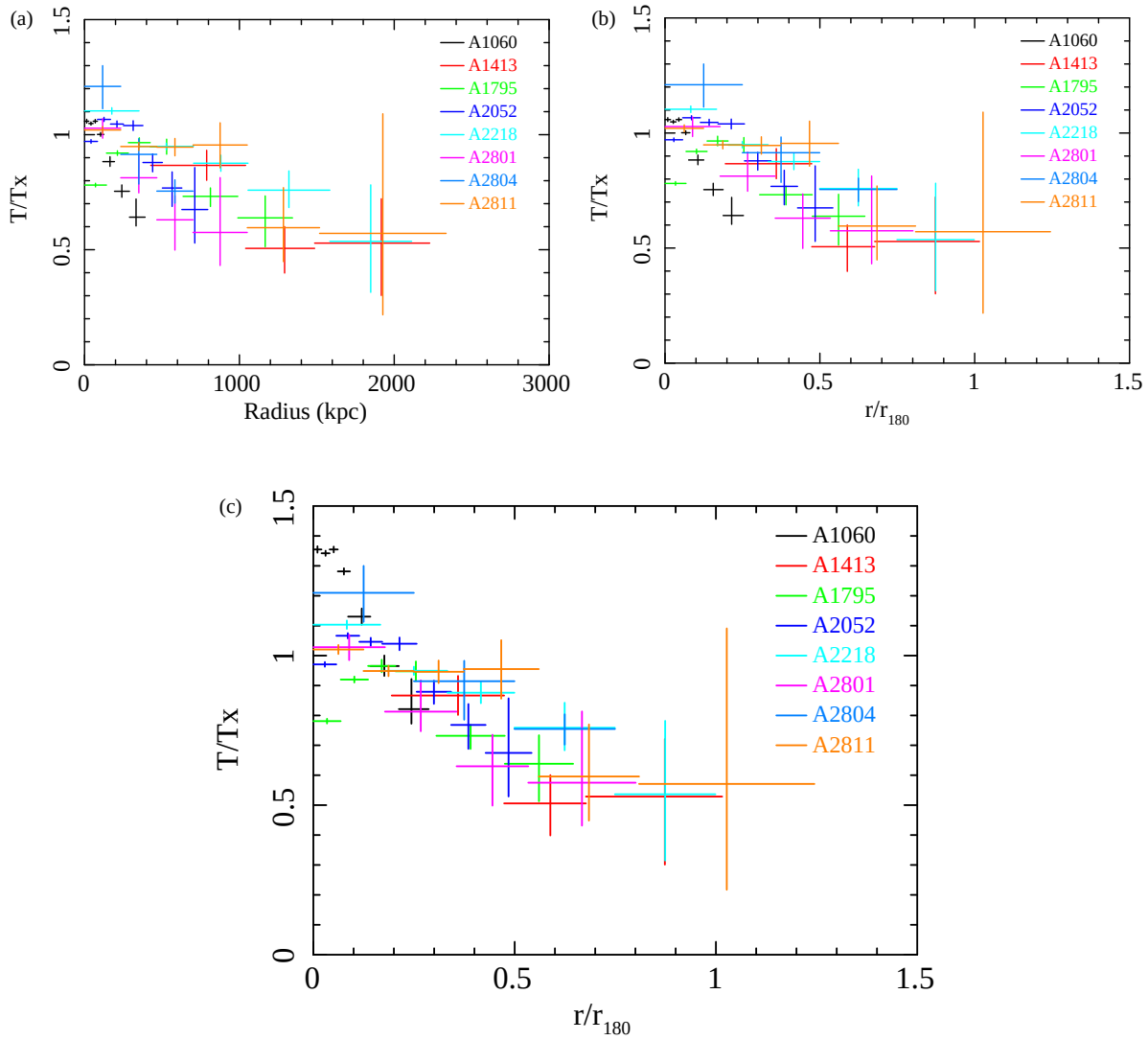

Figure 6.20: Temperature profiles for the sample regular clusters plotted as a function of (a) distance from the center and (b) in units of the cluster virial radius. The temperatures have been scaled to the cluster global temperature T_X. (c) is the same as (b), but the temperature profile of A1060 is scaled with $T_X = 2.5\,\mathrm{keV}$.

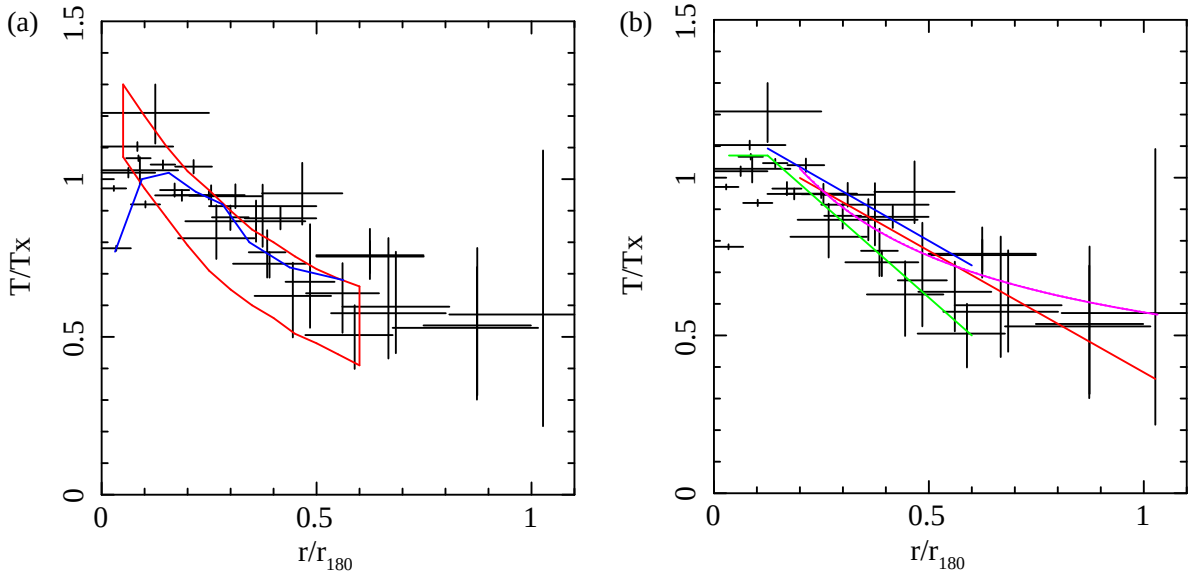

Figure 6.21: (a) Scaled projected temperature profiles compared with the average profiles from ASCA (Markevitch et al. 1998) and BeppoSAX (De Grandi & Molendi 2002). The black crosses show our results for all sample clusters, except for A1060. ASCA results are shown as the red band with the width equal to the scatter of the best-fit values in a sample of 30 clusters. BeppoSAX results (blue line) represent the average temperature profile in a sample of 11 cooling core clusters. (b) is same as (a), but comparison with the results of Chandra (green line, Vikhlinin et al. 2005) and XMM-Newton (blue line, Pratt et al. 2007) are shown. The red and magenta lines show the best fits to the XIS data obtained by using the linear line model and the polytropic model, respectively.

of the temperature profiles in the region of $r > 0.6r_{180}$ for the first time. The comparisons of our temperature profiles with those obtained from ASCA, BeppoSAX, Chandra, and XMM-Newton are shown in Fig. 6.21. There is a tendency that our temperature profiles lie around the upper edge of the envelope (red band in Fig. 6.21(a)) of the ASCA results. We note that the same tendency is observed in other missions. However, the definitions of the global temperature T_X differ between studies, making exact comparison between different results rather difficult.

Here, we fit the scaled temperature profiles in the outer region ($r/r_{180} > 0.2$) where the profiles exhibit similarity, except for A1060. First, we adopt a simple linear line model as

$$T/T_X = a - b\,x \quad (x > 0.2)\ , \tag{6.15}$$

where x is r/r_{180}. The best-fit model is plotted by the red line in Fig. 6.21(b), and its parameters are summarized in table 6.4. It shows that in general, temperatures decline with radius. In addition, the line we obtained is approximately consistent with those of Chandra and XMM-Newton, as shown in Fig. 6.21(b).

The linear line model is only a phenomenological model with no physical basis. Next, we compare our data with a polytropic model. The details about this model were introduced in subsection 2.3.5. It expresses the projected temperature profile as

$$\frac{T}{T_X} = t_0 \left[1 + \left(\frac{x}{x_c}\right)^2\right]^{-1.5\beta(\gamma-1)}\ , \tag{6.16}$$

where x_c is r_c/r_{180}, and t_0 is the scaled temperature at $x = 0$. x_c and β are set equal to 0.13 and 0.71, respectively, which match with the mean values we obtained by fitting the surface brightness profiles (table 6.3). We fit the temperature profiles in the outer region ($r/r_{180} > 0.2$) and list the best-fit parameters in table 6.4. The best-fit polytropic model is shown by the magenta line in Fig. 6.21(b). We note that the χ^2 value of the polytropic model is smaller than that of the linear line model. This indicates that the temperature profile is best fitted by asymptotical decline rather than straight-line decline. Meanwhile, the γ parameter represents the gas condition. Note that $\gamma = 1$ corresponds to the isothermal case, and $\gamma = 5/3$ describes the adiabatic case. Our best-fit value of the γ parameter is contained within these two cases and is closer to the isothermal value. This value is approximately consistent with the previous results of ASCA ($\gamma = 1.24^{+0.08}_{-0.11}$) (Markevitch et al. 1998).

The decrease in temperature with the cluster radius is probably explained by thermal conduction. Within the ICM, the thermal conduction will transport heat from hot to

Table 6.4: Best-fit parameters for the scaled temperature profiles

Linear			Polytropic*		
a	b	χ^2/dof	t_0	γ	χ^2/dof
1.153 ± 0.043	-0.77 ± 0.13	37.2/21	1.316 ± 0.085	1.190 ± 0.034	31.3/21

Errors are 90% confidence level.

* β and x_c for the polytropic model are set equal to 0.71 and 0.13, respectively.

cold regions and, in the absence of any competing effect, make the temperature spatially constant (isothermal). If the cluster potential is given by the analytic King form (eq. 2.16), and if the gas is assumed to cool isobarically (at constant pressure), the conduction time, $t_{cond} = -(d \ln T_g/dt)^{-1}$, at radius r is given by

$$t_{cond}(\xi) = \frac{3.3 \times 10^8}{g(\xi)} \text{ yr } \left(\frac{n_{g0}}{10^{-3} \text{ cm}^{-3}}\right) \left(\frac{T_g}{10^8 \text{ K}}\right)^{-5/2} \times \left(\frac{r_c}{0.25 \text{ Mpc}}\right)^2 \left(\frac{\ln \Lambda}{40}\right) , \quad (6.17)$$

where $\xi = r/r_c$, and Λ is the emission per ion at unit electron density. The function $g(\xi)$ is

$$g(\xi) = \left(\xi^2 + 1\right)^{-3/2} - \frac{5}{2\xi^2 f(\xi)} \left[f(\xi) - (\xi^2 + 1)^{-1/2}\right]^2 , \quad (6.18)$$

where $f(\xi) = \phi(r)/\phi_0$ is the ratio of the cluster potential to its central value and is given by eq. (2.16). The function $g(\xi)$ is plotted in Fig. 6.22. It is clear from this figure that thermal conduction is most effective in the cluster core, and the conduction time increases very rapidly with radius. At radii $r \gtrsim 2r_c \sim 0.5\,\text{Mpc}$, the conduction time is typically a factor of $\sim$100 longer, which is $t_{cond} \sim 3.3 \times 10^{10}$ yr. Thus, since this time scale is longer than the Hubble time, the thermal conduction is only marginally effective in the outer parts of the cluster, and temperature gradients still exist in almost all clusters.

In contrast, at the center ($r \sim 0$), the conduction time is $t_{cond} \sim 3.3 \times 10^8$ yr, which is much shorter than the Hubble time. If the thermal conduction is effective, the temperature distribution at the cluster centers should be isothermal. In fact, some non cooling core clusters, e.g. A2218 (Machacek et al. 2002), have isothermal regions at their centers. However, some clusters such as A1795 and A2052 have cooling cores at their centers, which indicate that the centers are not isothermal. This could be because the thermal conduction is suppressed by the magnetic field around a cooling core.

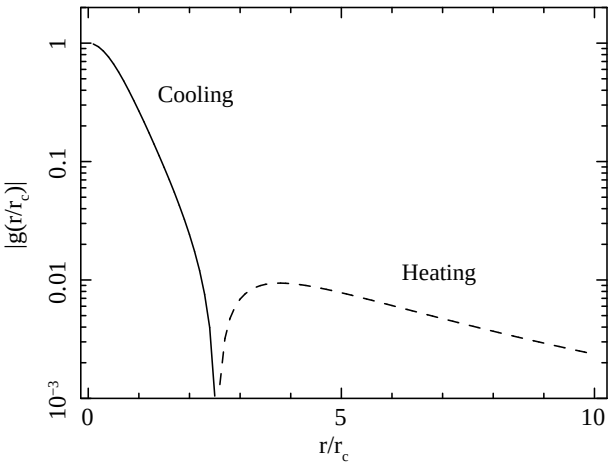

Figure 6.22: The function $g(r/r_c)$ as a function of radius. The conduction time is in inverse proportion to $g(r/r_c)$, and the radius is in units of the cluster core radius r_c. The solid (dashed) curve indicates the portion of the cluster where the gas is cooled (heated) by conduction.

6.5.2 Comparison with simulations

Although earlier simulations were more discrepant and produced both nearly isothermal profiles (Evrard et al. 1996) and strong temperature gradients (Katz & White 1993), declining temperature profiles in the outer region ($r \gtrsim 0.15 r_{180}$) are generally reproduced by recent cosmological hydrodynamical simulations in cold dark matter (CDM) model, e.g., Loken et al. (2002), Borgani et al. (2004), and Ettori et al. (2004). These recent simulations agree well with the temperature profiles observed with ASCA (Markevitch et al. 1998), BeppoSAX (De Grandi & Molendi 2002), Chandra (Vikhlinin et al. 2005), and XMM-Newton (Pratt et al. 2007). Vikhlinin et al. (2005) also reported that the best agreement with the observed temperature profiles appears to be reached by Eulerian codes (Loken et al. 2002 and discussion therein) and by the entropy-conserving versions of the smoothed particle dynamics (SPH) code (Springel & Hernquist 2002) used, e.g., by Ascasibar et al. (2003), Kay et al (2004), and Borgani et al. (2004).

Therefore, we compare our results with the simulated projected profiles of all clusters with $kT > 2\,\mathrm{keV}$ from Borgani et al. (2004), in which the SPH code GADGET-2 (Springel 2005) was used to simulate a concordance ΛCDM model ($\Omega_\mathrm{M} = 0.3$, $\Omega_\Lambda = 0.7$, $\sigma_8 = 0.8$, $h = 0.7$) within a box of $192\,h^{-1}\,\mathrm{Mpc}$ on a side, using 480^3 dark matter and an equal number of gas particles. The simulation included radiative cooling, star formation, and galactic ejecta powered by supernova feedback. Figure 6.23 shows this comparison. The simulation profiles were scaled using the emission-weighted global temperature, with a further 8% adjustment so that the normalization in the $0.15 < r/r_{180} < 0.5$ region is

the same as that of the observed profiles. This adjustment is necessary because the emission-weighted global temperature is not the same as the measured spectral global temperature T_X. We note that the adjustment value is the same as that reported by Pratt et al. (2007). The scatter in the simulated profiles is noticeable and originates from the accretion of colder subclumps onto the main cluster and shock fronts due to supersonic accretion. Thus, our temperature profiles agree well with the simulation from $0.15r_{180}$ up to the virial radius.

Next, we compare our results with the temperature profile simulated by Loken et al. (2002). Figure 6.23 shows their simulated profile, which was obtained by fitting their entire sample of symmetric clusters, by the blue line. The profile of Loken et al. (2002) is generally lower and has slightly steeper gradient than those of our results and Borgani et al. (2004). It is unclear whether the discrepancy is due to the differences between the simulation codes or the supernova feedback models or both. However, Loken et al. (2002) reported that the temperature profiles in the outer region ($r \gtrsim 0.6r_{180}$) are scarcely dependent on the physical processes included in the simulations, i.e., the radiative cooling and the supernova feedback. Therefore, the discrepancy between the simulated temperature profiles of Borgani et al. (2004) and Loken et al. (2002) might be due to the differences between the simulation codes.

Our temperature profiles agree well with those simulated by Borgani et al. (2004) from $0.15r_{180}$ to the virial radii. However, in the central regions, there are relatively large discrepancies between the observed and simulated temperature profiles. The peak of the simulated temperature profiles lies at $\sim 0.04r_{180}$, while that of the observed profiles lies at $\sim 0.15r_{180}$. This might be due to the facts that the physical process of the cooling cores is still unclear, as described in subsection 6.4.2, and our profiles are uncorrected for the PSF effect, i.e., stray light. We note that a similar difference in the peak position (as compared to the simulations) is also evident when the simulation results are compared with the Chandra results (Vikhlinin et al. 2005) or the XMM-Newton results (Pratt et al. 2007). A more detailed comparison with the observations of the cluster centers requires folding the simulation output through the detector response, but this is beyond the scope of this thesis. Nevertheless, we believe that the agreement between the simulated and observed clusters is quite good, and the numerical simulations can describe the global thermal structure of the ICM. This agreement and the scaling relations for the ICM temperature and density indicate that the ICM is dominantly heated by gravitational processes of cluster formation.

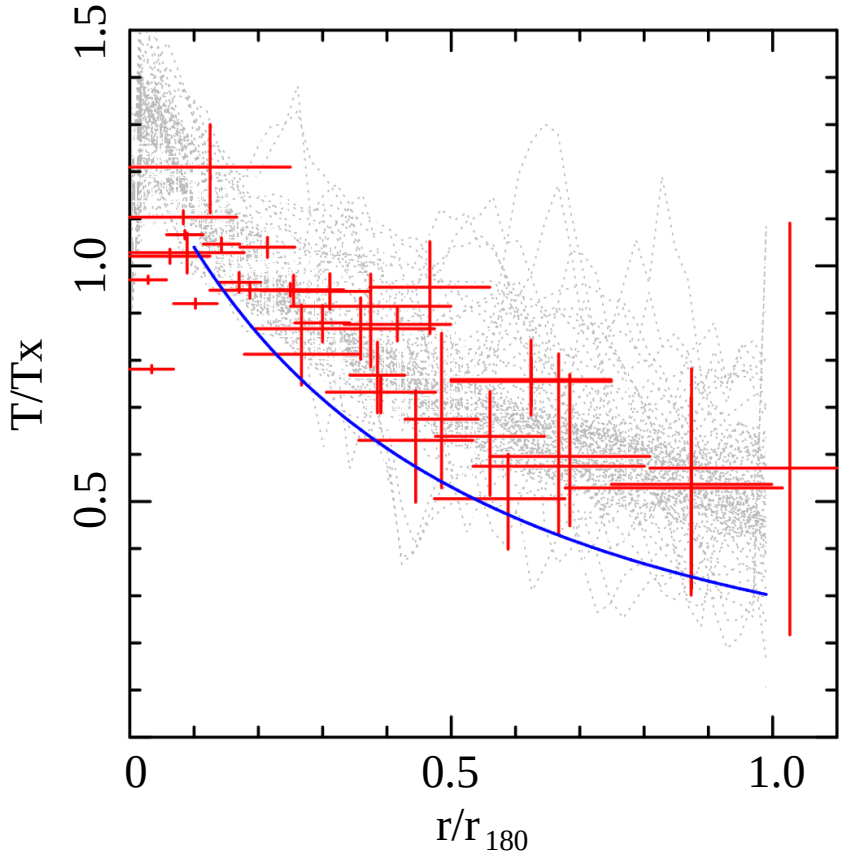

Figure 6.23: Scaled projected temperature profiles compared with the projected profiles from the simulations of Borgani et al. (2004) (black dotted lines) and Loken et al. (2002) (blue line). The simulated profiles of Borgani et al. (2004) are scaled using the mean emission-weighted temperature, with a further adjustment of 8% to take into account the difference between the two definitions of global temperature used to scale the profiles. The simulated profiles are taken from Fig. 6 of Pratt et al. (2007). The blue line shows the simulated profile obtained by Loken et al. (2002).

6.5.3 Mass–temperature relation

In this subsection, we discuss the relation between the total gravitating mass and the ICM temperature, which is called "M–T relation". In order to derive the total gravitating mass, we utilize the fact that the temperature profiles can be described by a polytropic model. Since we fitted the observed temperature profiles with the polytropic model (eq. 6.16) weighted with the surface brightness along the line of sight (see eq. 2.41), a three-dimensional temperature profile $T(r)$ (eq. 2.40) is expressed as

$$T(r) = t_0 T_X \frac{A(\beta)}{B(\beta,\gamma)} \left[1 + \left(\frac{r}{r_c}\right)^2\right]^{-(3\beta/2)(\gamma-1)}, \tag{6.19}$$

where

$$A(\beta) = \int_{-\pi/2}^{\pi/2} (\cos\theta)^{6\beta-2}\, d\theta, \tag{6.20}$$

$$B(\beta,\gamma) = \int_{-\pi/2}^{\pi/2} (\cos\theta)^{3\beta(\gamma+1)-2}\, d\theta. \tag{6.21}$$

Under the assumption that the ICM is in hydrostatic equilibrium, the total gravitating mass is expressed as eq. (2.10). In addition, assuming a spherically symmetric gas density distribution of the β-model (eq. 2.25) form and assuming the polytropic temperature profile (eq. 6.19), eq. (2.10) is converted as follows:

$$M(<r) = rT_X \frac{3k\beta\gamma t_0}{\mu m_p G} \frac{A(\beta)}{B(\beta,\gamma)} \left(\frac{r}{r_c}\right)^2 \left[1 + \left(\frac{r}{r_c}\right)^2\right]^{-(3\beta/2)(\gamma-1)-1}, \tag{6.22}$$

where, k, μ ($\sim$0.6), m_p, and G are the Boltzmann constant, mean molecular weight, the proton mass, and the gravitational constant, respectively. We calculate the virial mass M_{500}. Using the r_δ–T relation relation reported by Evrard et al. (1996) and the best-fit parameters of the polytropic model ($t_0 = 1.316$, $\gamma = 1.190$) and the β-model ($\beta = 0.71$, $r_c = 0.13 r_{180}$), we can derive the virial mass M_{500} as

$$M_{500} = \left(2.60 \times 10^{13}\right) \left(\frac{T_X}{\mathrm{keV}}\right)^{3/2} h^{-1} M_\odot. \tag{6.23}$$

It signifies that if clusters have the scaling relations for the temperature and density, the virial mass should depend only on the global temperature of ICM, T_X. We compare our M–T relation (eq. 6.23) with that simulated by Borgani et al. (2004) and those obtained from the observations with ASCA (Finoguenov et al. 2001b) and XMM-Newton (Arnaud et al. 2005), as shown in Fig 6.24. Our M–T relation agrees well with those of the other studies, particularly in the temperature range of $T_X \gtrsim 3$ keV. This might be

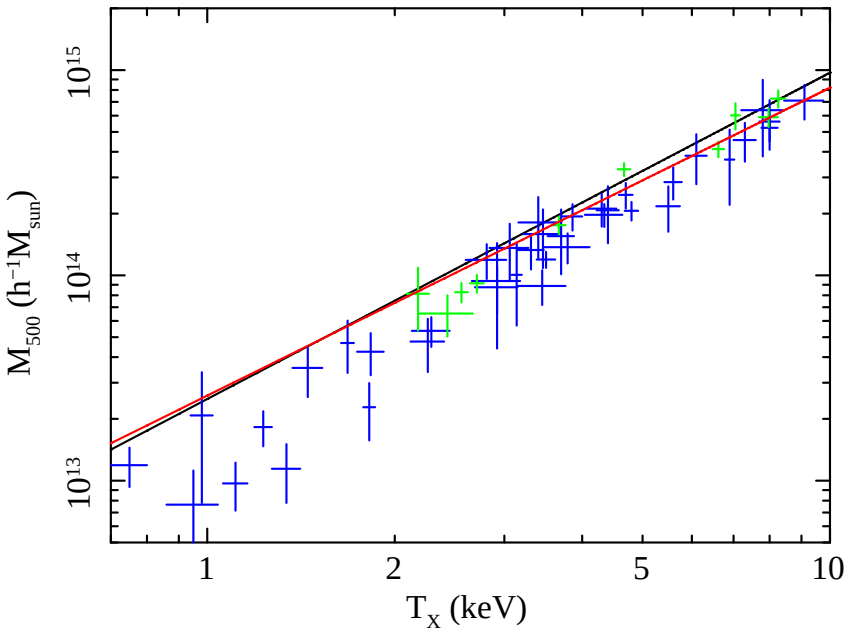

Figure 6.24: The M–T relation. The M–T relations derived from our Suzaku results (eq. 6.23) and that simulated by Borgani et al. (2004) are represented by the red and black lines, respectively. The virial masses observed by using ASCA (Finoguenov et al. 2001b) and XMM-Newton (Arnaud et al. 2005) are represented by the blue and green crosses, respectively.

because most of our sample clusters have T_X higher than $\sim$3 keV. In addition, our M–T relation is also consistent with that obtained analytically by Komatsu & Seljak (2001). These agreements assure the virial mass is estimated only with T_X as eq. (6.23) and also supported the scaling relations of clusters.

6.6 Conclusions

Suzaku XIS is best suited for the measurements of the temperature profiles up to the virial radii because of its low and stable NXB level. We have used the Suzaku observations of 8 regular clusters and measured their surface brightness and temperature profiles, which exhibit similarity in the radial range from $\sim 0.15 r_{180}$ to $\sim r_{180}$. While previous measurements of the temperature have been limited up to 0.5–0.6r_{180}, we have extended the measurements up to the virial radii. The temperatures significantly decline in the outer regions ($r \gtrsim 0.15 r_{180}$), and their general trend exhibits a polytropic index of 1.190 ± 0.034 (90% confidence level). Moreover, we have obtained the M–T relation taking advantage of the fact that the surface brightness and temperature profiles can be described by the β-model and polytropic model, respectively. Our temperature profiles and M–T relation

agree well with the previous observations and the recent numerical simulations in the CDM model. These results indicate that the global temperature of ICM T_X is good proxy for the total gravitating mass, and that the ICM is dominantly heated by gravitational processes of cluster formation. Thus, the observed regularity has important implications as cosmological probes.

Chapter 7

Metallicity of the ICM up to the Virial Radius

The metals in the ICM were originally produced by stars in galaxies. In the inner region of clusters ($r \lesssim 0.4 r_{180}$), the average metallicity of the ICM is $\sim 0.3 Z_{\odot}$ (Arnaud et al. 1992; Fukazawa et al. 2000). However, it is still unclear how and when the metals were transported into the ICM from cluster galaxies. Possible mechanisms that transfer metals from cluster galaxies into the ICM can be classified broadly into two types, ram-pressure stripping by the ICM and energetic outflows from the galaxies. In the former mechanism, a galaxy is moving in the ICM and the metal-enriched gas in the galaxy (interstellar medium) is stripped by the ram pressure exerted by the ICM (Gunn & Gott 1972; Fujita & Nagashima 1999; Quilis et al. 2000). The larger the density of the ambient ICM and/or the relative velocity between the galaxy and the ICM is, the larger the ram pressure exerted on the galaxy is. Thus, ram-pressure stripping is most effective at the cluster center. In the latter mechanism, galactic outflows that result from supernova explosions following active star formation in a galaxy inject metals into the ICM (De Young 1978). Since the static pressure exerted by the ICM suppresses the evolution of the galactic outflows, the latter mechanism is rather effective in the peripheral region of a cluster or the intergalactic space before the cluster forms (a proto-cluster region) (Kapferer et al. 2006). Therefore, it is critical to determine the metallicity of the ICM in the outermost region of clusters ($r \gtrsim 0.5 r_{180}$) in order to know which mechanism is dominant. Unfortunately, previous observations of metallicity have been limited to the inner region of clusters ($r \lesssim 0.4$–$0.5 r_{180}$) (De Grandi et al. 2004; Pratt et al. 2007).

Therefore, in this chapter, we study the nature of the ICM far away from the cluster center. First, we present the general trend of the metallicity profiles for sample regular clusters. Next, the cluster A1674 is spectrally analyzed. The ICM of A1674 has signifi-

cantly lower metallicity than that of typical clusters, A1674 is a rich cluster (Hashimotodani et al. 2000; Katayama et al. 2005). Finally, we investigate the link region between two clusters, A399 and A401, to study the ICM in further detail.

In this chapter, measurement uncertainties correspond to 1σ confidence level, unless otherwise specified.

7.1 Metallicity profiles of the sample regular clusters

Figure 7.1 shows the projected metallicity profiles of the sample regular clusters obtained in chapter 6 as a function of the distance from the cluster center in units of the cluster virial radius. We were able to measure the metallicity profiles of the regular clusters up to $r \sim 0.6$–$0.7 r_{180}$ for the first time. We again note that there are large uncertainties in the metallicities analysis of A1413 because the He-like Fe-Kα line overlaps with the Mn-Kα line due to its redshift, 0.143. In the central regions, there is a large scatter of the metallicity profiles, while in the outer regions ($r \gtrsim 0.4 r_{180}$), the metallicities are approximately constant at $0.2 Z_{\odot}$.

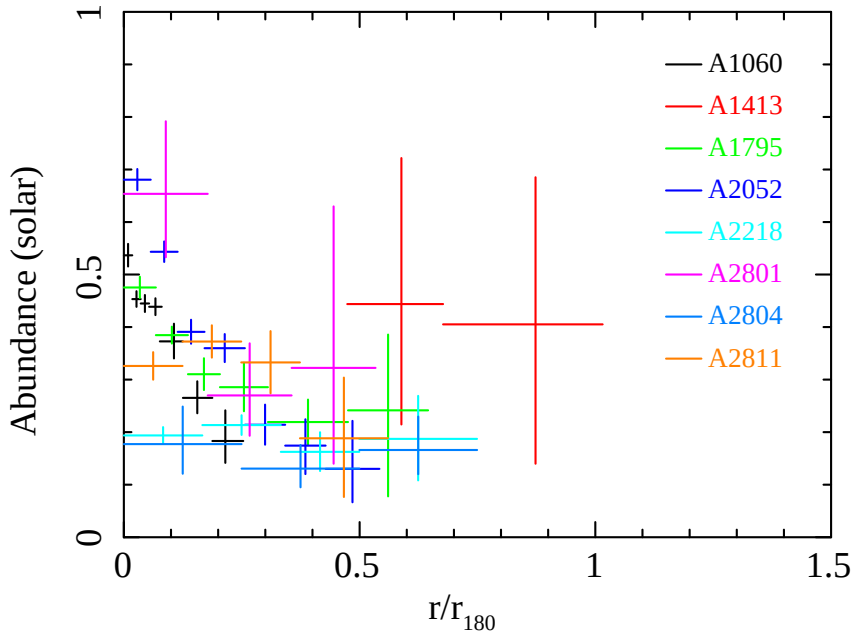

Figure 7.1: Metallicity profiles of the sample regular clusters. The radius is normalized to r_{180}.

7.2 A1674

The A1674 belongs to richness class 3; however, its X-ray luminosity is 5×10^{43} erg s^{-1} in the 0.1–2.0 keV band, which is significantly fainter than those of other clusters with comparable richness (Briel & Henry 1993). ASCA (Hashimotodani et al. 2000) and XMM-Newton (Katayama et al. 2005) observations revealed that the metallicity of its ICM is significantly low, whose upper limit was $0.2Z_{\odot}$. On the basis of optical data, Hashimotodani et al. (2000) also reported that A1674 contains significantly smaller number of elliptical galaxies, which are often thought to be the main metal sources of the ICM (Arnaud et al. 1992), than other rich clusters. Thus, A1674 was thought to be a very unique cluster.

In order to investigate the reason for its low-metallicity emission, we observed A1674 on 2006 December 16–18 using Suzaku. The details about this observation are summarized in table 7.1. The observation was not completed within the requested time of 100 ks. Since XIS2 was unusable on these observation dates, we use the data obtained using XIS0, XIS1, and XIS3. In addition, this observation data were obtained with the spaced-row charge injection (SCI) mode to improve the spectral resolution. Therefore, we use the revision 2.0 data supporting the SCI data. We also generate the NXB model from the night earth data that were obtained with the SCI-on mode between November 2006 and February 2007. Figure 7.2 shows the X-ray image of A1674 with the XIS, indicating its asymmetric X-ray morphology.

Figure 7.3 shows the two spectra for the center and SW regions (Fig. 7.2) from which the NXB spectra were subtracted. We fit the spectra using a method similar to that described in section 6.2, but setting the redshift as a free parameter. Since the spectral resolution of the SCI data is approximately consistent with the value just after the launch, we used the RMF that is essentially the same as that for the data obtained in August 2005. In addition, since the X-ray morphology of A1674 is asymmetric, we generate the ARF for the ICM emission using the XIS image. The best-fit parameters are summarized in table 7.2. Although A1674 is known as a cluster at a redshift of 0.106, the redshift of the central region is two times higher than that of A1674. In contrast, the redshift of the SW region approximately agrees with the redshift of 0.106. Therefore, we re-fit the spectrum of the center region with the redshift fixed to 0.106, and list the best-fit parameters in table 7.2. In this case, we confirm the presence of low-metallicity gas and the ASCA and XMM-Newton results. However, this model is statistically unlikely, while the model in which the redshift has been set as a free parameter is accepted.

In order to verify our results, we first compare the raw spectra, from which the NXB

spectra are not subtracted, with the NXB spectra. Figure 7.4 shows this comparison. The emission lines, Mn-Kα (5.895 keV), Ni-Kα (7.470 keV), and Au-Lα (9.671 keV), and continuous X-rays in the high energy range ($\gtrsim$ 8 keV) are well estimated; therefore, the NXB spectra have good accuracy both for the central region and for the SW region.

We further investigate the redshift of the central and SW regions on the basis of the He-like Fe-Kα line. For this purpose, we calculate the confidence contours for the redshift of He-like Fe-Kα line versus its intensity. Continuous X-rays are reproduced by a thermal bremsstrahlung model, and the He-like Fe-Kα line is reproduced by a Gaussian component, whose center energy and additional line width are fixed to 6.680 keV (Koyama et al. 2007b) and zero, respectively. Figure 7.5 shows the confidence contours of the central and SW regions. These contours show that the redshift of the central region is significantly higher than that of SW region and, the best-fit values of the redshift are 0.210 for the central region and 0.104 for the SW region. Since it is unlikely that the ICM bulk motion causes the redshift of $z \sim 0.1$ (2.9×10^4 km s^{-1}), we assume that there are two clusters in each region, and they are probably accidentally overlapped. Therefore, we probatively search the galaxies lying in the direction of A1674 by using the NASA/IPAC Extragalactic Database (NED)[1]. Note that the galaxies registered in the NED are a small fraction. However, these galaxies can be broadly classified into two redshift ranges $\sim$0.1 and $\sim$0.2 as shown in Fig. 7.2. Thus, the distributions of galaxies of $z \sim 0.1$ and $z \sim 0.2$ roughly correspond with the center and SW regions, respectively.

Therefore, we suggest that there are two clusters in A1674. One cluster is in the central region at the redshift of 0.210, and the other cluster is in the SW region at the redshift of 0.104. These clusters were not spectrally and spatially distinguished in the previous analysis; this might be due to the low angular resolution, small effective area, or short exposure time. If there are two clusters, their metallicities agree with the general value of regular clusters; this is in contrast to a rare case in which the metallicity in the cluster center is clearly lower than $0.2Z_\odot$. In addition, we should note that a situation similar to that discussed here in the case of A1674 can occur in other clusters.

7.3 A399/A401

In order to study the nature of the ICM far away from the center of a cluster, we observed the link region between two clusters, A399 and A401. The redshifts of A399 and A401 are 0.0718 and 0.0737, respectively, and the projected distance between the two clusters is 3 Mpc. Previous X-ray observations indicated that the clusters are at an initial stage

[1] ⟨ http://nedwww.ipac.caltech.edu/index.html ⟩

Table 7.1: A1674

Sequence number	801062010
Pointing direction	$(l, b) = (121.^\circ10, 49.^\circ54)$
Date	2006/12/16 – 12/18
Exposure	65.9 ks
N_H	1.85×10^{20} cm^{-2}

Table 7.2: Best-fit parameters of A1674 spectral analysis

Region	Temperature* (keV)	Metallicity* (solar)	z	χ^2/dof
Center	$4.02^{+0.16}_{-0.18}$	$0.290^{+0.043}_{-0.034}$	$0.2111^{+0.0030}_{-0.0038}$	466.9/486
	$3.92^{+0.18}_{-0.20}$	$0.046^{+0.038}_{-0.037}$	0.106 (fix)	513.9/487
SW	$2.29^{+0.17}_{-0.34}$	$0.36^{+0.08}_{-0.10}$	$0.1211^{+0.0096}_{-0.0093}$	277.5/281

* The CXB fluctuation of 12 % is taken into account in the errors.

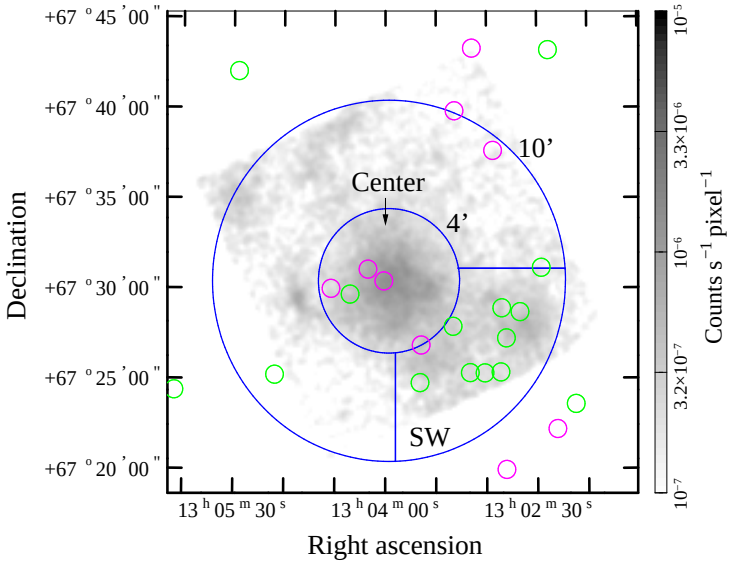

Figure 7.2: X-ray image (1–5 keV band) of A1674 with the XIS. Regions used for spectral analysis are labeled “center” and “SW.” Green and magenta circles show the galaxies at the redshifts of 0.10–0.12 and 0.21–0.23, respectively.

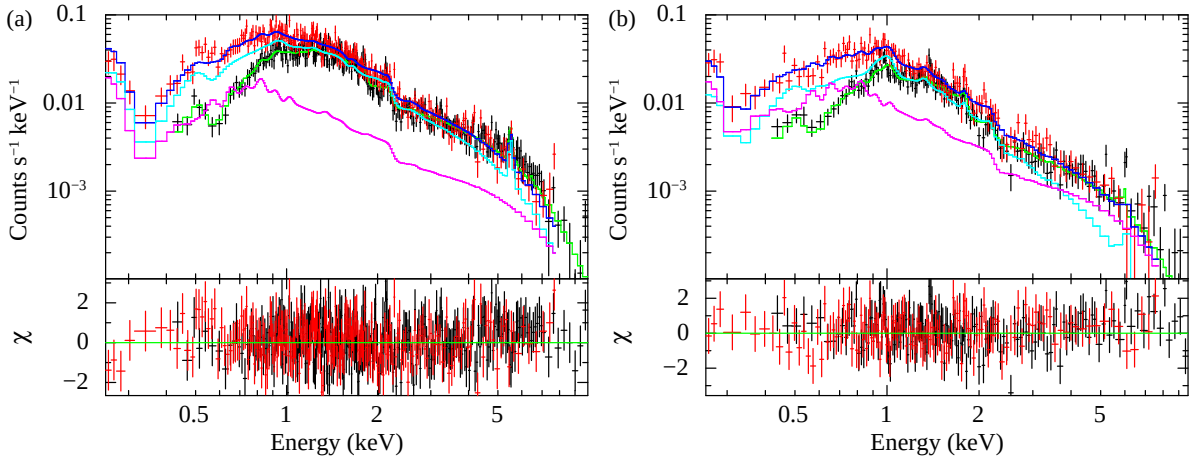

Figure 7.3: A1674 spectra of (a) the central region and (b) the SW region. Black and red crosses show the FI and BI spectra, respectively. The NXB spectra were subtracted, and the plotted data were fitted with the model in which the ICM, WABS × APEC, and the X-ray diffuse component, APEC + WABS (APEC + POWERLAW), were summed. The best-fit models are drawn by green and blue lines for the FI and BI spectra, respectively. The ICM and the diffuse X-ray component for the BI spectra are indicated by cyan and magenta lines, respectively.

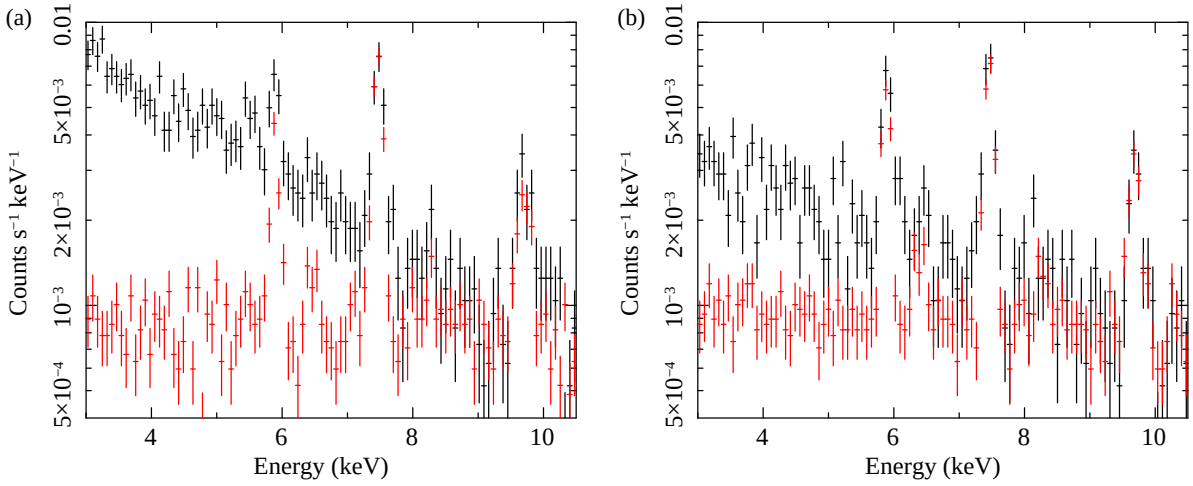

Figure 7.4: Comparison between the raw spectra of A1674 and the NXB spectra. (a) FI spectra for the central region. (b) FI spectra for the SW region. Black and red crosses show the raw spectra of A1674 and their NXB model spectra, respectively.

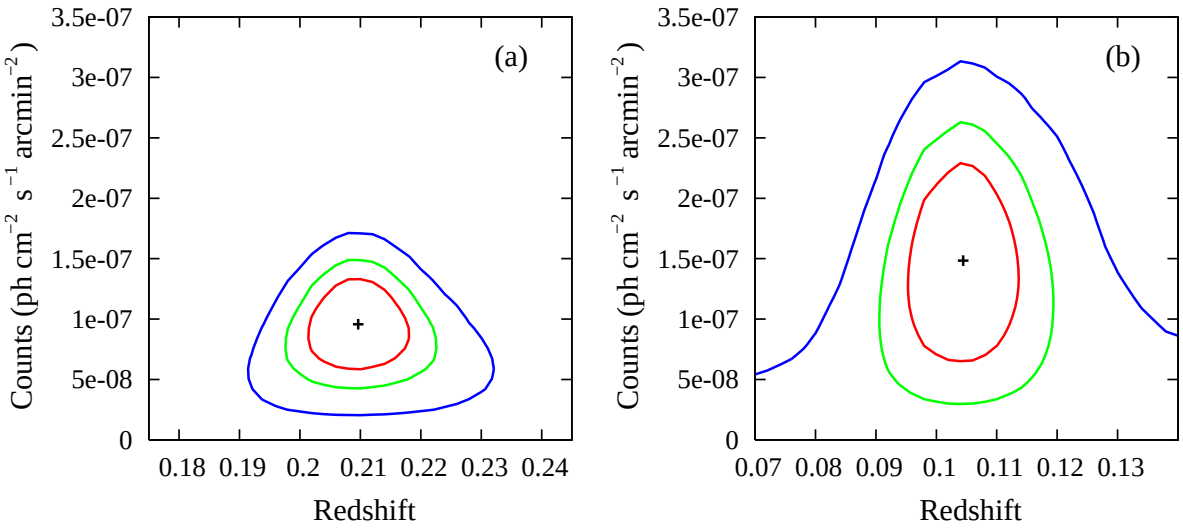

Figure 7.5: Confidence contours of A1674 for the redshift of He-like Fe-Kα line and photon counts of the Gaussian component. Red, green, and blue lines show 68%, 90%, and 99% confidence regions, respectively, for two interesting parameters. Black crosses show the best-fit values. For this figure, the fluctuation of the CXB is not considered, because the effect should be negligible.

of a cluster merger, and the hot gas in the link region is slightly compressed (Sakelliou & Ponman 2004; Fujita et al. 1996).

We observed the link region using Suzaku on 2006 August 19–22 for an exposure time of 150 ks. The observation is summarized in table 7.3. Fig. 7.6(a) shows the FOV of XIS in a ROSAT PSPC image. The region that we observed is the outermost region of the two clusters, where their virial radii, $r_{200} = 2.16$ Mpc for A399 and $r_{200} = 2.34$ Mpc for A401 (Sakelliou & Ponman 2004), cross each other.

We perform the spectral analysis by using a method similar to the one used for the regular clusters (see section 6.2). The results of this analysis have been already summarized by Fujita et al. (2008). First, we extract two spectra for regions A and B, as shown in Fig. 7.6(b). X-ray point sources in these regions are removed. Since this observation was carried out in August 2006, the emission lines in the NXB spectra cannot be well reproduced by the NXB model due to the degradation of the XIS spectral resolution. Therefore, we correct the line widths in the NXB model spectra by using the method described in section 4.3. Next, we generate the β-ARF. Since the FOV of this observation is adjacent to the cluster centers, the β-ARF is generated assuming that the surface brightness is equal to the sum of the surface brightness of the two β-models for A399 and A401 reported by Sakelliou & Ponman (2004). By using the NXB model and

the β-ARF, we simultaneously fit the two spectra, and the fitting results are shown in Fig. 7.8. In this spectral analysis, we adopt the mean values of the CXB model parameters obtained by our blank sky analysis (table 5.2) as Γ_{CXB} and N_{CXB} for the A399/A401 analysis and take account of the CXB spatial fluctuation of 12%.

The temperatures and metallicities in the link region are compared with the average ones of the inner regions of A399 and A401 ($r \lesssim 0.4r_{200}$). Sakelliou & Ponman (2004) reported that the temperature of the inner regions of A399 and A401 are 7.23 keV and 8.47 keV, respectively. These temperatures suggest that the temperature profile is approximately isothermal, and the gas in the link regions has been slightly heated up because of the gas compression associated with the interaction between the two clusters. Sakelliou & Ponman (2004) also reported the metallicities of inner regions as 0.22 for A399 and 0.25 for A401. Thus, the metallicities of the regions A and B are not different from those in their inner regions.

Table 7.3: A399/A401

Sequence number	801020010
Pointing direction	$(l, b) = (164.^\circ45, -39.^\circ13)$
Date	2006/08/19–08/22
Exposure	148.4 ks
N_H	1.05×10^{21} cm^{-2}

7.4 Discussion

In this chapter, we first summarized the metallicity profiles of the sample regular clusters to determine their general trend. The metallicities further than $0.5r_{180}$ could be measured using Suzaku for the first time. Next, we analyzed the A1674 observation. Although A1674 was reported as a rare case wherein the metallicity at its center is clearly lower than those of typical regular clusters, we find it is more likely that there are two clusters at the redshifts of 0.104 and 0.210 in A1674. If there are two clusters, their metallicities agree with the general value of regular clusters. It is important here that we cannot find the cluster whose central metallicity is significantly lower than those of typical regular clusters and that a situation similar to that discussed here in the case of A1674 can occur in other clusters. Finally, we analyzed the link region between A399 and A401 in order to study the ICM in further detail and could more accurately obtain the temperatures and

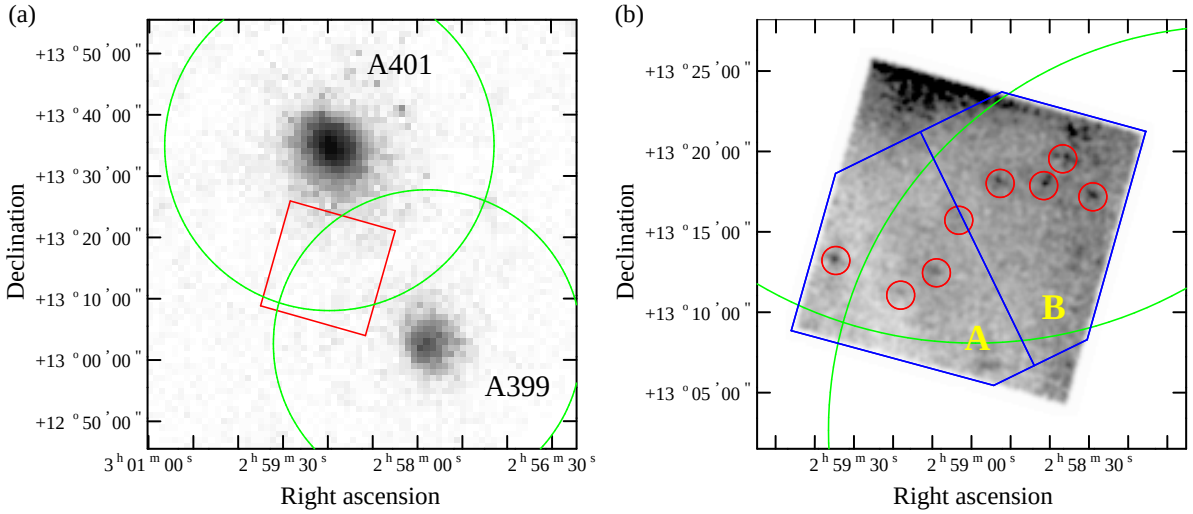

Figure 7.6: (a) ROSAT PSPC image of A399/A401. The virial radii, 2.16 Mpc for A399 and 2.34 Mpc for A401, are shown by green circles. The FOV of the Suzaku XIS shown in Fig. 7.6(b) is indicated by a red square. (b) XIS image of the link region. The virial radii of the clusters are shown by green circles. Regions used for spectral analysis are labeled "A" and "B." Point sources shown by red circles were removed in the spectral analysis.

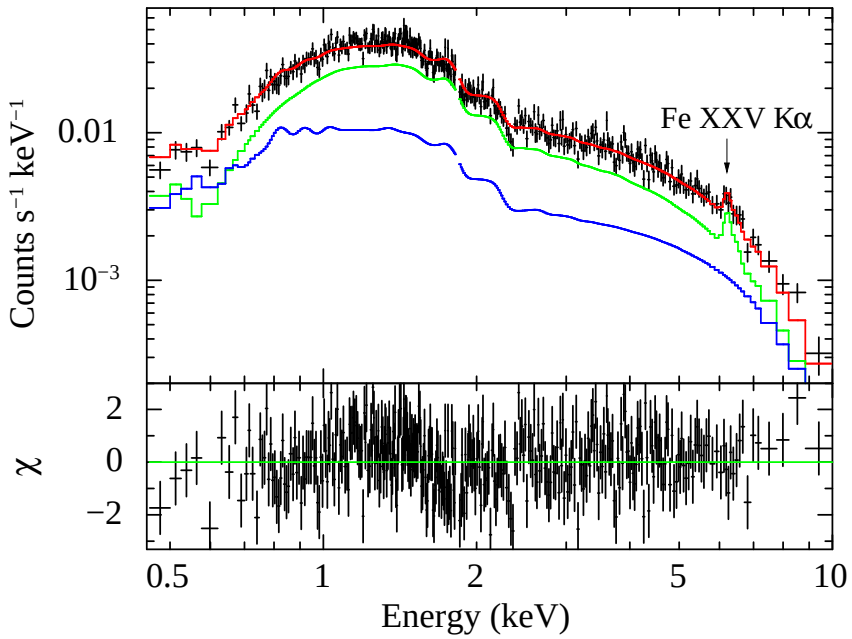

Figure 7.7: FI Spectrum of region A shown in Fig. 7.6(b) (crosses). The result of the fit is shown by the red line. The green line shows the contribution of the ICM, and the blue line shows the sky X-ray background component.

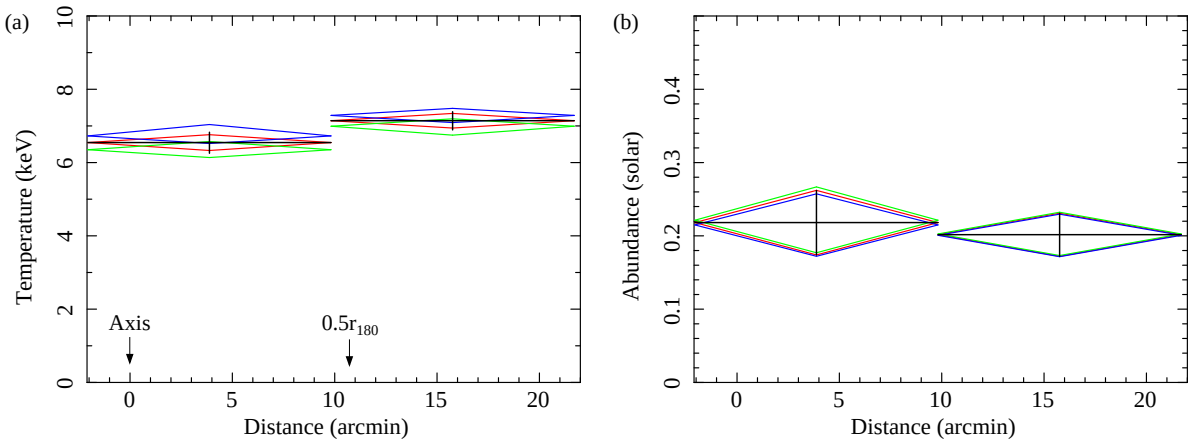

Figure 7.8: (a) Temperature and (b) abundance profiles of A399/A401.

the metallicities even in the outermost region ($r \gtrsim 0.5r_{180}$).

In this section, we individually discuss the metallicity profiles of the sample regular clusters and the results of the A399/A401 observation in subsections 7.4.1 and 7.4.2, respectively. Then, combining the results of the sample regular clusters and the A399/A401 observation, we discuss the metal transportation mechanisms in the outermost region in subsection 7.4.3.

7.4.1 Regular clusters

We replot the metallicity profiles of the sample regular clusters, whose errors are smaller than $0.2Z_{\odot}$, by the black crosses on Fig. 7.9. While the previous observations of metallicity have been limited to $r \lesssim 0.4$–$0.5r_{180}$ (De Grandi et al. 2004; Pratt et al. 2007), we can obtain the metallicities up to $r \sim 0.6$–$0.7r_{180}$ for the sample regular clusters. Our metallicity profiles show that there is a very large scatter in the central regions ($r \lesssim 0.2r_{180}$), and these profiles can be classified broadly into two types: one type has a metallicity excess in the center and the metallicity decreases with the radius; the other type has almost a flat profile. Several authors, e.g., Makishima et al. (2001), suggested that the central metallicity excess can be regarded as a product of the cD galaxy. However, we observed that A1060, which has no cD galaxy, presents the central metallicity excess, and A2218, which has a cD galaxy, presents a flat profile. Therefore, the scatter might be more probably explained by the presence of cooling cores of various strengths. The profiles of the cooling core clusters, i.e., A1795 and A2052, have the central metallicity excesses, while the non-cooling core clusters, i.e., A2218 and A2804, present more flat profiles. However, A1060 and A2804 have the central metallicity excesses, although the cooling cores are

not observed (see Fig. 6.20(c)). This might be because of the fact that these clusters are an initial phase in the formation of a cooling core, as suggested by Sato et al. (2007). This difference between cooling core and non-cooling core clusters was also reported by De Grandi et al. (2004) and Baldi et al. (2007). The mechanism producing the central metallicity excesses should be mainly ram-pressure stripping because the central gas densities of cooling core clusters are very high ($n_g \gtrsim 0.01\,\mathrm{cm}^{-3}$). In fact, recent numerical simulations (Kapferer et al. 2007) have reproduced the central excess of a cooling core cluster by ram-pressure stripping.

On the other hand, in the outer regions ($>0.4r_{180}$), regardless of whether cooling core clusters or non-cooling core clusters, there appears to be a general trend that the metallicity profiles become constant at $\sim 0.2Z_\odot$. This trend suggests that there is generally high-metallicity gas even in the outer region of clusters. It is unlikely that the high metallicity in the outer region is due to a small-scale structure of high metallicity because there is no noticeable X-ray structure in the XIS-FOV, and we excluded the point sources in the spectral analysis. Therefore, the ICM would actually include a large amount of metals.

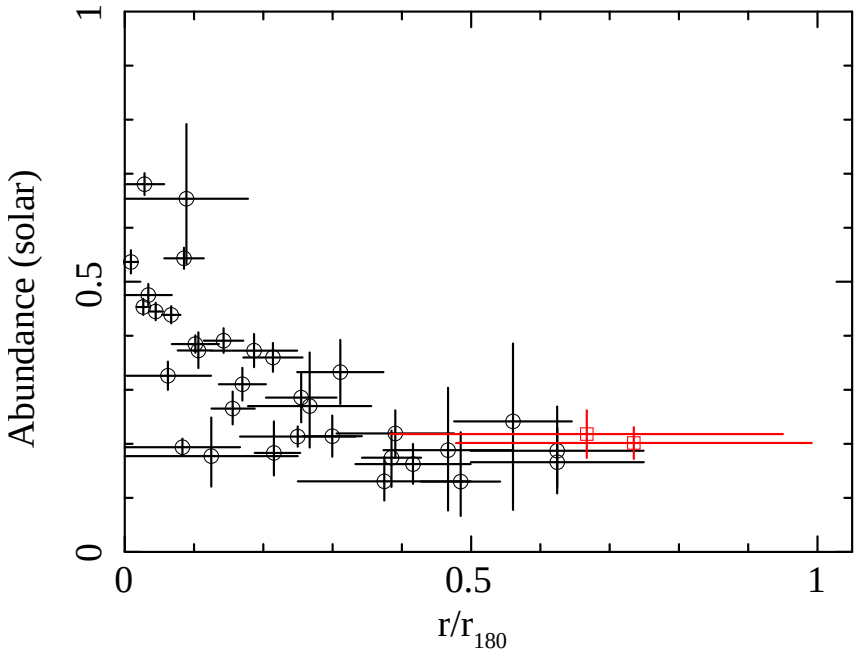

Figure 7.9: Metallicity profiles. Black open circles are the same profiles as shown in Fig. 7.1, but the metallicities whose errors are greater than $0.2Z_\odot$ are excepted. Red open squares show the metallicities of A399/A401 link region as a function of the average clustercentric radius of the two clusters in units of their virial radii.

7.4.2 A399/A401

The red open squares of Fig. 7.9 show the metallicities of the ICM in the link region between A399 and A401 as a function of the average clustercentric radius of the two clusters in units of their virial radii. Although the surface brightness of a cluster rapidly decreases with the radius, we could accurately measure the metallicity in the outermost region ($r \geq 0.5r_{180}$), where the metallicity has not been obtained before.

It is unlikely that the high ICM metallicity in the link region is due to a small-scale structure with high metallicity. This is because of the fact that there is no noticeable X-ray structure in the XIS-FOV, and we excluded the point sources in the spectral analysis. In particular, Sakelliou & Ponman (2004) showed that there is no enhancement of the number density of galaxies in the A399/A401 link region. These facts imply that there is no group of galaxies that possibly ejects more metals than the surrounding region.

The uniformity of the metallicities could be due to a head-on collision of the two clusters; if the two clusters had already passed through each other, metal-rich gas would have been pulled out of their central regions. However, this is not consistent with numerical simulations and previous observations. Numerical simulations showed that while collisionless dark matter and galaxies can pass through another cluster at a cluster collision, collisional ICM cannot. Thus, the ICM is detached from the dark matter and galaxies (Takizawa 1999; Ricker & Sarazin 2001; Poole et al. 2006). However, X-ray observations have shown that the overall X-ray morphology of the two clusters is regular (Fig. 7.6a), which indicates that the ICM is almost in pressure equilibrium in the gravitational potentials formed by the dark matter (Sakelliou & Ponman 2004). Moreover, their X-ray centers are coincident with their central galaxies as is the case of non-merging clusters (Fujita et al. 1996). These considerations indicate that the clusters have not passed through each other. Although both A399 and A401 do not have a prominent cool core, Sakelliou & Ponman (2004) concluded that this is because each cluster has undergone minor mergers, which did not significantly affect the overall structures. Still, we cannot rule out the possibility that the minor mergers might have resulted in some mixing of metals. Therefore, it is important that the findings presented here be also confirmed with regular clusters.

7.4.3 High metallicity of the ICM up to the virial radius

We were able to obtain the metallicities of the ICM in the outermost regions ($\gtrsim 0.5r_{180}$) for the first time. Figure 7.9 shows both of the metallicity profiles of the sample regular clusters and the A399/A401 link region, which indicates that the metallicity profile of A399/A401 is consistent with those of the sample regular clusters. The metallicity profiles

of the sample regular clusters and the A399/A401 link region might imply that the ICM metallicity in a regular cluster is uniform from $r \sim 0.4 r_{180}$ to r_{180}.

If the metallicity is actually high in the outermost regions of the regular clusters, it constrains models of metal transportation from galaxies in the outermost regions. First, ram-pressure striping is unlikely as the main mechanism because the ram pressure is very small and stripping is ineffective at $r \sim r_{180}$. These facts have been confirmed by an analytical method (Fujita & Nagashima 1999) and by numerical simulations (Domainko et al. 2006). Using the β-model parameters obtained by fitting the surface brightness of the sample regular clusters (see table 6.3), the ICM densities at $r = 0.5 r_{180}$ are calculated and are listed in table 7.4. On the other hand, the simply summed ICM density in the link region of A399/A401 is $\sim 2.4 \times 10^{-4}$ cm^{-3} by using the β-model parameters for both clusters obtained by Sakelliou & Ponman (2004). Due to the interaction between the two clusters, the surface brightness in the link region is a factor of two larger than that produced by their simple superposition (Fig. 10 in Sakelliou & Ponman 2004); therefore, the actual ICM density would be $\sqrt{2}$ times higher and be $\sim 3.4 \times 10^{-4}$ cm^{-3}. For a typical galaxy, ram-pressure stripping occurs when the ram pressure exceeds $\sim 2 \times 10^{-11}$ dyne cm^{-2} (Fujita & Nagashima 1999). In the ICM density of the A399/A401 link region, which is the highest in those of all the sample regular clusters at $r = 0.5 r_{180}$, the relative velocity between a galaxy and the ICM must be larger than $\sim$2000 km s^{-1} for effective ram-pressure stripping. Therefore, since this relative velocity is unlikely, ram-pressure stripping would not be effective in the outer region of a cluster.

Galactic outflows are the most promising candidate for the metal transportation mechanism. However, it is not feasible for the elliptical galaxies in the grown-up clusters to pollute the ICM at $r \sim r_{180}$ with metals. For example, an elliptical galaxy with a luminosity of $L_B = 10^{10} L_\odot$ releases an energy of $E_w \sim 10^{60}$ erg through the galactic outflow (David et al. 1991). The distance from the galaxy to which an outflow can reach, d_w, has a relation of

$$E_w \sim (4\pi/3) P d_w^3 \ , \tag{7.1}$$

where P is the pressure of the ICM surrounding the galaxy. Thus,

$$d_w \sim 86 \left(\frac{n_g}{10^{-3} \text{ cm}^{-3}} \right)^{-1/3} \left(\frac{T}{8 \text{ keV}} \right)^{-1/3} \left(\frac{E_w}{10^{60} \text{ erg}} \right)^{1/3} \text{ kpc} \ , \tag{7.2}$$

where n_g is the gas density of the ICM surrounding the galaxy. The distance d_w is much smaller than the virial radius of a cluster ($\sim$ 2 Mpc), which shows that the galactic outflows from elliptical galaxies at $z \sim 0$ alone cannot explain the high metallicity observed at $r \sim r_{180}$.

Therefore, we suggest that powerful outflows from galaxies at high redshifts ($z \sim 2$) act as a mechanism that transfers the metals up to the virial radius. At the redshift of $\sim$2, clusters had not much grown, and most galaxies observed in clusters at $z \sim 0$ had not fallen into the clusters. Such outflows could be produced by active galactic nuclei (AGNs) or intensive starburst activities (Benson et al. 2003; Cen & Ostriker 2006), and they could pollute gas with metals throughout the proto-cluster region (Romeo et al. 2006; Moll et al. 2007). We expect such metal-enriched gas to be captured by the sample clusters recently and observed as the present ICM. In fact, the space density of luminous AGNs and that of starburst galaxies increase from $z = 0$ to $z \sim 2$ (Ueda et al. 2003; Franceschini et al. 2001). By using semi-analytical galaxy formation models, Nagashima et al. (2005) indicated that the metals were ejected into the space outside the cluster ancestors by powerful galactic outflows before the circular velocity of the individual ancestors had grown up to $\sim$600 km s^{-1}.

The metal transportation mechanisms such as ram-pressure stripping and galactic outflows are very complicated; therefore, here we discuss these mechanisms based on numerical simulations. Many groups have recently performed the simulations. We take note of the results reported by Domainko et al. (2006, hereafter D06), Kapferer et al. (2006, hereafter K06), and Kapferer et al. (2007, hereafter K07), who belong to the same group, in order to investigate the distribution and time evolution of metallicity. D06 and K06 reported the simulation results of ram-pressure stripping and galactic outflows, respectively, from $z = 1$ to $z = 0$. Their metallicities at $r = 1\,\mathrm{Mpc} \sim 0.4 r_{180}$ are 1/50–1/100 times lower than those at the centers. The rate at which these metallicities decrease from the center toward the outer region is much larger than that found in our study. Moreover, the metallicities resulting from galactic outflows (K06) are approximately an order of magnitude lower than the observed ones, even in the centers. In contrast, their latest numerical simulations (K07) agree with our results compared to their previous simulations (D06 and K06). The metallicity profiles of non-cooling core clusters simulated by K07 are shown in Fig. 7.10. Although these metallicities in the centers are still higher than the observed ones, e.g., our results for A2218 and Fig. 1 (right) of De Grandi et al. (2004), the profiles of K07 more gradually decrease with the radii with respect to those of D06 and K06. In addition, the profiles of K07 appear to become constant at $Z \sim 0.1$–$0.2 Z_\odot$ at $r \gtrsim 0.8\,\mathrm{Mpc} \sim 0.3 r_{180}$, which is approximately consistent with the general trend that we observed (see Fig. 7.9). This should be because K07 traced the evolution of metallicity from the epoch where the first galaxies formed ($z = 20$) to $z = 0$. In fact, as shown in Figs. 7 and 8 of K07, the large amount of metals are ejected into the ICM before $z = 1$. In particular, whereas the galactic outflows trigger most of the mass

ejected into the ICM in the redshift regime $z > 2$, ram-pressure stripping increases the ejected mass in the redshift interval $z < 2$ in which clusters start to form. Therefore, the high metallicity in the outermost region ($r \gtrsim 0.4 r_{180}$) that we observed might evidence that large amount of metals was ejected at high redshifts ($z \sim 2$) by galactic outflows. However, the metallicity profiles of K07 are unfortunately limited to <1 Mpc in radius; consequently, a more detailed discussion requires the simulations of further outer regions.

Table 7.4: The ICM density at $r = 0.5\, r_{180}$ of the sample regular clusters

Cluster	Density (10^{-4} cm^{-3})	Cluster	Density (10^{-4} cm^{-3})
A1060	0.60	A2801	1.0
A1795	2.4	A2804	1.7
A2052	2.2	A2811	1.9
A2218	2.7		

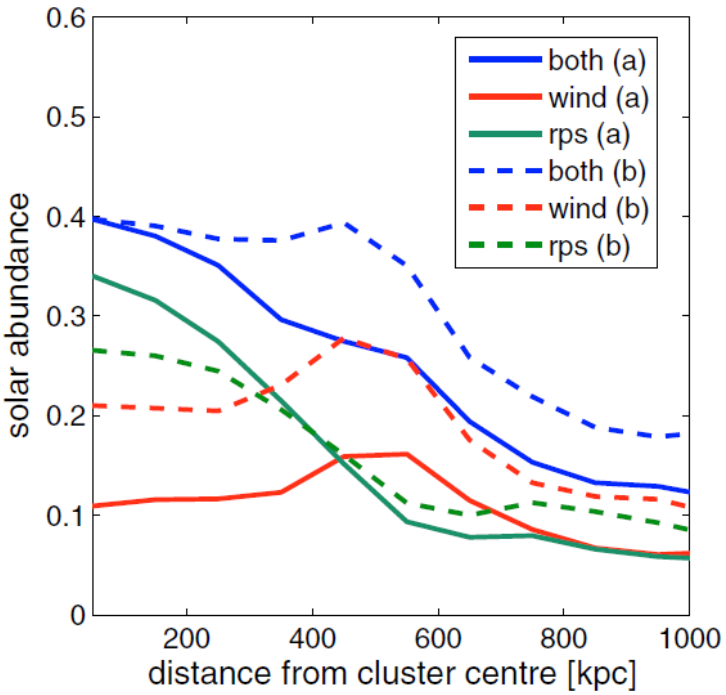

Figure 7.10: Metallicity profiles of the model cluster A that does not have a cooling core. The profiles for the metals ejected by galactic outflows ("wind" in this figure), ram-pressure stripping ("rps"), and both enrichment processes together ("both") are shown for the two enrichment process combinations *a* and *b* (see K07). This figure is taken from Figs. 12 in K07.

Chapter 8

Warm-Hot Intergalactic Medium

Recent numerical simulations of cosmological large-scale structure formation (Cen & Ostriker 1999; Davé et al. 2001) have predicted the existence of a large amount of baryonic matter in the local universe dispersed in the intergalactic medium. This material, comprising about a 1/3rd of the total baryonic matter, is expected to reside in the form of tenuous shock-heated warm-hot ($T = 10^{5-7}$ K) filaments of gas in moderate overdensities (about 10–100 times of the mean hydrogen density) tracing the cosmic web of dark matter (Dolag et al. 2006), called as warm-hot intergalactic medium (WHIM). The WHIM is important as the most promising candidate for the "missing baryons" (Fukugita et al. 1998; Fukugita & Peebles 2004), which was introduced to explain the discrepancy between the baryon density observed in the local universe and that expected from cosmological theories, or that observed at high redshift.

Considering the elemental abundance and the ionization fraction, oxygen is the most promising element to be detected at the expected temperatures of the WHIM. In fact, the emission and absorption lines of highly ionized elements have been searched for in UV and X-ray spectra. In the UV range, O VI absorption features more than 40 systems have been detected in observations with FUSE and HST (e.g., Danforth & Shull 2005). However, the baryon density in the temperature range of $T = 10^{5-6}$ K inferred from those observations is about one order of magnitude lower than that expected for the WHIM. Therefore, most of the missing baryons must reside in a hotter phase at $T = 10^{6-7}$ K, which can be probed with X-rays.

Several emissions have been reported and attributed to the WHIM. Kaastra et al. (2003) and Kaastra (2004a) reported the detection of soft X-ray ($<$0.5 keV) excesses, which include the redshifted O VII and O VIII lines, in the spectra of 7 clusters out of 21 systems measured using the XMM-Newton observatory. Finoguenov et al. (2003) also reported on the detection of O VII and O VIII emission lines in the outskirts of the Coma

cluster. Fujimoto et al. (2004) and Takei et al. (2007b) reported not only emission lines in the spectrum of cluster outskirts, but also absorption lines in the spectrum of a quasar behind the clusters. Fujimoto et al. (2004) observed the emission line and the absorption line of O VIII in the Virgo cluster by using the XMM-Newton observatory. On the other hand, Takei et al. (2007b) detected the emission line of Ne IX and the absorption line of Ne IX and O VIII in the Coma cluster, although the significance of their detection is not high ($\lesssim 3\sigma$ confidence level). However, there are counterarguments against attributing the abovementioned emission/absorption lines to the WHIM associated with clusters. For example, Bonamente et al. (2005) and Bregman & Lloyd-Davies (2006) concluded that some of the emission lines observed by Kaastra et al. (2003) are likely due to the field-to-field variations both of the LHB and MWH. However, both of these two contributions are poorly known, and it is difficult to separate the diffuse extragalactic emission from these bright foreground sources. This is because the CCD instruments cannot clearly distinguish the O lines emitted by the gas associated with the clusters at $z \lesssim 0.05$ from those emitted by the LHB and MWH at $z = 0$.

Therefore, we searched for the O VII line emitted from the WHIM in the link region between A399 and A401 by using the Suzaku XIS. Since these clusters are roughly superposed on the Suzaku field, a high surface brightness of the WHIM emission was expected. However, we detected no significant O VII line and set a tight constraint on its intensity with an upper limit. These results have already been summarized by Fujita et al. (2008). Although Takei et al. (2007a) also searched for the O VII and O VIII lines emitted from the WHIM surrounding A2218 by using the Suzaku XIS, the significant lines were not detected. In summary, the existence of the WHIM in the hotter phase is not yet confirmed.

8.1 Observations

First, we selected the A1413 observation with Suzaku because its net exposure time is the longest in our sample (see table 6.2) and its redshift is relatively high ($z = 0.143$). High redshift is important to distinguish a redshifted O VII line from the unredshifted line emitted from the LHB and MWH. In addition, since a blank sky field, Lockman hole A, was observed just before the observation of A1413, the data would be useful to evaluate the solar component.

We also selected three observations of the Sculptor supercluster, namely, A2801, A2804, and A2811 offset. In the supercluster catalog by Einasto et al. (2001), there are only three rich and distant ($z > 0.1$) superclusters, viz., Sculptor, Draco, and Grus,

which have more than ten clusters and more than two X-ray emitting clusters. Among these three clusters, since Sculptor is the richest one, it should have the most massive WHIM.

Details about the observations of A1413 and the Sculptor supercluster are listed in table 6.2, and the details about the observation of Lockman hole A are listed in 5.1.

8.2 Spectral analysis

8.2.1 Contamination of O I line from the Earth atmosphere

The O VII line from the WHIM surrounding A1413 is redshifted from 574 keV to 502 keV at $z = 0.143$. Although this redshifted O VII line should be distinguished from the unredshifted O VII line, it is difficult to distinguish it from the fluorescent O I line (525 eV), which is emitted from the Earth atmosphere excited by the solar X-rays or charged particles. Figure 8.1 shows the solar X-ray and proton fluxes observed by GOES (Geostationary Operational Environmental Satellites)[1] during the Lockman hole A and the A1413 observations. Since this figure shows that the solar activity is comparable between the two observations, the contributions of the O I line to the spectrum of Lockman hole A should be similar to those to the A1413 spectrum. Therefore, we employ the observation of Lockman hole A to evaluate the O I line contamination.

However, there are several faint clusters in the XIS FOV of the field of Lockman hole A and its nearby field, as shown in Fig. 8.2(a) by the magenta circles. These clusters were searched by using the NED. If the WHIM is surrounding these clusters, the emission from the WHIM might be confused with the atmospheric O I line. In particular, RX-J105340.4+572349, which is a cluster shown in Fig. 8.2(a), has high possibilities of influencing to this analysis because of its redshift, 0.205. Therefore, we extract the spectra from a region that is far away from this cluster, as shown in Fig. 8.2(b).

We apply two screening criteria to extract the spectra: criterion 1 and criterion 2. Criterion 1 is the same as that was applied to the blank sky field and the clusters described in subsection 5.2.2. Criterion 2, which is stricter than criterion 1, is ELV $> 20^\circ$ and DYE_ELV $> 30^\circ$. Its other parameters such as grade selection (step 1 in subsection 5.2.2) and orbit filter (see subsection 4.2.3) are the same as those of criterion 1. The net exposure times of the Lockman hole A for the spectra extracted using criteria 1 and 2 are 73.0 ks and 55.1 ks, respectively.

We use the BI CCD (XIS1), which has higher sensitivity in a low energy band ($\lesssim$2 keV)

[1] http://www.ngdc.noaa.gov/stp/GOES/goes.html

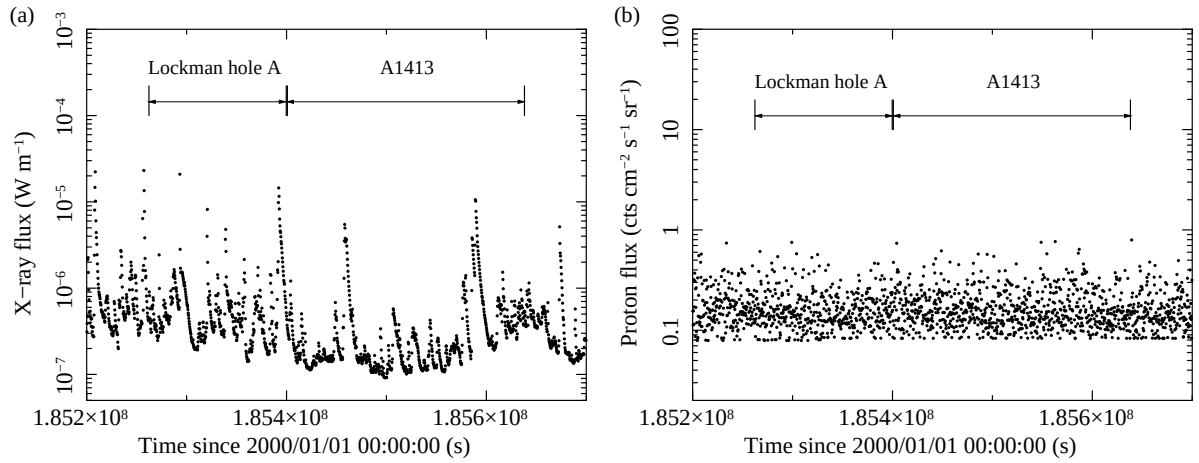

Figure 8.1: Fluxes of (a) the solar X-rays and (b) the solar protons observed with GOES. (b) shows the count rate of protons having energies greater than 10 MeV. The arrowed lines show the epochs of the Lockman hole A and the A1413 observations.

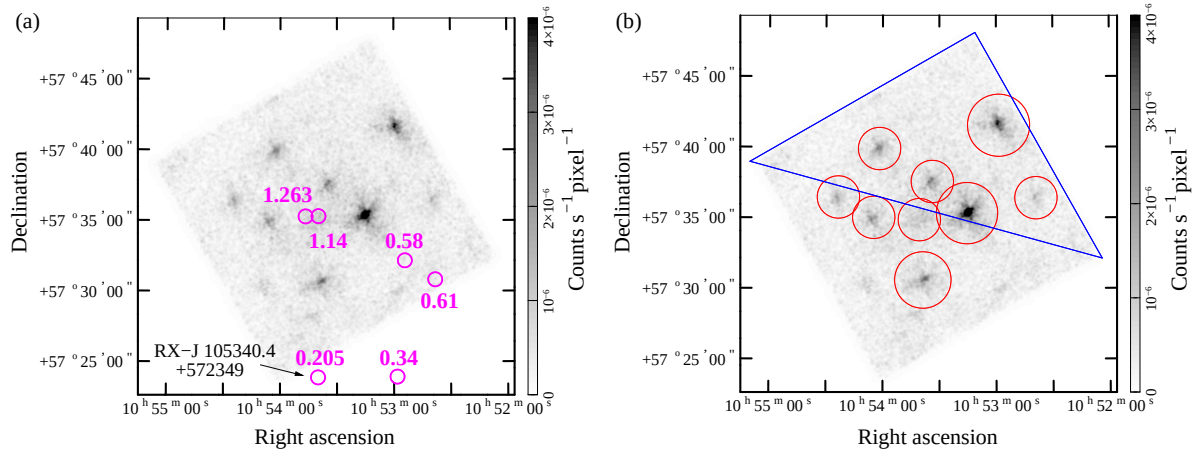

Figure 8.2: Same as Fig. 5.3(d), but (a) shows the faint clusters by the magenta circles, and (b) shows the region where the spectra were extracted by the blue triangle. The magenta numbers in (a) are the redshifts of the faint clusters. The red circles in (b) show the point sources.

than the FI CCDs (XIS0, 2, and 3). Figure 8.3 shows the BI spectra, which are fitted in the 0.25–5.5 keV band with a Gaussian component corresponding to the O I line around 525 eV and the sky X-ray background component (LHB, MWH, and CXB). We follow a fitting procedure similar to that used for the blank sky analysis (section 5.2), but the photon index of the CXB is set equal to the best-fit value that we obtained in the blank sky analysis, 1.468 (see Fig. 5.7). While the additional width of the Gaussian component is set equal to zero, its line-center energy and normalization are free. The best-fit model is shown in Fig. 8.3, and its parameters are summarized in table 8.1. The O I line is

significantly detected in the spectrum extracted using criteria-1, while it is not detected in the spectrum extracted using criteria-2. Therefore, we adopt criteria-2 to the spectral analysis of the A1413 and the Sculptor observations.

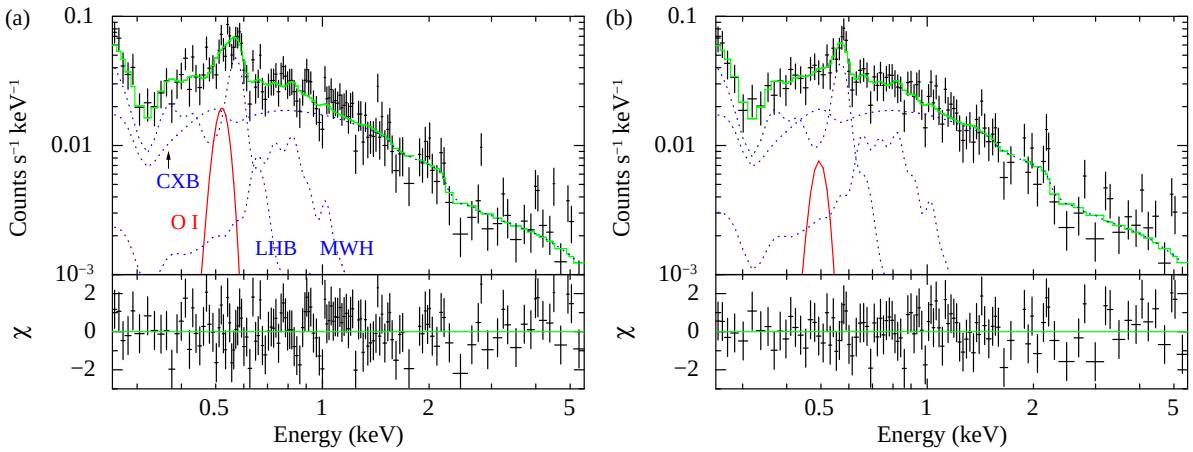

Figure 8.3: BI spectra of Lockman hole A and the best-fit model. The spectra of (a) and (b) were extracted using criteria 1 and 2, respectively. The red lines show the Gaussian component corresponding to the O I line, and the blue dotted lines show the LHB, MWH, and CXB. The green lines show the sum of these components.

Table 8.1: Best-fit parameters of Lockman hole A using a model for the O I line

Parameter	Criteria-1	Criteria-2
LHB kT (keV)	$0.1160^{+0.0083}_{-0.0059}$	$0.116^{+0.016}_{-0.012}$
MWH kT (keV)	$0.40^{+0.19}_{-0.08}$	$0.35^{+0.18}_{-0.04}$
CXB Photon index	1.468 (fix)	1.468 (fix)
O I E (eV)	519^{+15}_{-19}	494 (<561)
O I I^*	$1.58^{+0.73}_{-0.61} \times 10^{-7}$	$0.57\ (<1.1) \times 10^{-7}$
χ^2/dof	142.6/124	87.4/95

Errors are 90 % confidence level.

* In units of photons cm^{-2} s^{-1} arcmin^{-2}.

8.2.2 A1413

We extract a BI spectrum by applying criteria-2 from the outermost region where the distance from the A1413 center is greater than 10′. The point sources shown in Fig. 6.3(a) are excluded from the spectrum, while the calibration source regions are included. The

spectrum is fitted in the 0.25–5.5 keV band with a single thermal model (APEC), a Gaussian component corresponding to the expected redshifted O VII line around 500 eV, and the sky X-ray background component. The thermal component is required to precisely estimate the contribution of the ICM. We assume that its temperature, metallicity, and redshift are 3.86 keV, $0.41 Z_{\odot}$, and 0.143, respectively, obtained from the fitting results of the annular region between $10'$ and $15'$ from the center (subsection 6.3.2). The normalization of the thermal component is free in the fit. While the additional width of the Gaussian component is set equal to zero, its line-center energy and normalization are free. The sky X-ray background is treated in the same manner as that in the above subsection, but the photon index of the CXB is fixed to 1.489, which is the best-fit value measured in the outermost region ($r > 15'$) of A1413 (subsection 6.3.2). The thermal component is calculated using the β-ARF, and the Gaussian component and the sky X-ray background are calculated using the uniform ARF. (The β-ARF and the uniform ARF are described in subsection 6.2.3.)

The spectrum and the best-fit model with and without the Gaussian component are shown in Fig. 8.4(b) and (a), respectively. The best-fit values for the models with/without the Gaussian component are summarized in table 8.2. The residuals present around 500 eV in Fig. 8.4(a) disappear in Fig. 8.4(b), suggesting the existence of an emission line at $\sim$500 eV with a 99.86% confidence level of the F-test.

Table 8.2: Best-fit parameters of A1413 obtained using a model with/without the redshifterd O VII line

Parameter	Without O VII line	With O VII line
LHB kT (keV)	$0.1236^{+0.0075}_{-0.0062}$	$0.1213^{+0.0063}_{-0.0068}$
MWH kT (keV)	$0.33^{+0.14}_{-0.08}$	$0.32^{+0.14}_{-0.07}$
CXB Photon index	1.489 (fix)	1.489 (fix)
O VII E (eV)	-	505^{+17}_{-15}
O VII I^*	-	$1.04^{+0.51}_{-0.45} \times 10^{-7}$
χ^2/dof	263.40/258	250.19/256

Errors are 90 % confidence level.

* In units of photons cm^{-2} s^{-1} arcmin^{-2}.

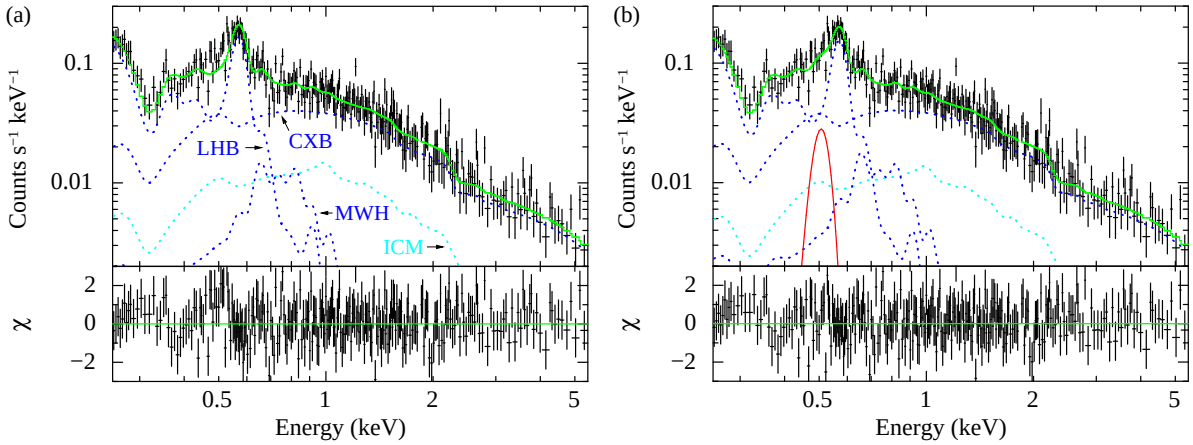

Figure 8.4: BI spectra of A1413 and the best-fit models (a) without and (b) with the redshifted O VII line. The spectra were extracted from the A1413 outermost region where the distance from the center is greater than 10′. The red line shows the Gaussian component corresponding to the redshifted O VII line. The blue and cyan dotted lines show the sky X-ray background and the ICM component, respectively. The green lines show the sum of these components.

8.2.3 Sculptor supercluster

We extract the BI spectra by applying criteria-2 from the blank sky field in the Sculptor observations. In this case, the blank sky field implies the sky regions where the ICM is not significantly detected, as shown in Fig. 6.11. First, we fit the spectra with only the sky X-ray background component. The energy range of the A2801 spectrum is the 0.25–5.5 keV band because the calibration source regions have not been excluded. In contrast, the energy range of the spectra of A2804 and A2811 offset is the 0.25–8.0 keV band because the calibration source regions have been excluded. The model parameters of this component are set to have the same values for each spectrum in the fit. The spectra and the models are shown in Fig. 8.5(a), and the best-fit parameters are summarized in the "model 1" column of table 8.3. Next, we fit the spectra with the sum of the sky X-ray background component and a Gaussian component. The best-fit parameters are summarized in the "model 2" column of table 8.3. The center energy of the Gaussian component is significantly lower than the expected value (518.05 eV) at a redshift of 0.108. Therefore, we fix the center energy to 518.05 eV and refit the spectra with the same model. The best-fit model is shown in Fig. 8.5(b), and the best-fit parameters are summarized in the "model 3" column of table 8.3. We cannot significantly detect the redshifted O VII line emitted from the WHIM and set a tight constraint on the intensity with an upper limit of 5.2×10^{-8} photons cm^{-2} s^{-1} arcmin^{-2} for the surface brightness of O VII.

Table 8.3: Best-fit parameters of the Sculpter observations

Parameter	Model 1	Model 2	Model 3
LHB kT (keV)	$0.120^{+0.014}_{-0.010}$	$0.125^{+0.022}_{-0.013}$	$0.120^{+0.013}_{-0.010}$
MWH kT (keV)	$0.336^{+0.078}_{-0.049}$	$0.34^{+0.20}_{-0.05}$	$0.335^{+0.077}_{-0.048}$
CXB Photon index	1.413 (fix)	1.413 (fix)	1.413 (fix)
O VII E (eV)	-	450 (<490)	518.05 (fix)
O VII I^*	-	6.4 (<15.6) $\times 10^{-8}$	0.4 (<5.2) $\times 10^{-8}$
χ^2/dof	159.54/164	157.28/162	159.52/163

Errors are 90 % confidence level.

* In units of photons cm^{-2} s^{-1} arcmin^{-2}.

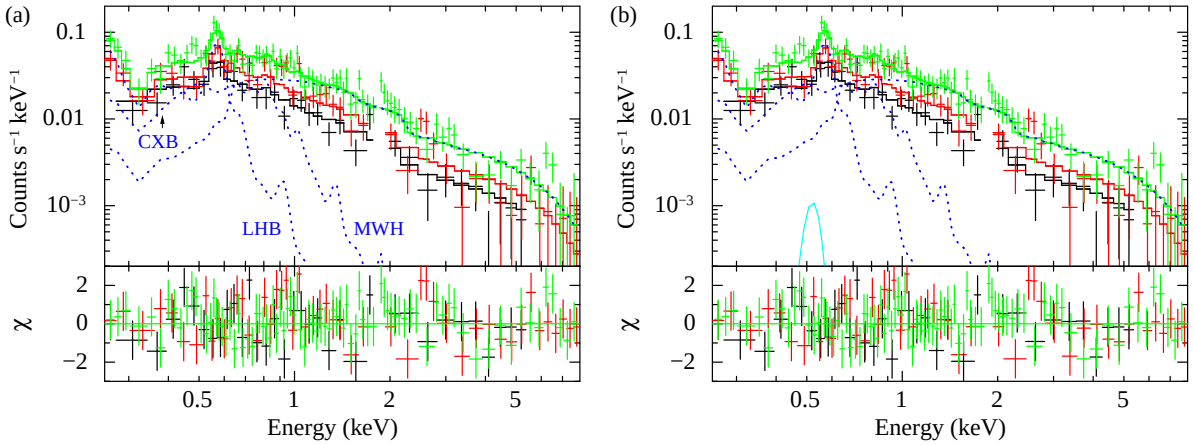

Figure 8.5: BI spectra and the best-fit models of A2801 (black), A2804 (red), and A2811 offset (green). The spectra of (a) were fitted with the sky X-ray background component, while the spectra of (b) were fitted with the sky X-ray background component and a Gaussian component representing the redshifted O VII line. The center energy of the line was fixed to 518.05 eV in the fit. The cyan line and blue dotted lines show the O VII line and the sky X-ray background (LHB, MWH, and CXB) for the A2811 offset observation, respectively.

8.3 Discussion

We searched for the redshifted O VII line emitted from the WHIM around A1413 and the Sculptor clusters, A2801, A2804, and A2811. In the results obtained, while the emission line around 500 eV for the Sculptor clusters is not detected, the line for A1413 is significantly detected. We calculate the confidence contours for the line-center energy and its normalization for the A1413 observation in Fig. 8.6. The center energy of this line is 505^{+17}_{-15} eV, which agrees well with the expected value for the redshifted O VII (502 eV) from the WHIM surrounding A1413. In addition, the significance of its detection is higher than 99.73% (3σ confidence level). Note that the line is distinguished from the unredshifted O VII line emitted from the LHB and MWH. The contribution of the O I line from the Earth atmosphere is negligible, assuming that criteria-2 removes its contamination.

However, the XIS spectra in the energy band of $\lesssim$1 keV are sometimes affected by the solar-wind charge-exchange X-ray (SCX) emission from the Earth's magnetosheath (Fujimoto et al. 2007). Since it is difficult to eliminate the SCX emission by screening with the elevation angles, we evaluate its effects by using the solar-wind proton flux. Figure 8.7 shows the proton flux calculated using the level-2 ACE (Advanced Composition Explorer) SWEPAM (Solar Wind Electron, Proton, and Alpha Monitor) data[2] during the observations of the Sculptor clusters. As shown in this figure, the proton flux was enhanced before and after the observation of A2811 offset, and its level was comparable with or higher than that when Fujimoto et al. (2007) and Fujita et al. (2008) detected the SCX emission. In addition, when we set the center energy of the Gaussian component to be free in the fit, its best-fit value was 450 eV (model 2 in table 8.3). This value is approximately consistent with the C VI $n = 4$ to 1 transition line (Lyγ) (459 eV), which was also detected by Fujimoto et al. (2007). Thus, the observations of the Sculptor clusters must have been affected by the SCX emission.

We also evaluate the solar-wind proton flux during the observations of Lockman hole A and A1413. The ACE SWEPAM data show that the proton flux during the observation of Lockman hole A was $\sim 1.8 \times 10^8$ cm^{-2} s^{-1} and was stable, which is about 35% of the level when the SCX emission was observed (Fujimoto et al. 2007; Fujita et al. 2008). However, the ACE data during the A1413 observation were unfortunately not available. Since the proton flux was stable during the observation of Lockman hole A, we assume that it was approximately constant between the Lockman hole A and A1413 observations. Under this assumption, the positive detection of the redshifted O VII line in A1413 is justified (red diamond in Fig. 8.8). In contrast, if the proton flux increased during the

[2]http://swepam.lanl.gov/data/raw/index.cgi/swepam_dswi_level2

A1413 observation, the contamination of the SCX emission cannot be ruled out. In this case, our results indicate that the upper limit of the O VII line is 1.6×10^{-7} photons cm^{-2} s^{-1} arcmin^{-2} (black arrow in Fig. 8.8).

In this paragraph, we compare our results of the O VII line intensities with those reported in other works. Figure 8.8 shows this comparison. Kaastra et al. (2003) and Finoguenov et al. (2003) reported the positive detections of O VII line around clusters based on XMM-Newton observations. Kaastra et al. (2003) analyzed a sample of 14 clusters and detected significant O VII line in three clusters, Sérsic 159-03, MKW 3s, and A2052. The line intensities shown in Fig. 8.8 were calculated using the temperature and emission measure in their table 7 and the metal abundance from tables 4 and 5 of Tamura et al. (2004). Finoguenov et al. (2003) detected the O VII line in the outskirts of the Coma cluster, particularly in the Coma-11 field. Takei et al. (2007a) and Fujita et al. (2008) obtained the upper limit for the O VII line intensity from the observations of A2218 and the A399/A401 link region with Suzaku, respectively. Figure 8.8 also shows the intensity of the O VII line of the sky X-ray background. This O VII line is mainly emitted from the LHB. The line intensity observed using a microcalorimeter onboard a sounding rocket of McCammon et al. (2002), the one measured from the compiled XMM-Newton data by Lumb et al. (2002), and the one measured from the A2218 offset-A observation with Suzaku by Takei et al. (2007a) are shown. The intensities of the O VII line that were reported as the WHIM emission based on the XMM-Newton observations are similar to, or higher than, those of the sky X-ray background. In contrast, the O VII line intensities observed for Suzaku, A2218, the A399/A401 link region, A1413, and the Sculptor clusters are about six times lower than those of the sky X-ray background. The line intensity observed in the A1413 vicinity is also lower than those observed using XMM-Newton and agrees with those in the A2218 vicinity and the A399/A401 link region. In addition, The upper limit of the intensity in the vicinity of Sculptor clusters is tighter than those obtained in the A2218 vicinity and the A399/A401 link region.

Here, we evaluate the hydrogen density of the WHIM around A1413 and the Sculptor clusters based on our results. Under assumption that the redshifted O VII line is produced in a cloud with a uniform density and temperature of $T = 2 \times 10^6$ K, the hydrogen density at a redshift z can be expressed by

$$n_H = 8.25 \times 10^{-5} \text{ cm}^{-3} \ (1+z)^{3/2} \left(\frac{I}{1 \times 10^{-7} \text{ ph cm}^{-2} \text{ s}^{-1}} \right)^{1/2} \times \left(\frac{Z}{0.1 Z_\odot} \right)^{-1/2} \left(\frac{L}{1 \text{ Mpc}} \right)^{-1/2}, \quad (8.1)$$

where L is the path length (Takei et al. 2007a). From eq. (8.1), under assumption that

the metallicity of WHIM is $Z = 0.1Z_{\odot}$, the density of the WHIM surrounding A1413 ($z = 0.143$) is $n_H = 7.3^{+5.1}_{-4.8} \times 10^{-5}$ cm^{-3} for $L = 2$ Mpc. The value of L is the typical depth of warm gas in a cosmic filament (Colberg et al. 2005). On the other hand, the density of the WHIM in the vicinity of Sculptor clusters ($z = 0.108$) is $n_H < 4.9 \times 10^{-5}$ cm^{-3} for $Z = 0.1Z_{\odot}$ and $L = 2$ Mpc. We also calculate the overdensity of this cloud, $\delta \equiv n_H/\bar{n}_H$, where $\bar{n}_H = X\Omega_{\rm b}\rho_c(1+z)^3/m_{\rm p} = 1.77 \times 10^{-7}(1+z)^3$ cm^{-3} is the mean hydrogen density in the universe at a redshift z (Takei et al. 2007a). $X = 0.71$ denotes the hydrogen-to-baryon mass ratio, $\Omega_{\rm b} = 0.0457$ is the baryon density of the universe, $\rho_c = 9.21 \times 10^{-30}$ g cm^{-3} is the critical density of the universe, and $m_{\rm p} = 1.67 \times 10^{-24}$ g is the proton mass. The overdensities δ of the cloud surrounding A1413 and in the vicinity of Sculptor clusters are 275^{+193}_{-181} (assuming no contamination of the SCX emission) and $<$204, respectively. These densities are much higher than the typical density of WHIM, $\delta \sim 10$. It might be the case that the high-density part of the WHIM exists near clusters as predicted by the numerical simulations in the CDM model (e.g., Cen & Ostriker 1999; Davé et al. 2001; Dolag et al. 2006).

In previous observations with Suzaku (e.g., Takei et al. 2007a; Fujita et al. 2008), the search for the emission from the WHIM was restricted to the inner regions of clusters ($r \lesssim 0.6r_{180}$). However, our results imply that the surface brightness of the O VII line emitted from the WHIM is comparable with or lower than that emitted from the sky X-ray background, i.e., LHB. Therefore, we recommend that the outer region ($r \gtrsim 0.6r_{180}$), where the surface brightness of the ICM is sufficiently low, be observed in order to detect the WHIM emission.

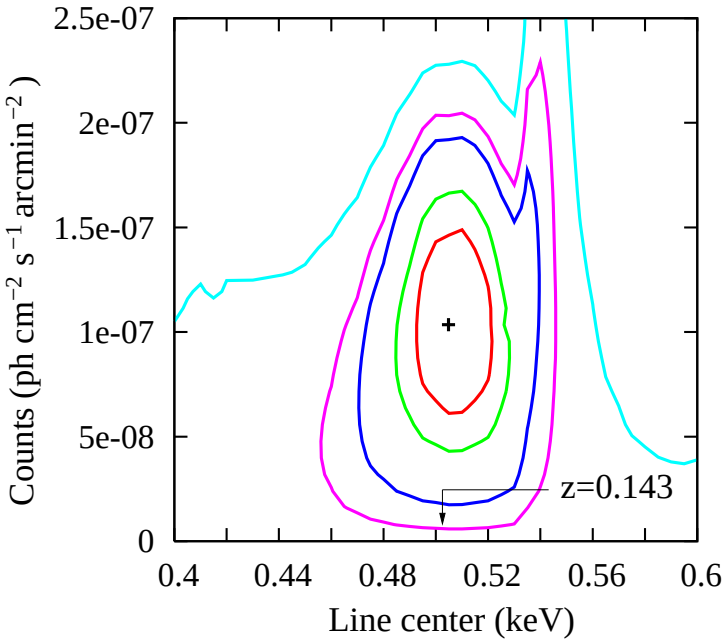

Figure 8.6: Confidence contours for the line center and photon counts of the Gaussian component. The lines show 68.3%, 90.0%, 95.4%, 99.0%, 99.73%, and 99.99% confidence regions for two interesting parameters, and the black cross shows the best-fit values. The arrow indicates a energy of 502 eV, which corresponds to the redshifted O VII line at $z = 0.143$.

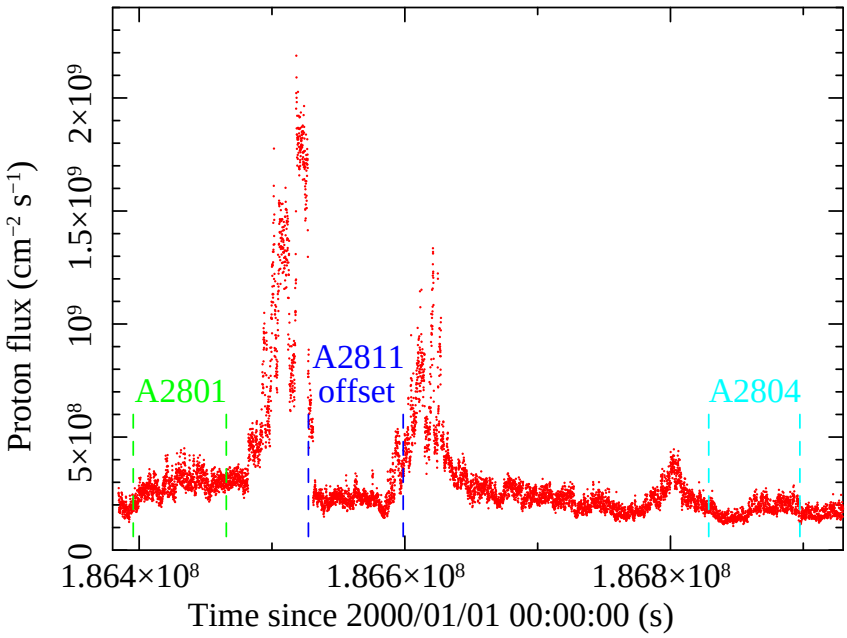

Figure 8.7: Solar-wind proton flux during the observations of the Sculptor clusters, A2801, A2804, and A2811. The flux was calculated using the level-2 ACE SWEPAM data. Each bin of the ACE data was shifted in time to correct for the travel time of the solar wind from ACE to the Earth (typically ∼2700 s). The green, blue, and cyan dashed lines show the epoch of the A2801, A2811 offset, and A2804 observations with Suzaku, respectively.

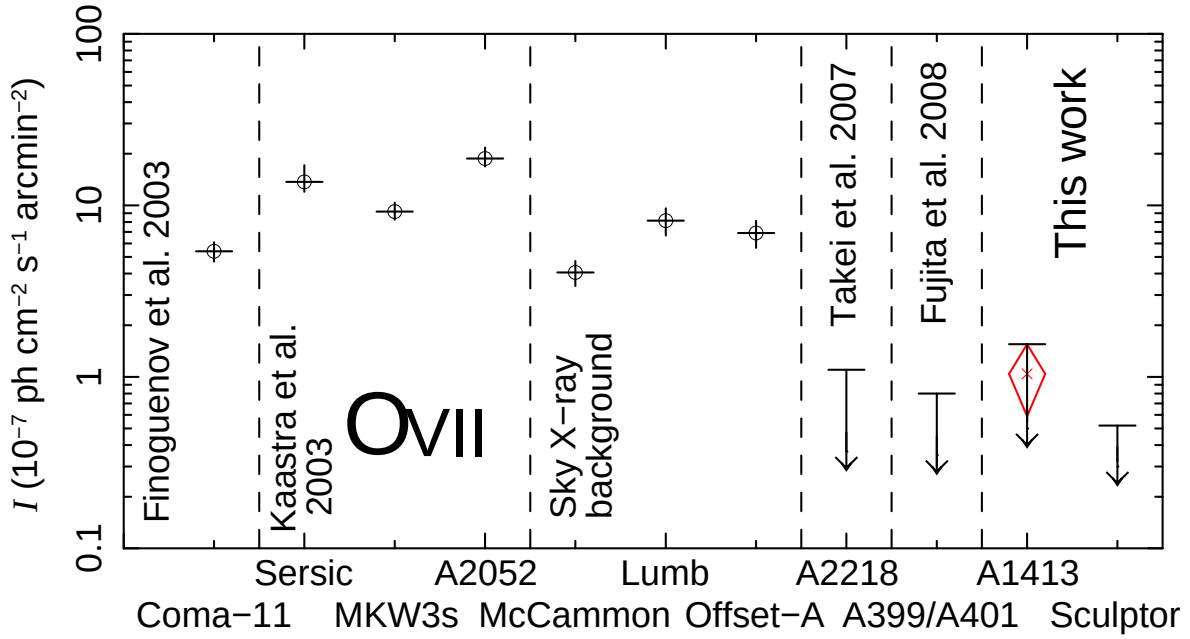

Figure 8.8: Comparison of O VII surface brightness. From left to right, those in the Coma-11 field (Finoguenov et al. 2003), Sérsic 159-03, MKW 3s, A2052 (Kaastra et al. 2003), the sky X-ray background of McCammon et al. (2002), Lumb et al. (2002), the A2218 offset observation (Takei et al. 2007a), the upper limits in the A2218 outskirts (Takei et al. 2007a) and the A399/A401 link region (Fujita et al. 2008), the A1413 outermost region, and the vicinity of Sculptor clusters (this work). If there is no contamination of the SCX emission, the O VII line for A1413 will be significantly detected (red diamond). In contrast, if there is some contamination of the SCX emission, we will obtain the upper limit of the O VII line intensity for A1413 (black arrow). The data in this figure are the same as those in Fig. 7(left) of Takei et al. (2007a), except for the results of Fujita et al. (2008) and this work.

Chapter 9

Summary

9.1 Background for the Suzaku XIS

Proper treatment of the background observed in the Suzaku XIS is very important for the spectral and spatial analysis of faint extended sources. The background of the XIS consists of three components: (1) the NXB, (2) the solar component, and (3) the sky X-ray background. Among these components, the solar component varies with time, and hence, is the most difficult to estimate. However, we can minimize it by using the orbital and altitude data of Suzaku and the solar wind data. On the other hand, since one of the advantages of the XIS is its low and extremely stable NXB, in order to make the best use of this advantage, it is important to correctly subtract the NXB from the spectra of on-source observations. It is also important to estimate the spectrum of the sky X-ray background and its spatial fluctuation for the sources extending over the XIS-FOV. Therefore, we investigated the NXB and the sky X-ray background.

9.1.1 NXB

We constructed the NXB database by collecting the XIS events of the NTE. The NXB database, including EHK files and two software tools, *mk_corsorted_spec_v1.0.pl* and *mk_corweighted_bgd_v1.1.pl*, is now accessible via the Suzaku web page at ISAS/JAXA and GSFC/NASA. Since the XIS NXB depends on the cut-off-rigidity in orbit or on the PIN-UD count rate, we need to equalize the distributions of these parameters for the on-source observations and for the NTE observation so that we can actually subtract the NXB. We have examined two modeling parameters for the NXB, the *COR2* and the PIN-UD. There is a large deviation from the expected value of the NXB count rate for both models when Suzaku passes through high-altitude and high-latitude regions. With the

exception of these instances, the NXB reproducibilities show a significant improvement. Similarly, excluding the data collected in September 2005, the XIS2 reproducibility also shows improvement. Our results show that the NXB model sorted by the PIN-UD has better reproducibility than that sorted by the *COR2*. Using the NXB data in exposure bins of 5 ks each, the reproducibility obtained with the PIN-UD model is 4.55%–5.63% for each XIS NXB in the 1–7 keV band and 2.79%–4.36% for each XIS NXB in the 5–12 keV band.

9.1.2 Sky X-ray background

We analyzed the spectra of six blank sky observations with the Suzaku XIS excluding the point sources whose fluxes in the 0.7–8 keV band are higher than 2.5×10^{-14} erg cm^{-2} s^{-1}. Since the blank sky spectra contain three components — LHB, MWH, and CXB — we fitted the spectra with a model for the sum of two thermal models for the LHB and MWH components and a single power-law model for the CXB components. We find that the blank sky spectra in the 0.25–10 keV band can be accurately reproduced by the model. The mean temperatures for the LHB and MWH are 0.1121 ± 0.0026 keV and 0.270 ± 0.019 keV (1σ statistical errors), respectively, which are consistent with those observed by ROSAT PSPC and XMM-Newton EPIC. On the other hand, the mean photon index for the CXB is 1.451 ± 0.034 (1σ statistical error). The mean flux in the 2–10 keV band is $(4.37 \pm 0.14) \times 10^{-15}$ erg cm^{-2} s^{-1} arcmin^{-2} (1σ statistical error), and its spatial fluctuation is $12.0 \pm 2.4\%$ (1σ statistical error) of the mean flux. We also analytically calculated the spatial fluctuation by considering the flux for point source elimination and the mean effective beam size. We confirmed that the observed fluctuation value is consistent with the calculated value of 13.3%.

9.2 Galaxy clusters

In the CDM model, the structure of the universe grows hierarchically by gravitational attraction, with small objects merging in a continuous hierarchy to form more and more massive objects. Therefore, the temperature and density of the ICM are important to study the gravitational processes responsible for the large-scale structure formation of the universe and non-gravitational-energy input into the ICM. In addition, the metallicity of the ICM is the key to understanding the formation history of stars in clusters and the mechanisms that transfer metals from galaxies to the ICM. The CDM model also predicts the existence of the WHIM. The confirmation of the existence of the WHIM is considered to be the solution to the "missing baryons problem."

Since the Suzaku XIS has a large effective area and a low and extremely stable NXB, it is suitable for the analysis of faint and diffuse sources. Therefore, we have analyzed the Suzaku XIS data to measure the temperature and the metallicity up to the outermost region of the clusters and to search for the WHIM.

9.2.1 Temperature and surface brightness profiles of regular clusters

We analyzed the Suzaku data of eight regular clusters — A1060, A1413, A1795, A2052, A2218, A2801, A2804, and A2811. In this spectral analysis, we employed the NXB spectra modeled with the PIN-UD by using our developed method and considered the spatial fluctuation of the CXB, which we obtained from the XIS observations of the blank sky. Although temperature profiles were measured with the previous observations, i.e., ASCA (Markevitch et al. 1998), BeppoSAX (De Grandi & Molendi 2002), Chandra (Vikhlinin et al. 2005), and XMM-Newton (Pratt et al. 2007), their profiles were unfortunately limited to $\sim 0.6 r_{180}$. Therefore, we have investigated the temperature and surface brightness profiles of the regular cluster samples up to the outermost regions. Our main results can be stated as follows:

- We were able to measure the temperature and surface brightness profiles of the regular cluster samples up to the virial radii.
- The scaled temperature and the scaled emission measure profiles show the similarity in the radial range from $0.15 r_{180}$ to the virial radius.
- The temperatures significantly decline with the radius in the outer region ($r \gtrsim 0.15 r_{180}$), and their general trend shows a polytropic index of 1.190 ± 0.034.
- The scaled temperature profiles are consistent with those of the previous observations, i.e., ASCA (Markevitch et al. 1998), BeppoSAX (De Grandi & Molendi 2002), Chandra (Vikhlinin et al. 2005), and XMM-Newton (Pratt et al. 2007).
- We obtained a M–T relation by using the best-fit parameters of the polytropic model ($T_0 = 1.316$, $\gamma = 1.190$) and the β-model ($\beta = 0.71$, $r_c = 0.13 r_{180}$). Our M–T relation agrees well with those of other studies, and we find that the total gravitational mass can be estimated from only T_X.
- The scaled temperature profiles we observed are consistent with those of the recent numerical simulations in the CDM model (Borgani et al. 2004) from $0.15 r_{180}$ to the virial radius.

The scaling relations for the ICM temperature and density and the consistency between the temperature profiles of our observations and the numerical simulations indicate that the ICM is dominantly heated by gravitational processes of cluster formation.

9.2.2 Metallicity of the ICM up to the virial radius

We measured the metallicities of A1674 and the link region between A399 and A401 in addition to the regular cluster samples. The Suzaku XIS can obtain the metallicity with a high degree of accuracy even in the outermost region ($r \gtrsim 0.5r_{180}$). However, the metallicities of the previous observations (De Grandi et al. 2004; Baldi et al. 2007) have been limited to the inner region ($r \lesssim 0.4$–$0.5r_{180}$), and the mechanisms that transfer metals from the cluster galaxies into the ICM are still unclear. Therefore, we constrain the mechanisms that transfer metals from galaxies to the ICM comparing the observed metallicities with the ones of the recent numerical simulations. Our main results can be stated as follows:

- We were able to measure the metallicity profiles of the regular cluster samples up to $\sim 0.7r_{180}$. While there is a large scatter of the metallicities in the center, the ones in the outer region ($r \gtrsim 0.4r_{180}$) are approximately constant at $0.2Z_{\odot}$.

- Although A1674 was reported as a rare case in which the metallicity at its center was clearly lower than those of the typical regular clusters, we find that it is more likely that there are two clusters at redshifts of 0.104 and 0.210 in the A1674 region. If there are two clusters, the metallicities of these clusters agree with the general value of the regular clusters.

- The metallicity of the A399/A401 link region is $\sim 0.2Z_{\odot}$, which is comparable to the metallicity in the inner regions of the clusters. This suggests that the metallicity is uniform within the virial radii.

- While the constantly high metallicities we observed in the outermost regions ($r \gtrsim 0.4r_{180}$) cannot be reproduced by simulations in which the metal enrichment process is traced from $z = 1$ to $z = 0$ (Domainko et al. 2006; Kapferer et al. 2006), our metallicities can be reasonably reproduced by the latest simulations in which the process is traced from $z = 20$ and 0 (Kapferer et al. 2007). This suggests that the metals were transferred before the clusters formed ($z \sim 2$), and that the proto-cluster region was heavily polluted with the metals. Since the density of the ICM was low at a redshift of ~ 2, the galactic outflows would have been more effective than ram-pressure stripping.

9.2.3 WHIM

Since the emission from the WHIM is very faint and spatially diffuse, the Suzaku XIS is the most suitable device to search for the O VII line emitted from the WHIM. Therefore, we selected the Suzaku observations of A1413 and the Sculptor clusters A2801, A2804, and A2811. These clusters have relatively high redshifts, which is important to distinguish the redshifted O VII line from the unredshifted one emitted from the LHB and MWH. Analyzing these observations, we reached the following conclusions:

- We detected the redshifted O VII line in the outermost region of A1413 with a statistical confidence level of 99.86%. The center energy and the surface brightness of this line are 505^{+17}_{-15} eV and $1.04^{+0.51}_{-0.45} \times 10^{-7}$ photons cm^{-2} s^{-1} arcmin^{-2}. However, we cannot rule out the possibility that the SCX emission might have resulted in the detection of the redshifted O VII line, although the detection is unlikely due to the O VII line emitted from the LHB and MWH and the O I line emitted from the Earth's atmosphere.

- The redshifted O VII line, emitted from the outskirt region of the Sculptor clusters, cannot be detected with an upper limit of 5.2×10^{-8} photons cm^{-2} s^{-1} arcmin^{-2}.

9.3 Future prospects

We selected the eight regular clusters and obtained their temperature and metallicity profiles, but previous works (Markevitch et al. 1998; De Grandi & Molendi 2002; De Grandi et al. 2004; Vikhlinin et al. 2005; Pratt et al. 2007) obtained these profiles of 10–30 regular clusters. Hereafter, it is important to observe more clusters using Suzaku. In such observations, we suggest to observe the outermost region ($r \gtrsim 0.5 r_{180}$) of a cluster with a long exposure time ($\gtrsim$60 ks) as discussed in subsection 5.2.8 because the flux of ICM in the outermost region is generally consist with or lower than that of the CXB. By increasing the number of cluster samples, the differences of the temperature and metallicity between cooling-core and non cooling-core clusters might be revealed in the outer region, as discussed by De Grandi & Molendi (2002) and De Grandi et al. (2004). In the search for the WHIM, previous works (Takei et al. 2007a; Fujita et al. 2008) were limited to the inner regions of clusters ($r \lesssim 0.6 r_{180}$). However, our results imply that the surface brightness of the O VII line emitted from the WHIM is comparable with or lower than that emitted from the LHB and MWH. Therefore, we suggest that the outer region ($r \gtrsim 0.6 r_{180}$), where the surface brightness of the ICM is sufficiently low, be observed to detect the WHIM emission.

Our results indicate that the ICM temperature strongly depends on the CXB fluctuation. Since the Suzaku XRT has a limited angular resolution, the point source sensitivity of the Suzaku XIS is not as high as those of the Chandra ASIC and the XMM-Newton EPIC. In other words, the threshold for point source elimination, S_0 in eqs. (5.11) and (5.12), of the Suzaku XIS is by a factor of about 10 and 100 higher than those of the XMM-Newton EPIC (Hasinger et al. 2001) and the Chandra ACIS (Campana et al. 2001), respectively. This results in the large CXB fluctuation as expressed in eq. (5.12), which becomes difficult to accurately measure the ICM temperature in the outermost regions of clusters. However, this problem might be improved by the next Japanese X-ray satellite, which is called "NeXT". It is proposed that NeXT is equipped with the X-ray telescope whose angular resolution is higher than that of the Suzaku XRT and comparable to that of the XMM-Newton XRT. Moreover, its effective area is comparable to that of the Suzaku XRT. The high angular resolution and large effective area are effective in the cluster outer regions as well as in the inner regions. If S_0 for NeXT is 10 times lower than that for Suzaku, the CXB fluctuation for NeXT is expected to be about 2 times smaller than that for Suzaku by eq. (5.12). In addition, since the orbit of NeXT will be approximately the same altitude as that of Suzaku, the NXB level and the NXB reproducibility of NeXT are expected to be comparable to those of Suzaku. The characteristics of clusters will be more accurately investigated from inner to outer regions using NeXT.

Appendix A

New and old map for the cut-off-rigidity

The cut-off-rigidity values have been calculated from the orbital position of Suzaku using a cut-off-rigidity map shown in Fig. A.1(a). However, the map assumes charged particles originating from the zenith direction at an altitude of 500 km, and it uses an international geomagnetic reference field for 1975. This cut-off-rigidity definition (hereafter "COR") is out of date and inaccurate. We therefore define a new cut-off-rigidity map based on the recent cut-off-rigidity database.

The new cut-off-rigidity map is calculated by using corrected geomagnetic (CGM) coordinates. The CGM coordinates are useful to study geophysical phenomena affected by the Earth's magnetic field and are provided at the web service by NASA[1] (Tsyganenko 1996). To calculate the CGM coordinates, several parameters are required. We set these parameters as follows; altitude is 570km, date is 2006/01/01 00:00:00, and default parameters are employed for the solar wind (Den = 3, Vel = 400, BY = 5, BZ = -6, and Dst = -30). Then, the new cut-off-rigidity value, R_C, is calculated as follows,

$$R_C = 14.5 \frac{\cos^2 \theta}{r^2} \quad \mathrm{GV}, \tag{A.1}$$

where θ is the latitude in CGM coordinates. r is the distance from the center of earth's magnetism, and the value of r is normalized by the radius of the earth. We call this cut-off-rigidity as "*COR2*". Figure A.1(b) shows the *COR2* map. In the red box region shown in Fig. A.1(b), since the CGM cannot be obtained due to the local magnetic structure, we use geomagnetic latitude obtained with dipole approximation in place of the CGM.

The cut-off-rigidity value for each event can be determined from the EHK file associated with each observation. The EHK files before revision 2.0 processing contain only the

[1]The service is available at ⟨ http://modelweb.gsfc.nasa.gov/models/cgm/t96.html ⟩

COR, while those after revision 2.0 contain both the *COR* and the *COR2*. These *COR* and *COR2* values are calculated using the cut-off-rigidity maps of *rigidity_20000101.fits* and *rigidity_20060421.fits* in the generic area of the calibration database (CALDB).

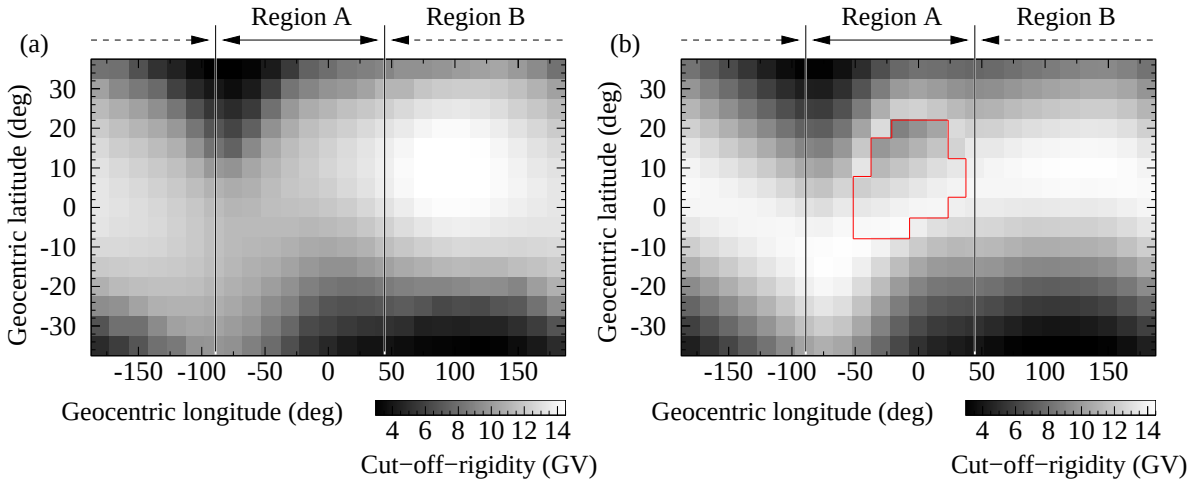

Figure A.1: Maps of (a) the *COR* and (b) the *COR2*. The region A is $-90° <$ latitude $< 45°$, and the region B encompasses the remaining latitude range.

We evaluate the reproducibility of the NXB model with the *COR* by the same way as that with the *COR2* or the PIN-UD in main text. The bin ranges of the *COR* to sort the NXB data and on-source data are the same as the *COR2* as shown in table 4.3. Table A.1 shows the reproducibility of the NXB model with the *COR* in the energy bands of 1–7 keV and 5–12 keV. The reproducibility is calculated by dividing the *NXB2* data into 5 ks or 50 ks exposure bins. We found that the *COR* has the worst reproducibility among the three kinds of the NXB models.

We searched for the location where the *COR* does not perfectly reproduce the XIS NXB. Figure A.2(1) shows the average count rate of the XIS0 NXB in the 5–12 keV energy band as a function of the three modeling parameters, in the northern hemisphere and in the southern hemisphere, displayed separately. This count rate is obtained from the *NXB2* data. For the three modeling parameters, there is not a large difference between the NXB count rate in the northern hemisphere and that in the southern hemisphere. On the other hand, if we take the data from two different longitude regions, region A and region B in Fig. A.1, we obtain Fig. A.2(2). There is a significant difference between the NXB count rate in region A and that in region B for a given value of the *COR*. This is one reason the *COR* gives the worst reproducibility.

Table A.1: Reproducibility of the NXB model with the *COR* in the energy bands of 1–7 keV and 5–12 keV.

Sensor	Reproducibility of *COR* (%)			
	5 ks exposure		50 ks exposure	
	1–7 keV*	5–12 keV†	1–7 keV*	5–12 keV†
XIS0	5.73 ± 0.76	4.46 ± 0.64	2.28 ± 0.88	1.60 ± 0.72
XIS1	7.97 ± 0.73	6.60 ± 0.51	3.42 ± 0.94	3.12 ± 0.75
XIS2	7.63 ± 0.85	5.60 ± 0.68	1.70 ± 0.84	2.02 ± 0.77
XIS3	6.58 ± 0.85	3.20 ± 0.65	2.14 ± 0.92	1.15 ± 0.72

* These values are normalized by the average count rates shown in table 4.6.

† These values are normalized by the average count rates shown in table 4.4.

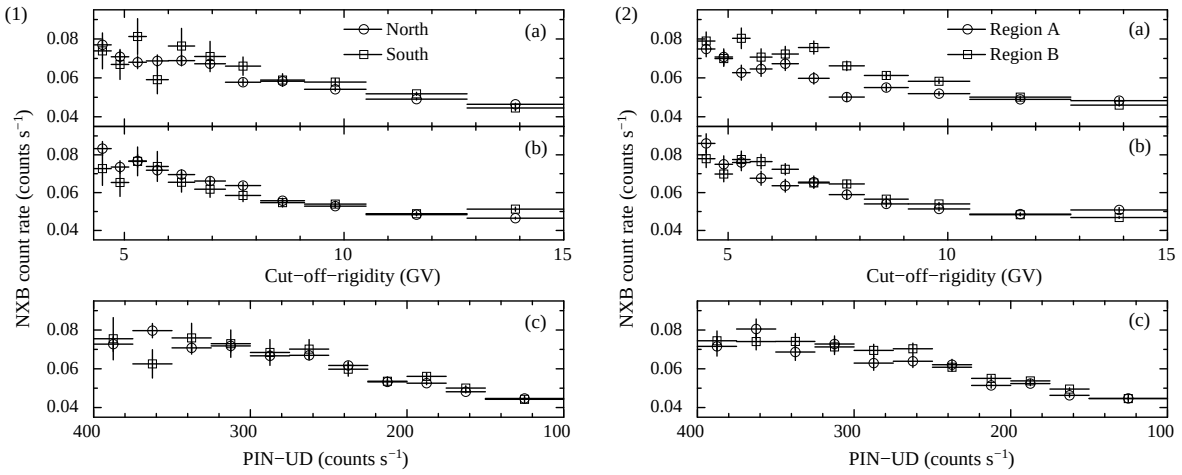

Figure A.2: NXB of the XIS0 for given values of (a) *COR*, (b) *COR2*, and (c) PIN-UD. (1) shows the NXB count rates for the northern and southern hemisphere separately. Open circles are for the north hemisphere and open squares for the south hemisphere. (2) shows the count rates for region A and region B (see Fig. A.1). Open circles are for region A and open squares for region B.

Appendix B

Errors of the statistical parameters

We discuss the errors of σ_c, $\sigma_{sta,c}$, $\sigma_{sys,c}$, and $\sigma_{sys,\Delta c}$ as defined in subsection 4.2.2. If the distribution of C_j follows a Gaussian distribution whose average and standard deviation are μ and σ respectively, then $(n-1)\sigma_c^2/\sigma^2 \equiv X$ follows a χ^2 distribution with $(n-1)$ degrees of freedom. The expected value and variance of X are $(n-1)$ and $2(n-1)$, respectively. Although the distribution of the statistical error of X does not correctly follow a Gaussian distribution, the statistical error can be approximated with $\sqrt{2(n-1)}$. Thus, the statistical error of σ_c^2 is $\sigma^2\sqrt{2/(n-1)}$. However, since σ is a standard deviation of the parent population and can not be obtained, we approximate that σ equals σ_c. As a result, the statistical error of σ_c^2 is $\sigma_c^2\sqrt{2/(n-1)}$. The statistical error of σ_c ($\Delta\sigma_c$) is expressed by using the principle of error propagation as follows,

$$\Delta\sigma_c = \frac{\sigma_c}{\sqrt{2(n-1)}} \ . \tag{B.1}$$

In the same way, the statistical error of $\sigma_{sta,c}$ ($\Delta\sigma_{sta,c}$) is obtained as follows,

$$\Delta\sigma_{sta,c} = \frac{\sigma_{sta,c}}{\sqrt{2(n-1)}} \ . \tag{B.2}$$

The statistical errors of $\sigma_{sys,c}$ ($\Delta\sigma_{sys,c}$) is expressed by using the principle of error propagation as follows,

$$\Delta\sigma_{sys,c} = \frac{1}{\sigma_{sys,c}\sqrt{2(n-1)}}\sqrt{\sigma_c^4 + \sigma_{sta,c}^4} \ . \tag{B.3}$$

In the same way as $\Delta\sigma_{sys,c}$, the statistical error of $\sigma_{sys,\Delta c}$ ($\Delta\sigma_{sys,\Delta c}$) is expressed as follows

$$\Delta\sigma_{sys,\Delta c} = \frac{1}{\sigma_{sys,\Delta c}\sqrt{2(n-1)}}\sqrt{\sigma_{\Delta c}^4 + \sigma_{sta,\Delta c}^4} \ . \tag{B.4}$$

Appendix C

Individual spectra of clusters

In this appendix, we show the spectrum and the best-fit model for each annular region and each sample cluster, i.e. A1060, A1413, A1795, A2052, A2218, A2801, A2801, A2804, and A2811.

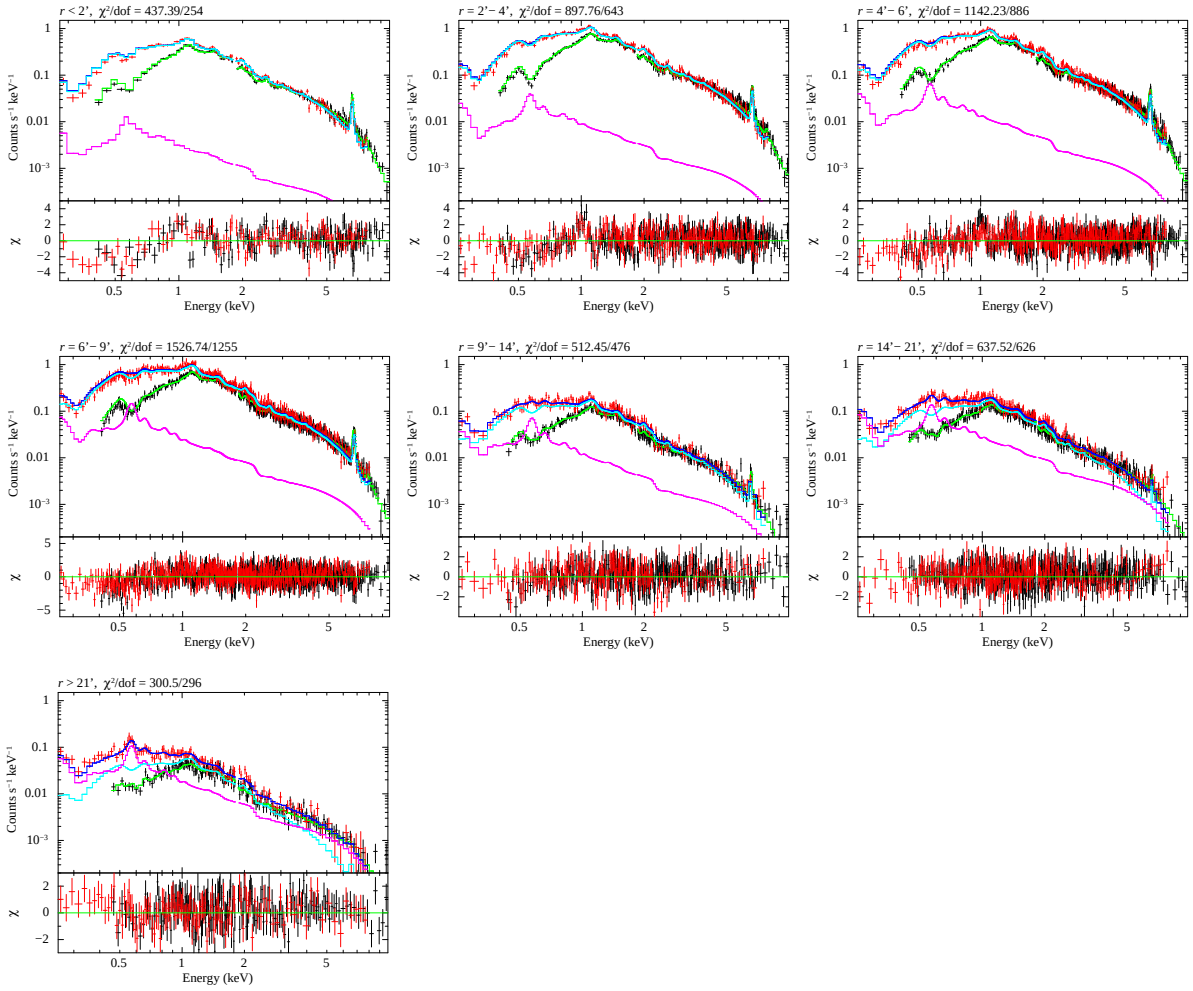

Figure C.1: A1060 spectra. The black and red lines show the FI and BI spectra from which the NXB model spectra have been subtracted, respectively. These spectra were fitted with a model in which the ICM, WABS × APEC, and the sky X-ray background, APEC + WABS (APEC + POWERLAW), were summed in XSPEC. The best-fit models are plotted by green and blue lines for the FI and BI spectra, respectively. The ICM and the sky X-ray background components for the BI spectra are plotted by the cyan and magenta lines, respectively.

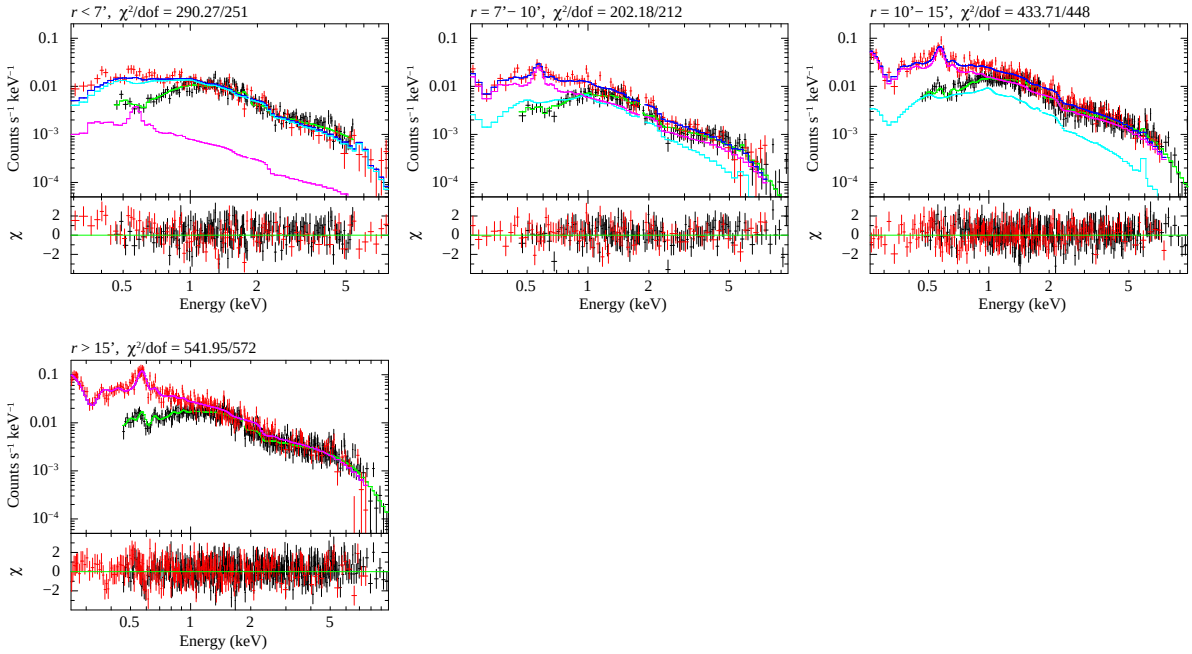

Figure C.2: A1413 spectra. The energy band greater than 5.5 keV of the FI spectrum for the innermost region ($r < 7'$, top left) was not used in the fit because this spectrum was extracted from the region including the calibration source regions. The bottom left panel shows the spectra for the blank sky field in the A1413 observation.

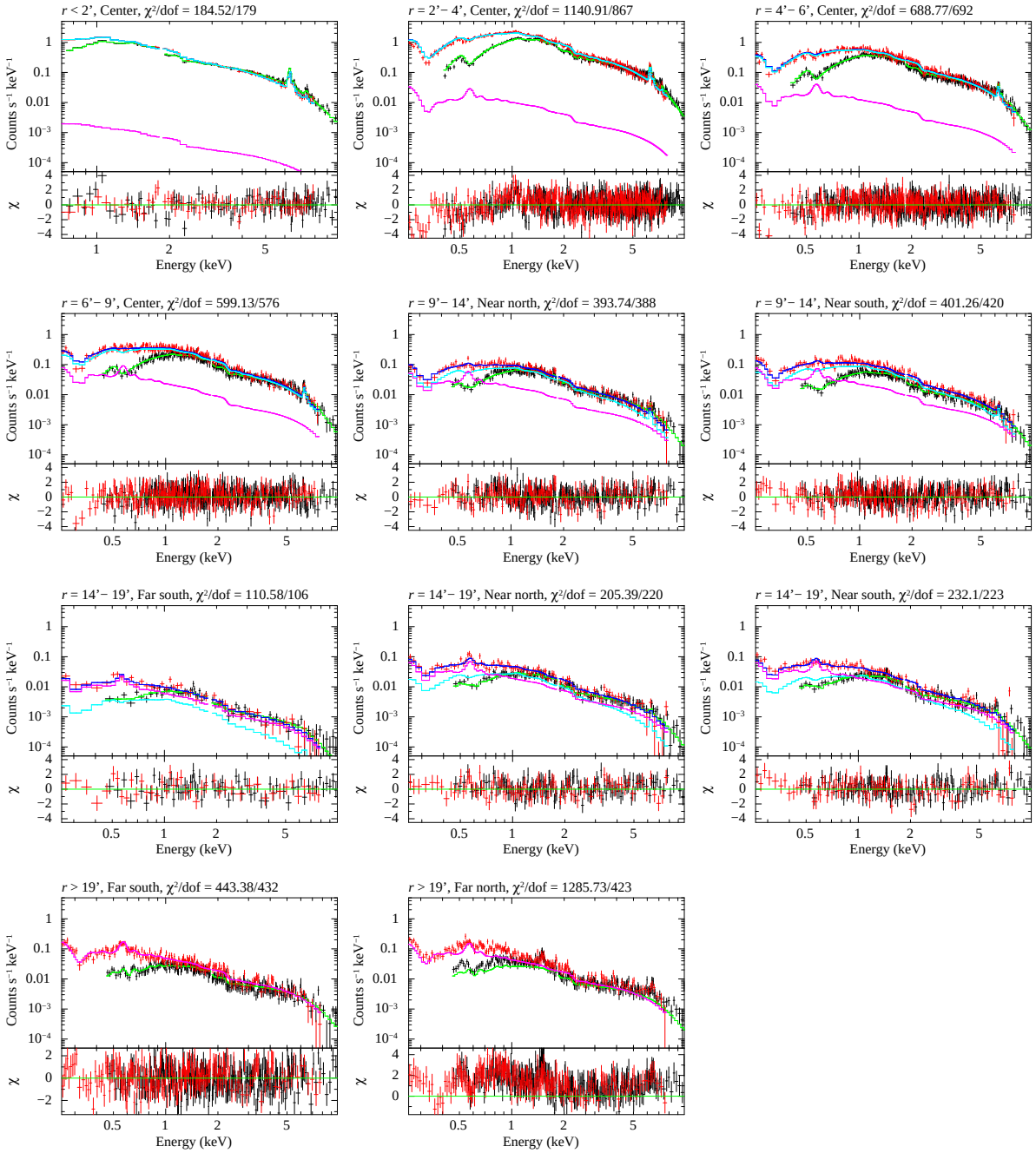

Figure C.3: A1795 spectra. The bottom left and center panels show the spectra for the blank sky field in the A1795 observations, but the spectrum of bottom center panel, which was extracted from the far north observation, is not used in this analysis due to its high background level.

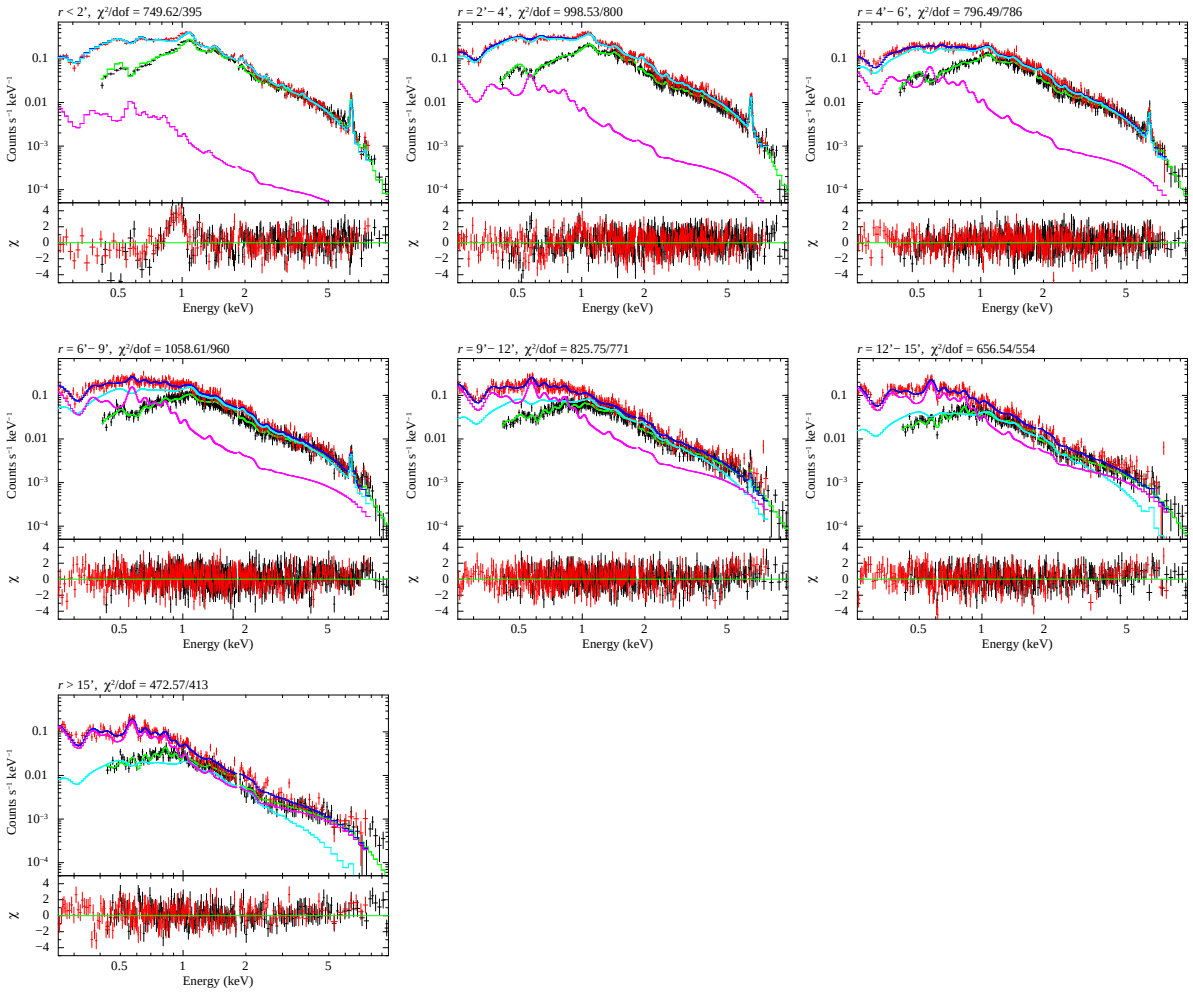

Figure C.4: A2052 spectra.

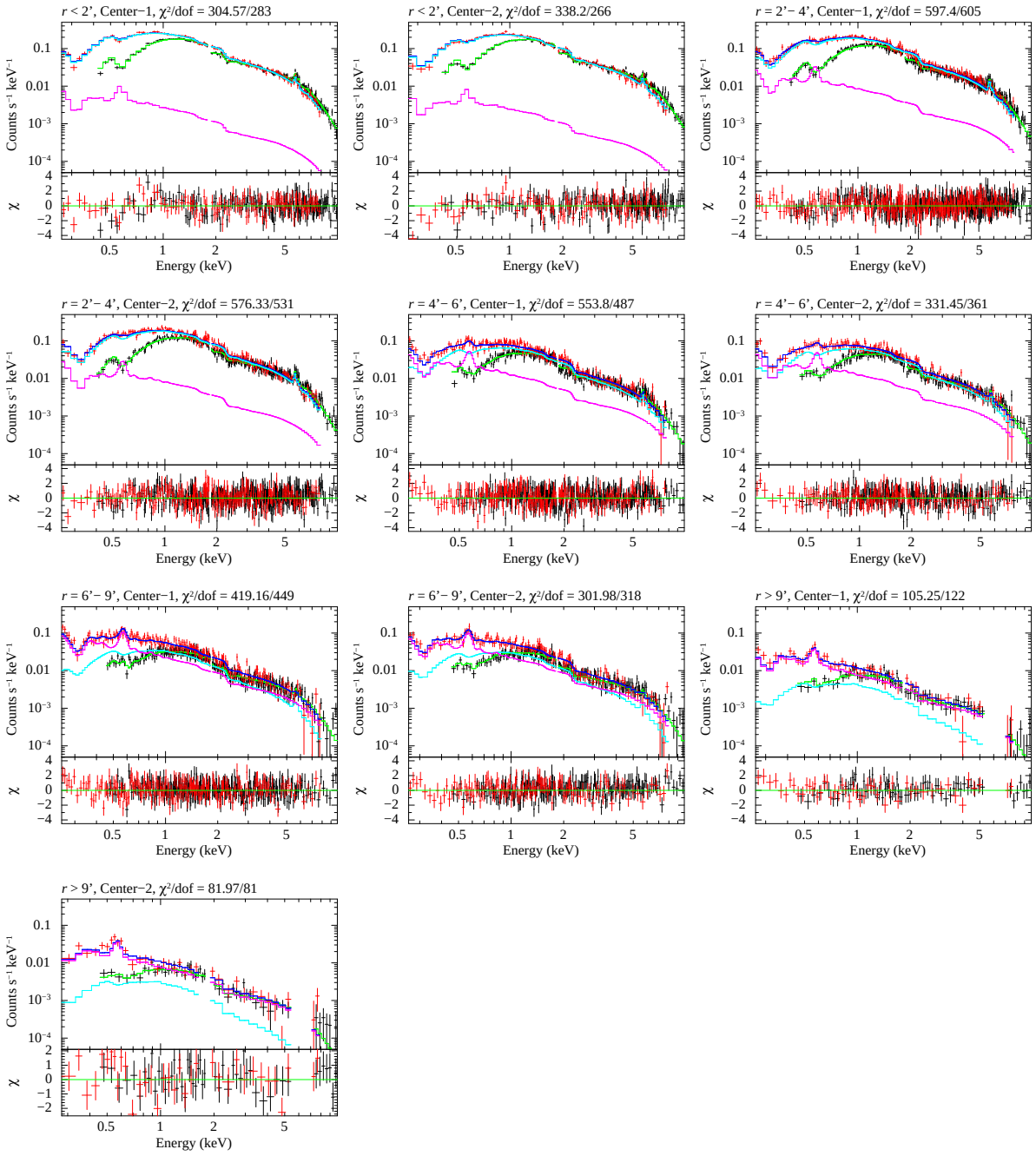

Figure C.5: A2218 spectra. The energy band of 5.5–7.0 keV of the spectra for the outermost region ($r > 9'$) was not used in the fit because these spectra were extracted from the region including the calibration source regions.

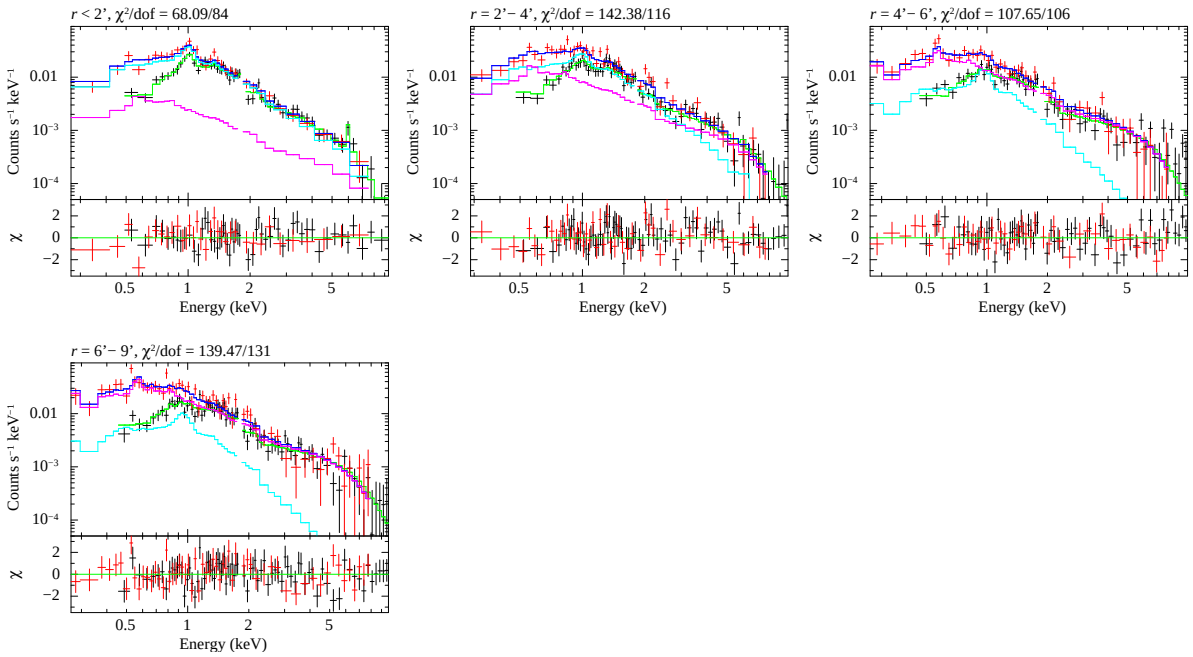

Figure C.6: A2801 spectra.

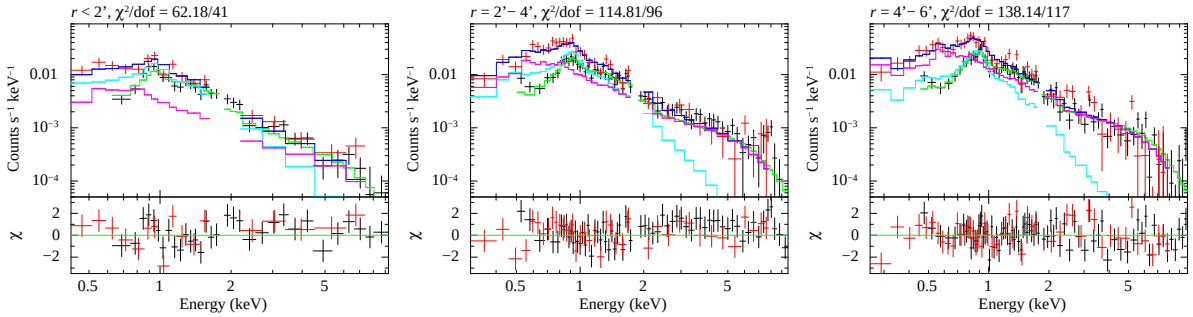

Figure C.7: A2804 spectra.

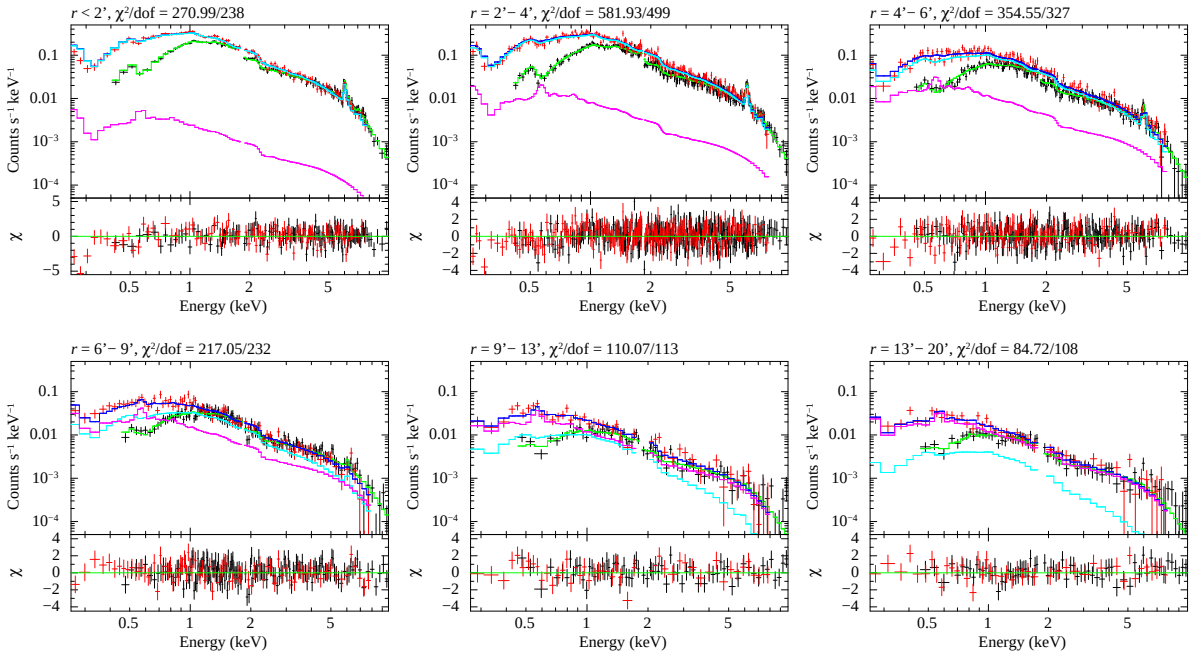

Figure C.8: A2811 spectra.

Acknowledgments

First of all, I sincerely thank to Prof. K. Hayashida for his help and useful comments. He supported my studies from all sides, such as statistical considerations, calibrations of the XIS, and analysis of clusters. I also thank to Prof. H. Tsunemi. His advice from a broad perspective was very useful for me. I am grateful to Prof. Y. Fujita. By collaborating with him, we was able to get not only an observational concept, but also a theoretical prospect.

Finally, I wish to thank all of members in X-ray Astronomy Group in Osaka University and the XIS team.

References

Abell, G. O. 1958, ApJS, 3, 211

Abell, G. O., Corwin, H. G. Jr., & Olowin, R. P. 1989, ApJS, 70, 1

Allen, S. W., Schmidt, R. W., & Fabian, A. C. 2001, MNRAS, 328, 37

Anders, E., & Grevesse, N. 1989, Geochim. Cosmochim. Acta, 53, 197

Arnaud, M., Rothenflug, R., Boulade, O., Vigroux, L., & Vangioni-Flam, E. 1992, A&A, 254, 49

Arnaud, M., Neumann, D. M., Aghanim, N., Gastaud, R., Majerowicz, S., & Hughes, J. P. 2001, A&A, 365, 80

Arnaud, M., Pointecouteau, E., & Pratt, G. W. 2005, A&A, 441, 893

Ascasibar, Y., Yepes, G., Müller, V., & Gottlöber, S. 2003, MNRAS, 346, 731

Baldi, A., Ettori, S., Mazzotta, P., Tozzi, P., & Borgani, S. 2007, ApJ, 666, 835

Bautz, M. W., et al. 1998, Proc. SPIE, 3444, 210

Benson, A. J., Bower, R. G., Frenk, C. S., Lacey, C. G., Baugh, C. M., & Cole, S. 2003, ApJ, 599, 38

Blanton, E. L., Sarazin, C. L., & McNamara, B. R. 2003, ApJ, 585, 227

Bonamente, M., Lieu, R., & Kaastra, J. 2005, A&A, 443, 29

Borgani, S., Murante, G., Springel, V., Diaferio, A., Dolag, K., Moscardini, L., Tormen, G., Tornatore, L., & Tozzi, P. 2004, MNRAS, 348, 1078B

Bregman, J. N., & Lloyd-Davies, E. J. 2006, ApJ, 644, 167

Briel, U. G., & Henry, J. P. 1993, A&A, 278, 379

Burke, B. E., Mountain, R. W., Harrison, D. C., Bautz, M. W., Doty, J. P., Ricker, G. R., & Daniels, P. J. 1991, IEEE Trans. ED, 38, 1069

Byram, E. T., Chubb, T. A., & Friedman, H. 1966, Science, 152, 66

Campana, S., Moretti, A., Lazzati, D., & Tagliaferri, G. 2001, ApJ, 560, 19

Carter, J. A. & Read, A. M. 2007, ApJ, 464, 1155

Cen, R., & Ostriker, J. P. 1999, ApJ, 514, 1

Cen, R., & Ostriker, J. P. 2006, ApJ, 650, 560

Colberg, Jörg M., Krughoff, K. S., & Connolly, A. J. 2005, MNRAS, 359, 272

Condon, J. J. 1974, ApJ, 188, 279

Danforth, C. W., & Shull, J. M. 2005, ApJ, 624, 555

Davé, R., Cen, R., Ostriker, J. P., Bryan, G. L., Hernquist, L., Katz, N., Weinberg, D. H., Norman, M. L., & O'Shea, B. 2001, ApJ, 552, 473

De Grandi, S., & Molendi, S. 2001, ApJ, 551, 153

De Grandi, S., & Molendi, S. 2002, ApJ, 567, 163

De Grandi, S., Ettori, S., Longhetti, M., & Molendi, S. 2004, A&A, 419, 7

De Young, D. S. 1978, ApJ, 223, 47

Dolag, K., Meneghetti, M., Moscardini, L., Rasia, E., & Bonaldi, A. 2006, MNRAS, 370, 656

Domainko, W., Mair, M., Kapferer, W., van Kampen, E., Kronberger, T., Schindler, S., Kimeswenger, S., Ruffert, M., & Mangete, O. E. 2006, A&A, 452, 795

Einasto, M., Einasto, J., Tago, E., Müller, V., & Andernach, H. 2001, AJ, 122, 2222

Ettori, S., Borgani, S., Moscardini, L., Murante, G., Tozzi, P., Diaferio, A., Dolag, K., Springel, V., Tormen, G., & Tornatore, L. 2004, MNRAS, 354, 111

Evrard, A. E., Metzler, C. A., & Navarro, J. F. 1996, ApJ, 469, 494

Feldmeier, J. J., Mihos, J. C., Morrison, H. L., Rodney, S. A., & Harding, P. 2002, ApJ, 575, 779

Franceschini, A., Aussel, H., Cesarsky, C. J., Elbaz, D., & Fadda, D. 2001, A&A, 378, 1

Finoguenov, A., Arnaud, M., & David, L. P. 2001, ApJ, 555, 191

Finoguenov, A., Reiprich, T. H., & Böhringer, H.

Finoguenov, A., Briel, U. G., & Henry, J. P. 2003, A&A, 410, 777

Fritz, G., Davidsen, A., Meekins, J. F., Friedman, H. 1971, ApJ, 164, 81

Fukazawa, Y., Makishima, K., Tamura, T., Nakazawa, K., Ezawa, H., Ikebe, Y., Kikuchi, K., & Ohashi, T. 2000, MNRAS, 313, 21

Fukugita, M., Hogan, C. J., & Peebles, P. J. E. 1998, ApJ, 503, 518

Fukugita, M., Peebles, P. J. E. 2004, ApJ, 616, 643

Fujimoto, R., et al. 2004, PASJ, 56, 29

Fujimoto, R., et al. 2007, PASJ, 59, 133

Fujita, Y., Koyama, K., Tsuru, T., & Matsumoto, H. 1996, PASJ, 48, 191

Fujita, Y., & Nagashima, M. 1999, ApJ, 516, 619

Fujita, Y., Tawa, N., Hayashida, K., Takizawa, M., Matsumoto, H., Okabe, N., & Reiprich, T. H. 2008, PASJ, in press (astro-ph/07052017)

Fusco-Femiano, R., Dal Fiume, D., Feretti, L., Giovannini, G., Grandi, P., Matt, G., Molendi, S., & Santangelo, A. 1999, ApJ, 513, 21

Fusco-Femiano, R., Dal Fiume, D., De Grandi, S., Feretti, L., Giovannini, G., Grandi, P., Malizia, A., Matt, G., & Molendi, S. 2000, ApJ, 534, 7

Garmire, G. P., et al. 1992, in AIAA, Space Programs and Technologies Conference (Paper 92-1473) (New York: AIAA)

Giacconi, R., et al. 2001, ApJ, 551, 624

Goto, T., Yamauchi, C., Fujita, Y., Okamura, S., Sekiguchi, M., Smail, I., Bernardi, M., & Gomez, P. L. 2003, MNRAS, 346, 601

Gunn, J. E., Gott, J. R. I. 1972, ApJ, 176, 1

Hashimotodani, K., Hayashida, K., Takai, T., Kawasaki, W., & Takeuchi, T. T. 2000, Advances in Space Research, 25, 611

Hasinger, G., et al. 2001, A&A, 365, 45

Hayakawa, A, Hoshino, A, Ishida, M, Furusho, T, Yamasaki, N. Y., & Ohashi, T. 2006, PASJ, 58, 695

Horner, D. J., Baumgartner, W. H., Gendreau, K. C., Mushotzky, R. F., Loewenstein, M., & Molnar, S. M. 2000, AAS, 32, 1581

Ikebe, Y., Böhringer, H., & Kitayama, T. 2004, ApJ, 611, 175

Irwin, J. A., Bregman, J. N., & Evrard, A. E. 1999, ApJ, 519, 518

Irwin, J. A., & Bregman, J. N. 2000, ApJ, 538, 543

Ishisaki, Y. et al. 2007, PASJ, 59S, 113

Kaastra, J. S. & Mewe, R. 1993, A&AS, 97, 443

Kaastra, J. S., Lieu, R., Tamura, T., Paerels, F. B. S., den Herder, J. W. 2003, A&A, 397, 445

Kaastra, J. S. 2004, J. Korean Astron. Soc., 37, 375

Kaastra, J. S., Tamura, T., Peterson, J. R., Bleeker, J. A. M., Ferrigno, C., Kahn, S. M., Paerels, F. B. S., Piffaretti, R., Branduardi-Raymont, G., Böhringer, H. 2004, A&A, 413, 415

Kaastra, J. S., Werner, N., Herder, J. W. A. den, Paerels, F. B. S., de Plaa, J., Rasmussen, A. P., & de Vries, C. P. 2006, ApJ, 652, 189

Kalberla, P. M. W., Burton, W. B., Hartmann, Dap, Arnal, E. M., Bajaja, E., Morras, R., & Pöppel, W. G. L. 2005, A&A, 440, 775

Kapferer, W., et al. 2006, A&A, 447, 827

Kapferer, W., Kronberger, T., Weratschnig, J., Schindler, S., Domainko, W., van Kampen, E., Kimeswenger, S., Mair, M., & Ruffert, M. 2007, A&A, 466, 813

Katayama H., 2003, PhD thesis, Osaka University

Katayama, H., Takahashi, I., Ikebe, Y., Matsushita, K., & Freyberg, M. J. 2004, A&A, 414, 767

Katayama, H., Hayashida, K., & Nishino Y. 2005, Advances in Space Research, 36, 689

Katz, N., & White, S. D. M. 1993, ApJ, 412, 455

Kay, S. T., Thomas, Peter A., Jenkins, Adrian, & Pearce, Frazer R. 2004, MNRAS, 355, 1091

Kelley, R. L., et al. 2007, PASJ, 59, 77

King, I. 1962, AJ, 67, 471

Kokubun, M., et al. 2007, PASJ, 59, S53

Komatsu, E., & Seljak, U. 2001, MNRAS, 327, 1353

Koyama, K., et al. 2007a, PASJ, 59, 23

Koyama, K., et al. 2007b, PASJ, 59, 245

Kuntz, K. D., Snowden, S. L. 2000, ApJ, 543,195

Kushino, A., Ishisaki, Y., Morita, U., Yamasaki, N. Y., Ishida, M., Ohashi, T., & Ueda, Y. 2002, PASJ, 54, 327

Loken, C., Norman, M. L., Nelson, E., Burns, J., Bryan, G. L., & Motl, Patrick 2002, ApJ, 579, 571

Lumb, D. H., Warwick, R. S., Page, M., & De Luca, A. 2002, A&A, 389, 93

Machacek, M. E., Bautz, M. W., Canizares, C., & Garmire, G. P. 2002, ApJ, 567, 188

Makishima, K. et al. 2001, PASJ, 53, 401

Markevitch, M., Forman, W. R., Sarazin, C. L., & Vikhlinin, A. 1998 ApJ, 503, 77

Markevitch, M., Vikhlinin, A., Forman, W. R., & Sarazin, C. L. 1999, ApJ, 527, 545

McCammon, D., et al. 2002, ApJ, 576, 188

Mitchell, R. J., Culhane, J. L., Davison, P. J. N., & Ives, J. C. 1976, MNRAS, 175, 29

Mitsuda, K., et al. 2007, PASJ, 59, 1

Mizuno, T., Kamae, T., Godfrev, G., Handa, T., Thompson, D. J., Lauben, D., Fukazawa, Y., & Ozaki, M. 2004, ApJ, 614, 1113

Moll, R., Schindler, S., Domainko, W., Kapferer, W., Mair, M., van Kampen, E., Kronberger, T., Kimeswenger, S., & Ruffert, M. 2007, A&A, 463, 513

Nagashima, M., Lacey, C. G., Baugh, C. M., Frenk, C. S., & Cole, Shaun 2005, MNRAS, 358, 1247

Nevalainen, J., Oosterbroek, T., Bonamente, M., & Colafrancesco, S. 2004, ApJ, 608, 166

Nevalainen, J., Markevitch, M., & Lumb, D. 2005, ApJ, 629, 172

Navarro, J. F., Frenk, C. S., & White, S. D. M. 1995, MNRAS, 275, 56

Navarro, J. F., Frenk, C. S., & White, S. D. M. 1996, ApJ, 462, 563

Neumann, D. M., & Arnaud, M. 1999, A&A, 348, 711

Nicastro, F., et al. 2005, ApJ, 629, 700

Oegerle, W. R., & Hill, J. M. 2001, AJ, 122, 2858

Peterson, J. R., Kahn, S. M., Paerels, F. B. S., Kaastra, J. S., Tamura, T., Bleeker, J. A. M., Ferrigno, C., & Jernigan, J. G. 2003, ApJ, 590, 207

Poole, G. B., Fardal, M. A., Babul, A., McCarthy, I. G., Quinn, T., & Wadsley, J. 2006, MNRAS, 373, 881

Pratt, G. W. & Arnaud, M. 2002, A&A, 394, 375

Pratt, G. W., Böhringer, H.; Finoguenov, A. 2005, A&A, 433, 777

Pratt, G. W., Böhringer, H., Croston, J. H., Arnaud, M., Borgani, S., Finoguenov, A., & Temple, R. F. 2007, A&A, 461, 71

Quilis, V., Moore, B., & Bower, R. 2000, Science, 288, 1617

Rasmussen, A. P., Kahn, S. M., Paerels, F., Herder, J. W. den, Kaastra, J., & De Vries, C. 2007, ApJ, 656, 129

Raymond, J. C. & Smith, B. W. 1977, ApJS, 35, 419

Ricker, P. M., & Sarazin, C. L. 2001, ApJ, 561, 621

Romeo, A. D., Sommer-Larsen, J., Portinari, L., & Antonuccio-Delogu, V. 2006, MNRAS, 371, 548

Rybicki, G. B. & Lightman, A. P. 1979, New York, Wiley-Interscience

Sakelliou, I., Ponman, T. J. 2004, MNRAS, 351, 1439

Sarazin, C. L. 1988, "X-ray emissions from clusters of galaxies", Cambridge University Press

Sato K., et al. 2007, PASJ, 59, 299

Serlemitsos, P. J., et al. 2007, PASJ, 59, 9

Smith, R. K., Brickhouse, N. S., Liedahl, D. A., & Raymond, J. C. 2001, ApJ, 556, L91

Snowden, S. L., et al. 1997, ApJ, 485, 125

Snowden, S. L., Egger, R., Finkbeiner, D. P., Freyberg, M. J., & Plucinsky, P. P. 1998 ApJ, 493, 715

Spergel, D. N., et al. 2003, ApJS, 148, 175

Springel, V. & Hernquist, L 2002, MNRAS, 333, 649

Springel, V. 2005 MNRAS, 364, 1105

Strüder, L., et al. 2001, A&A, 365, 18

Takahashi, T., et al. 2007, PASJ, 59, S33

Takei, Y., et al. 2007a, PASJ, 59, 339

Takei, Y., Henry, J. P., Finoguenov, A., Mitsuda, K., Tamura, T., Fujimoto, R., & Briel, U. G. 2007b, ApJ, 655, 831

Takizawa, M. 1999, ApJ, 520, 514

Tamura, T., et al. 2001, A&A, 365, 87

Tamura, T., Kaastra, J. S., den Herder, J. W. A., Bleeker, J. A. M., & Peterson, J. R. 2004, A&A, 420, 135

Tawa, N., et al. 2008, PASJ, in press

Tornatore, L., Borgani, S., Matteucci, F., Recchi, S., & Tozzi, P. 2004, MNRAS, 349, 19

Tsyganenko, N. A. 1995, J. Geophys. Res., 100, 5599

Tsyganenko, N. A. 1996, Proc. Third Int. Conf. on Substorms (ICS-3), Versailles, France, 12-17 May 1996, ESA SP-389

Turner, M. J. L., et al. 2001, A&A, 365, 27

Ueda, Y., Akiyama, M., Ohta, K., & Miyaji, T. 2003, ApJ, 598, 886

Vikhlinin, A., Markevitch, M., Murray, S. S., Jones, C., Forman, W., & Van Speybroeck, L. 2005, ApJ, 628, 655

Weisskopf, M. C., Brinkman, B., Canizares, C., Garmire, G., Murray, S., & Van Speybroeck, L. P. 2002, PASP, 114, 1

White, D. A. 2000, MNRAS, 312, 663

Yamaguchi, H., et al. 2006, Proc. SPIE, 6266, 626642

Yamasaki, N. Y., Ohashi, T., & Furusho, T. 2002, ApJ, 578, 833

Yamashita, A., et al. 1997, IEEE Trans., Nucl., Sci., 44, 847

Zwicky, F. E., Herzog, P., Wild, M. K., & Kowal, C. T., 1961-1968, *Catalogues of Galaxies and Clusters of Galaxies*, Vol. 1-6, Pasadena, Caltech.

Abbreviations

ACE	Advanced Composition Explorer
ACTX	X axis of actual coordinate for the XIS CCD chip
ACTY	Y axis of actual coordinate for the XIS CCD chip
ARF	Ancillary response file
BI CCD	Back-illuminated CCD
CALDB	Calibration database
CCD	Charge-coupled device
CDM	Cold dark matter
CGM	Corrected geomagnetic
CL	Confidence level
COR	Conventional cut-off-rigidity
COR2	New type of cut-off-rigidity
CTE	Charge transfer efficiency
CXB	Cosmic X-ray background
DETX	X axis of detector coordinate for the XIS
DETY	Y axis of detector coordinate for the XIS
DYE_ELV	Earth day-time elevation angles
EHK	Enhanced house keeping
ELV	Earth elevation angles
EOB	Extensible optical bench
FI CCD	Front-illuminated CCD
FOV	Field of view
FWHM	Full width at half maximum
GOES	Geostationary Operational Environmental Satellites
GSFC	Goddard Space Flight Center
HPD	Half power diameter
HXD	Hard X-ray Detector
ICM	Intracluster medium

ISAS	Institute of Space and Astronautical Science
JAXA	Japan Aerospace Exploration Agency
LHB	Local hot bubble
MWH	Milky Way halo
NASA	National Aeronautics and Space Administration
NED	NASA/IPAC Extragalactic Database
NEP	North ecliptic pole
NTE	Night Earth
NXB	Non-X-ray background
PIN-UD	PIN upper discriminator
RMF	Redistribution matrix file
SAA	South atlantic anomaly
SCI	Spaced-row Charge Injection
SCX	Solar-wind charge-exchange X-ray
SWEPAM	Solar Wind Electron, Proton, and Alpha Monitor
WHIM	Warm-hot intergalactic medium
XIS	X-ray Imaging Spectrometer
XIS-BI	XIS using BI CCD; i.e., XIS1
XIS-FI	XIS using FI CCD; i.e., XIS0, XIS2, and XIS3
XRS	X-ray Spectrometer
XRT	X-ray Telescope